

**FUNCTIONAL METAL-BASED
NANOSTRUCTURES AND BIOAPPLICATIONS**

TEE SI YIN

(B.Sc. (Hons.), NUS)

**A THESIS SUBMITTED
FOR THE DEGREE OF DOCTOR OF PHILISOPHY
DEPARTMENT OF BIOMEDICAL ENGINEERING
NATIONAL UNIVERSITY OF SINGAPORE**

2015

Declaration

I hereby declare that the thesis is my original work and it has been written by me in its entirety. I have duly acknowledged all the sources of information, which have been used in the thesis.

This thesis has also not been submitted for any other degree in any university previously.

Tee Si Yin

30 July 2015

Acknowledgements

This thesis represents a milestone of 5 years of work in IMRE and NUS. During these years of training have certainly broaden my horizons and shaped me into a scientific explorer.

First and foremost I would like to express my deepest gratitude to my advisor, Dr. Han Ming-Yong for his excellent guidance, patience and providing me with continuous support throughout my PhD study. I am grateful for all his contribution of time, ideas and funding to make my PhD experience productive and stimulating. I will always remember his encouragement and moral support during my difficult times, “relax, be happy”. My sincere thanks are due to my NUS supervisor, Dr. James Kah, for my dissertation reading and his helpful comments.

Dozens of people have helped at IMRE. My sincere thanks go to Dr. Ye Enyi, Dr. Khin Yin Win, Dr. Evan Williams, Dr. Michelle Dela Cruz Regulacio, Dr. Chua Chin Sheng, Dr. Wang Guan, Dr. Jiang Shan, Ms. Michelle Low, Mr. Teng Choon Peng, Ms. Koh Leng Duei, Ms. Coryl Lee, Mr. Lai szu Cheng, Mr. Jayven Yeo, Ms. Tan Hui Ru, Ms. Hui Hui Kim, Mr. Lim Poh Chong and Ms. Doreen Lai for their support, patience and encouragement.

This work would not be possible without the financial support from IMRE, ASTAR. I would like to take this opportunity to acknowledge ASTAR for providing me SSDA research scholarship to study in their premises as well as the use of their facilities for my PhD project. Last but not least, a big thank to my family, their love support has been unconditional all these years. I offer my regards and blessings to them as well as all of those who supported me in any respect during the completion of my PhD study.

Table of Contents

Declaration	i
Acknowledgements	ii
Table of Contents	iii
Summary	vii
List of Tables.....	viii
List of Figures	ix
Publications	xviii
Patents	xx
Chapter 1 Background and Significance	1
1.1 Introduction to metal-based nanostructures	2
1.11 Metals.....	2
1.12 Metal oxides.....	3
1.13 General synthetic methodology	4
1.2 Transition metal nanostructures and properties	6
1.2.1 Elemental transition metals	6
- Copper	6
- Silver.....	9
- Gold	10
- Ruthenium	12
1.2.2 Bimetallic transition metal nanostructures and properties	14
1.3 Transition metal oxide nanostructures and properties	19
- Titanium oxide.....	19
- Iron oxide.....	21
- Copper oxide	24
1.4 Rare-earth metal oxide nanostructures and properties.....	25
- Europium oxide	29
- Terbium oxide	30
1.5 Biomedical applications.....	31

	- Antibacterial activity	32
	- Targeted drug delivery	34
	- Bioimaging	37
1.6	Bioanalytical applications.....	39
	- SERS sensing.....	39
	- Electrochemical sensing	41
	- Fluorescence-based sensing.....	43
1.7	Objectives and scopes	45
Chapter 2 Fabrication of Copper Nanowires for Glucose Sensing ..47		
2.1	Introduction.....	48
2.2	Experimental section.....	51
	2.2.1 Materials.....	51
	2.2.2 Colloidal synthesis of Cu nanowires.....	51
	2.2.3 Sample preparation for characterization	52
	2.2.4 Thin film fabrication of Cu nanowires.....	52
	2.2.5 Evaluation of electrocatalytic activities of Cu nanowires.....	52
	2.2.6 Examination of antibacterial activities.....	53
2.3	Results and discussion	53
	2.3.1 Colloidal synthesis of Cu nanowires.....	53
	2.3.2 Electrocatalytic activities of Cu nanowires towards glucose oxidation	54
	2.3.3 Antibacterial activities of Cu nanowires.....	56
2.4	Summary	57
Chapter 3 Bimetallic Cu/Au(Ru) Nanostructures for Glucose Sensing58		
3.1	Introduction.....	59
3.2	Experimental section.....	60
	3.2.1 Materials.....	60
	3.2.2 Colloidal synthesis of Cu/Au (Ru) nanomaterials	60
	3.2.2.1 Bimetallic Cu/Au nanotubes (220/140 °C)	60

3.2.2.2	Other bimetallic Cu/Au nanostructures (220/220 °C and 220/300 °C).....	61
3.2.2.3	Bimetallic Cu/Ru nanowires (220/270 °C)	61
3.2.3	Sample preparation for characterization	62
3.2.4	Thin film fabrication of bimetallic Cu/Au(Ru) nanostructures.....	62
3.2.5	Evaluation of electrocatalytic activities of bimetallic Cu/Au(Ru) nanostructures	62
3.3	Results and discussion	62
3.3.1	Colloidal synthesis of bimetallic Cu/Au nanostructures.....	62
3.3.2	Electrocatalytic activities of bimetallic Cu/Au nanostructures towards glucose oxidation	68
3.3.3	Selectivity, stability and reproducibility of Cu/Au nanotubes towards glucose sensing.....	71
3.3.4	Influence of Au loading in Cu/Au nanostructures on glucose sensing	73
3.3.5	Colloidal synthesis of bimetallic Cu/Ru nanostructures	76
3.3.6	Electrocatalytic activities of bimetallic Cu/Ru nanostructures towards glucose sensing	78
3.4	Summary.....	79
Chapter 4 Rare Earth Metal Oxides for Sensing Application		80
4.1	Introduction.....	81
4.2	Experimental section.....	82
4.2.1	Materials.....	82
4.2.2	Colloidal synthesis of ZrO ₂ :Tb ³⁺ nanoparticles	83
4.2.3	Measurement of luminescent response with respect to dilution in hexane	83
4.2.4	Measurement of luminescent response to pesticides	83
4.2.5	Sample preparation for characterisation.....	84
4.3	Results and Discussion	84
4.3.1	Colloidal synthesis of ZrO ₂ :Tb ³⁺ nanoparticles	84
4.3.2	Optical properties of ZrO ₂ :Tb ³⁺ nanoparticles.....	85
4.3.3	Interparticle-distance dependent PL of ZrO ₂ :Tb ³⁺ nanoparticles....	88

4.3.4	Detection of pesticides through PL quenching of $\text{ZrO}_2:\text{Tb}^{3+}$ nanoparticles	91
4.3.5	Structure and composition study of $\text{ZrO}_2:\text{Tb}^{3+}$ nanoparticles	92
4.4	Summary	95
Chapter 5 Rare Earth Metal Oxides for Bioimaging.....		96
5.1	Introduction.....	97
5.2	Experimental section.....	98
5.2.1	Materials for nanoparticles synthesis	98
5.2.2	Colloidal synthesis of $\text{TiO}_2:\text{Eu}^{3+}$	99
5.2.3	Colloidal synthesis of TiO_2	99
5.2.4	Nanoparticles sample preparation for characterisation	100
5.2.5	Materials for PLGA encapsulation and biological experiment.....	100
5.2.6	Encapsulation of luminescent nanoparticles with PLGA	100
5.2.7	Characterisation for PLGA microparticles	101
5.2.8	Cell culture	101
5.2.9	Cell uptake of PLGA particles in confocal microscopy.....	101
5.2.10	Cell cytotoxicity assay	102
5.3	Results and discussion	102
5.3.1	Colloidal synthesis of $\text{TiO}_2:\text{Eu}^{3+}$ nanoparticles	102
5.3.2	Optical properties of $\text{TiO}_2:\text{Eu}^{3+}$ nanoparticles	103
5.3.3	Structural study of $\text{TiO}_2:\text{Eu}^{3+}$ nanoparticles	105
5.3.5	Bioimaging of PLGA encapsulated $\text{TiO}_2:\text{Eu}^{3+}$ and $\text{ZrO}_2:\text{Tb}^{3+}$ nanoparticles	109
5.4	Summary	111
Chapter 6 Conclusions and Outlook		112
6.1	Conclusions.....	113
6.2	Outlook	114
	References	115
	List of Abbreviations.....	124

Summary

Well-defined functional nanostructures are of fundamental importance in the advancement of nanoscience and nanotechnology. Colloidal synthesis techniques have been successfully developed in the fabrication of functional nanostructures. In this thesis, various metal and bimetallic nanostructures of the controlled size, shape, composition, crystal structure and surface capping are prepared for bioapplications including chemical sensing, bioimaging and bacterial inhibition. Uniform copper nanowires were first prepared through disproportionation reaction, and further used as template to form various bimetallic nanostructures such as Cu/Au (i.e., nanotubes, nanorods, and nanoparticles) for greatly improving electrochemical glucose sensing. These optimized synthesis of bimetallic Cu/Au nanotubes are incorporated as advanced glucose sensors through electrochemical sensing. The controlled fabrications of bimetallic Cu/Au nanotubes possess large surface areas and exhibited their synergistic enhancement in electrocatalytic properties in comparison with copper nanowires and other shaped Cu/Au nanostructures. Also, they have been demonstrated with high sensitivity, low detection limit and fast response towards glucose sensing. Fluorescent chemical sensing was further demonstrated using various RE-incorporated metal oxide nanoparticles ($\text{ZrO}_2:\text{Tb}^{3+}$, $\text{SiO}_2:\text{Tb}^{3+}$, $\text{TiO}_2:\text{Eu}^{3+}$, $\text{ZrO}_2:\text{Eu}^{3+}$, and $\text{SiO}_2:\text{Eu}^{3+}$) prepared in this work. The highly luminescent nanoparticles are attributed to the effective passivation of luminescent centers in amorphous metal oxide matrices to prevent concentration quenching. This is the first observation that interparticle distance of $\text{ZrO}_2:\text{Tb}^{3+}$ nanoparticles significantly alter their photoluminescent and this is optimised for highly sensitive detection of pesticides down to ppb level. The RE-incorporated metal oxide nanoparticles with high photostability and low cytotoxicity were readily encapsulated by PLGA to exhibit strong luminescent for cellular imaging and it is believed that they are potentially the next generation bioprobes in bioapplications.

List of Tables

Table 2.1 List of noble metals non-enzymatic glucose sensors. The table is presented with respect to electrode materials, sensitivity, linear range, limit of detection and publication year.....49

Table 2.2 List of transition metals non-enzymatic glucose sensors. The table is presented with respect to electrode materials, sensitivity, linear range, limit of detection and publication year.50

Table 5.1 Various concentration of Eu^{3+} in TiO_2 with ICP analysis (atomic or molar %).102

List of Figures

- Figure 1.1** The periodic table of elements. The transition metals are highlighted in yellow.....3
- Figure 1.2** Fabrication of oleylamine-coated Cu nanowires by the disproportionation reaction. (A) TEM image and (B) XRD pattern of Cu nanowires. (C) Magnified TEM image and (D) schematic illustration of Cu nanowires. (E) Schematic disproportionation reaction for the formation of Cu nanowires.²⁹ 7
- Figure 1.3** Schematic illustration of the shape-selective formation of Cu nanospheres and nanocubes via the disproportionation reaction route.³⁰8
- Figure 1.4** Three-step seed-mediated growth approach for preparing Au and Ag nanorods of controlled aspect ratio. TEM of Au nanorods.⁵⁷ 11
- Figure 1.5** (A,B) TEM and (C,D) SEM images of Ru-capped columns prepared under (A,C) 160 °C and (B,D)150 °C . The inset in (D) is the geometric model of the capped columns.⁶⁸ 14
- Figure 1.6** Schematic representation of possible mixing patterns of zero-dimensional (A-C) and one-dimensional (D-F) nanomaterial. Zero-dimensional: (A) core-shell, (B) dumbbell, (C) mixed. One-dimensional: (D) core-shell, (E) mixed, (F) bamboo-like.⁸⁷ 15
- Figure 1.7** Schematic illustrating the formation of a nanocage made of Au/Ag alloy and then a cubic nanoframe made of pure Au by selectively removing the Ag atoms from Au/Ag alloy nanobox. (A) Ag nanocubes, (B) Formation of Au/Ag alloy nanocage, (C) selective removal of the Ag atoms from the nanobox, (D) complete removal of Ag from the nanocage. Corresponding TEM and SEM images (insets) of the Ag nanocube, Au nanobox, Au nanocage, and Au nanoframes, respectively.⁹⁷ 17

Figure 1.8 SEM (A, C) and TEM (B, D) of the Pt/Pd core–shell nanocubes (A, B) and Pt/Au nanorod (C, D). ⁹⁸	17
Figure 1.9 SEM (top row) and TEM images (bottom row) of Cu nanowires, Cu/Pd and Cu/Pt nanotubes. The schematic illustrating the formation mechanism of Cu/Pt alloy nanostructures and Cu/Pd bimetallic nanotubes from Cu nanowires. ¹⁰⁰	18
Figure 1.10 TEM images of TiO ₂ nanostructures. (A-C) nanorods with different aspect ratio (D) nanoparticles. Inset in parts C and D: HRTEM image of a single TiO ₂ nanorod and nanoparticle.	20
Figure 1.11 Schematic illustrating the synthesis of monodisperse nanoparticles. Metal–oleate precursors were prepared from the reaction of metal chlorides and sodium oleate. Thermal decomposition of the metal–oleate precursors in high boiling solvent produced monodisperse nanoparticles. ¹¹⁸	22
Figure 1.12 TEM images of iron oxides (A) plates, (B) truncated octahedrons, and (C) tetrahedrons. ¹²⁰	23
Figure 1.13 Formation process of hematite tube-in-tube nanostructures (top view). ¹²¹	24
Figure 1.14 The periodic table of elements. The rare earth metals are boxed in red. ...	26
Figure 1.15 Energy diagram of the trivalent RE series. ¹³⁹	28
Figure 1.16 Energy level diagram of Tb ₂ O ₃ system.....	30
Figure 1.17 Schematic illustrating magnetic nanoparticle-based drug delivery system: these magnetic carriers concentrate at the targeted site using an external high-gradient magnetic field. After accumulation of the magnetic carrier at the target tumor site <i>in vivo</i> , drugs are released from the magnetic carrier and effectively taken up by the tumor cells. ¹¹³	35

Figure 1.18 TEM images of Au nanorods with varying aspect ratios: (A) 1.5, (B) 1.9, (C) 2.3, (D) 2.4, (E) 2.7, (F) 2.8, (G) 2.9, (H) 3.1, (I) 3.5 and the corresponding UV-vis spectra of Au nanorods. ²⁰⁹	40
Figure 1.19 TEM images of Ru nanostructures (A) nanospheres, (B) irregular plates, (C) triangle plates, (D) capped columns, and (E) SERS spectra of 4-mercaptopyridine on films of Ru nanostructures: capped columns, triangle plates, nanospheres, and Raman spectra of bulk 4-mercaptopyridine solids. ⁶⁸	41
Figure 2.1 Summary of enzymatic glucose oxidation mechanism illustrating first, second and third generation sensors ²³⁰	49
Figure 2.2 Anisotropic growth of Cu nanowires by the controlled disproportionation of CuCl in oleylamine at 220 °C. (A) Schematic disproportional reaction for the formation of Cu nanowires. (B) Low magnification SEM image of Cu nanowires and the magnified TEM image at inset. (C) XRD pattern of copper nanowires.	54
Figure 2.3 CV profiles of (A) blank FTO substrate and (B) Cu nanowires on FTO substrates as electrodes at a potential window of 0-0.7 V and a scan rate of 50 mV s ⁻¹ without (---- dash line) and with (— solid line) 3.0 mM of glucose in 0.1 M sodium hydroxide solution.....	55
Figure 2.4 Electrocatalytic activities of copper nanowires on FTO substrates as electrodes up to 1800 s. (A) Chronoamperometric curves of copper nanowires at a constant potential of 0.6 V upon a successive addition of a glucose solution to obtain a cumulative concentration from 0 to 10.5 mM. Inset shows the enlarged current density region from 0-600 s. (B) The respective calibration curves of copper nanowires.....	56
Figure 2.5 Antibacterial activities of Cu nanowires. Antibacterial efficiency of samples against (A) <i>S. aureus</i> and (B) <i>E. coli</i> bacterial cells as a function of the contact time of 1, 3, 6, 24 hours. The bars indicate the standard errors. (C) Photos of petri dishes with <i>S. aureus</i> and <i>E. coli</i> bacteria cultivated on LB agar covered with bacterial suspension which was in contact with samples and control for 6 hours.....	57

Figure 3.1 Schematic fabrication of bimetallic Cu/Au nanostructures. The reaction temperatures of 220 °C is anticipated to form Cu nanowires via Cu ⁺ disproportionation, whereas 140 °C, 220 °C and 300 °C are anticipated to form various bimetallic Cu/Au nanostructures as labelled as 220/140, 220/220 and 220/300 °C, respectively.	60
Figure 3.2 (A) TEM image of uniform gold nanoparticles prepared by reacting 0.1 mmol of AuBr ₃ in oleylamine at 140 °C for 30 minutes. (B) XRD pattern of the spherical Au nanoparticles with fcc structure (JCPDS #04-0784).....	63
Figure 3.3 Anisotropic growth of Cu nanowires by the controlled disproportionation of CuCl in oleylamine at 220 °C (A-B) for the subsequent formation of Cu/Au nanostructures after reaction with AuBr ₃ at 140 °C (C-D). (A) Low magnification SEM image of Cu nanowires and the magnified TEM image at inset. (B) XRD pattern of Cu nanowires. (C) High magnification SEM image. (D) XRD pattern of Cu/Au nanostructures.	64
Figure 3.4 (A-B) TEM images, (C-E) TEM EDX mapping of bimetallic Cu/Au nanotubes and (F) line scanning across bimetallic Cu/Au nanotubes. (G) Schematic formation of Cu/Au nanotubes with Au-incorporated nanoparticles.....	65
Figure 3.5 (A) SEM image, (B) TEM image, (C) XRD pattern and (D) TEM EDX mapping of Cu/Au nanostructures prepared by heating the as-prepared Cu nanowires at 220 °C after injecting a low amount of Au ³⁺ in the solution.	66
Figure 3.6 (A) SEM image of Cu nanoparticles obtained by disproportionation of CuCl at 220 °C for 30 minutes followed by further heat treatment at 300 °C for 20 minutes. (B) Enlarged region of the blue box in (A). (C) SEM image, (D) high resolution TEM image, (E) XRD pattern, (F) TEM EDX mapping of Cu/Au nanostructures prepared by heating the as-prepared Cu nanowires at 300 °C after injecting a low amount of Au ³⁺ at 220 °C.....	67
Figure 3.7 XRD pattern of the (A) Cu/Au nanotubes and (B) Cu/Au nanostructures after annealing in vacuum at 220 °C.	69

Figure 3.8 CV profiles of Cu nanowires and Cu/Au nanostructures on FTO substrates as electrodes at a potential window of 0-0.7 V and a scan rate of 50 mV s⁻¹ without (--- - dash line) and with (— solid line) 3.0 mM of glucose in 0.1 M sodium hydroxide solution. (A) Pristine Cu nanowires (220 °C) and various Cu/Au nanostructures prepared at (B) 220/140 °C, (C) 220/220 °C and (D) 220/300 °C.....70

Figure 3.9 Electrocatalytic activities of Cu nanowires and Cu/Au nanostructures on FTO substrates as electrodes up to 1800 s. (A) Chronoamperometric curves of Cu nanowires (220 °C) and various Cu/Au nanostructures prepared at 220/140 °C, 220/220 °C and 220/300 °C at a constant potential of 0.6 V upon a successive addition of a glucose solution to obtain a cumulative concentration from 0 to 10.5 mM. Inset shows the enlarged current density region from 0-600 s. (B) The respective calibration curves of Cu nanowires and Cu/Au nanostructures.70

Figure 3.10 Linear range of Cu/Au nanotubes at 3 mol% Au (220/140 °C) as glucose sensors at an applied potential of 0.6 V.71

Figure 3.11 Amperometric response of Cu/Au nanotubes as an electrode at a potential of 0.6 V to various organic species in comparison with 1.0 mM glucose. (A) Various interfering species including 0.02 mM uric acid, 0.1 mM acetamidophenol, 0.1 mM ascorbic acid and 0.1 mM dopamine were tested at an interval of 50 s. (B) Various sugars including fructose, mannose, maltose, sucrose and lactose at a concentration of 0.1 mM were tested sequentially at an interval of 50 s. These concentrations are final concentrations prior to test.72

Figure 3.12 Amperometric response of bimetallic Cu/Au nanotubes as an electrode to 3.0 mM of glucose at a potential of 0.6 V. The stability test was conducted at the beginning of 1 day, 2 days, 1 month and 3 months. The glucose solutions were freshly prepared prior to each test for 1000 s.....73

Figure 3.13 TEM images of (A) Cu/Au@1% and (B) Cu/Au@0.1% nanostructures prepared by heating Cu nanowires at 140 °C after the

introduction of a lower level of Au³⁺ with a molar ratio of Au³⁺/Cu⁺ at 1:100 and 1:1000, respectively.....74

Figure 3.14 Electrocatalytic activities of different Au-incorporated Cu nanowires with different incorporation levels of 0.1, 1 and 3 mol% Au on FTO substrates as electrodes up to 1800 s. (A) Chronoamperometric curves of Cu nanowires (220 °C) and Cu/Au nanostructures prepared at 220/140 °C at a constant potential of 0.6 V upon a successive addition of a glucose solution to obtain a cumulative concentration from 0 to 10.5 mM. Inset shows the enlarged current density region from 0-600 s. (B) The respective calibration curve of Cu nanowires and Cu/Au nanostructures.75

Figure 3.15 Linear range of Cu/Au porous nanowires at 1 mol% Au as glucose sensors at an applied potential of 0.6 V.76

Figure 3.16 CV profiles of different composition Au-incorporated Cu nanowires on FTO substrates as electrodes at a potential window of 0-0.7 V (vs. Ag/AgCl) and a scan rate of 50 mV s⁻¹ without (---- dash line) and with (— solid line) 3.0 mM of glucose. (A) Molar ratio of Au/CuCl at 1:100 (i.e., 1 mol% Au) and (B) molar ratio of Au/CuCl at 1:1000 (i.e., 0.1 mol% Au).76

Figure 3.17 (A) TEM of as-synthesized Ru nanoparticles and (B) XRD of as-synthesized and annealed Ru nanoparticles from 150 to 700 °C in Ar atmosphere.77

Figure 3.18 TEM image of bimetallic Cu/Ru nanowires prepared by reacting Cu nanowires with 0.1 mmol of RuCl₃ in oleylamine at 270 °C and enlarged surface of the nanowires at inset. (B) XRD pattern of the as-synthesized Cu/Ru nanowires with Ru JCPDS # 006-0663.....78

Figure 3.19 Electrocatalytic activities of Cu nanowires and Cu/Ru nanowires on FTO substrates as electrodes up to 1800 s. (A) Chronoamperometric curves of Cu nanowires (220 °C) and Cu/Ru nanostructures prepared at 220/270 °C at a constant potential of 0.6 V upon a successive addition of a glucose solution to obtain a cumulative concentration from 0 to 10.5 mM. Inset shows the enlarged current density region from

0-600 s. (B) The respective calibration curves of Cu nanowires and Cu/Ru nanowires.78

Figure 4.1 Aminolysis reaction between terbium-zirconia carboxylate complexes and primary amine.84

Figure 4.2 Emission spectra of Tb-incorporated ZrO₂ nanoparticles excited at 257 nm: (A) 5-50 mol% and (B) 60-100 mol% of Tb³⁺ in ZrO₂. (C) Maximum emission intensity at ⁵D₄→⁷F₅ transition (545 nm, excited as 257 nm) as a function of Tb³⁺ composition ranging from 5-100 mol% of Tb³⁺ in ZrO₂. Insets show the photograph of 50 mol% (1.9×10¹⁷ particles/ mL) ZrO₂:Tb³⁺ colloidal dispersion in hexane excited on a 302 nm UV illuminator.85

Figure 4.3 (A) Schematic diagram of energy transfer from Zr⁴⁺ to Tb³⁺. The up solid arrow represents photoexcitation and the down dash arrows denote emission. (B) Room temperature excitation spectrum of 50 mol% ZrO₂:Tb³⁺ nanoparticles monitored at 545 nm with concentration fixed at 1.9×10¹⁷ particles/ mL in hexane. The yellow highlighted region represents the f-d transition.86

Figure 4.4 Excitation spectra of Tb-incorporated ZrO₂ nanoparticles excited at 545 nm: (A) 5 - 50 mol% and (B) 60-100 mol% of Tb³⁺ in ZrO₂. (C) Maximum excitation intensity at 4f⁸-4f⁷5d¹ transition (257 nm, excited as 545 nm) as a function of Tb³⁺ composition ranging from 5-100 mol% of Tb³⁺ in ZrO₂.88

Figure 4.5 TEM EDX of 50 mol% ZrO₂:Tb³⁺ nanoparticles.88

Figure 4.6 (A) Room temperature excitation spectra of as-synthesized 50 mol% ZrO₂:Tb³⁺ nanoparticles (λ_{em} at 545 nm) with different concentrations in hexane (no. of particles/ mL) as labeled with 1 to 20 times, corresponding to dilution factor with respect to concentration ranging from ~1.5×10¹⁸ to ~9.4×10¹⁵ particles/ mL. Inset shows the TEM image of ZrO₂:Tb³⁺ nanoparticles with average diameter of 2 nm. (B) Effect of the interparticle distance of 50 mol% ZrO₂:Tb³⁺ nanoparticles on luminescent intensity. Luminescent intensity is obtained from the excitation maxima of different

concentration monitored at 545 nm. The inset shows the schematic illustrations of the $\text{ZrO}_2:\text{Tb}^{3+}$ nanoparticles dispersed in hexane at different concentrations.....90

Figure 4.7 Sensitivity of 50 mol% $\text{ZrO}_2:\text{Tb}^{3+}$ nanoparticles responding to pesticides in the range of 1 to 5 ppm. Concentration of $\text{ZrO}_2:\text{Tb}^{3+}$ nanoparticles is fixed at 6.3×10^{16} particles/mL. (A) Excitation spectra of $\text{ZrO}_2:\text{Tb}^{3+}$ nanoparticles responding to nitrobenzene. (B) Luminescent quenching upon doping with different pesticides. (C) Luminescence stability.91

Figure 4.8 XRD diffraction pattern and their respective 2θ (111) as a function Tb^{3+} content of ZrO_2 , Tb -incorporated ZrO_2 nanoparticles with Tb^{3+} content ranges from 5-90 mol% of Tb^{3+} in ZrO_2 and Tb_2O_3 . (A-B) as-synthesized, (C-D) annealed at 500 °C, (E-F) 700 °C. The standard JCPDS file of Tb_2O_3 (23-1418) and ZrO_2 (49-1642) are shown on top and bottom respectively of the XRD diffraction plot.94

Figure 4.9 Schematic illustration of amorphous (as-synthesized) and crystalline (500 °C) $\text{ZrO}_2:\text{Tb}^{3+}$ matrix in 25, 50 and 75 mol% of Tb^{3+} in ZrO_294

Figure 5.1 (A) Schematic aminolytic synthesis of oleate-coated $\text{TiO}_2:\text{Eu}^{3+}$ nanoparticles at 290 °C through the nucleophilic attack of $-\text{NH}_2$ (oleylamine) to $-\text{C}=\text{O}$ (metal oleates) to form amide. (B) Schematic illustration and (C) TEM image of 50% $\text{TiO}_2:\text{Eu}^{3+}$ nanoparticles.103

Figure 5.2 Luminescence spectra of $\text{TiO}_2:\text{Eu}^{3+}$ nanoparticles. (A) excitation and (B, C) emission spectra of $\text{TiO}_2:\text{Eu}^{3+}$ nanoparticles with tunable molar percentage ranging from 5, 10, 25, 40, 50, 60, 75, to 90 mol %.(B) Direct excitation at 396 nm from Eu^{3+} emission centers, and inset is the corresponding emission intensity as a function of molar concentration. (C) Energy-transfer excitation at the maximum peaks (341, 341, 341, 341, 337, 333, 326, and 320 nm) for the different concentration-tunable $\text{TiO}_2:\text{Eu}^{3+}$ nanoparticles respectively, and inset is the corresponding emission intensity as a function of molar concentration. The sharp second harmonic emission peak of 95% $\text{TiO}_2:\text{Eu}^{3+}$ nanoparticles cannot be removed by the filters because it has a large overlap with the energy transfer excitation wavelength.105

Figure 5.3 (A) XRD analysis of as-synthesized TiO₂ and 50% TiO₂:Eu³⁺ nanoparticles and after annealing at 500 and 1000 °C. (B) Room-light optical (top row) and UV-excited PL (bottom row) images of 50 mol% TiO₂:Eu³⁺ nanoparticles: as synthesized at 290 °C, after annealing at 500 °C and 1000 °C for 3 hours. 106

Figure 5.4 Comparative excitation and emission spectra of 50 mol% TiO₂:Eu³⁺, ZrO₂:Eu³⁺, and Y₂O₃:Eu³⁺ nanoparticles. 107

Figure 5.5 Schematic diagram showing the proposed energy transferring mechanism in TiO₂:Eu³⁺ nanoparticles: → UV photons are absorbed by the TiO₂ band gap; --→ non-radiated relaxation to the TiO₂ surface states; ⇒ energy transferring to the crystal-field states of Eu³⁺ ions, — which causes the fluorescence. — Emission spectra of 50% SiO₂:Tb³⁺ and 50% ZrO₂:Tb³⁺ nanoparticles under respective maximum energy transfer excitation at 321 nm and direct excitation of Tb³⁺ ions at 488 nm. 108

Figure 5.6 (A) Optical photos of ZrO₂:Tb³⁺/green and TiO₂:Eu³⁺/red, nanoparticles in glass vials. (B) SEM image of PLGA encapsulated ZrO₂:Tb³⁺ microparticles. (C) Confocal images of PLGA encapsulated ZrO₂:Tb³⁺ microparticles and (D) confocal images of PLGA encapsulated TiO₂:Eu³⁺ microparticles. 109

Figure 5.7 (A-C) Cellular imaging, (A-B) ZrO₂:Tb³⁺, (C) TiO₂:Eu³⁺ counterstained with dye molecules. (D) In vitro cell viability of MCF-7 cells incubated with PLGA encapsulated ZrO₂:Tb³⁺ microparticles at different concentrations for periods of 24 hours. 110

Publications

1. "Temperature and chemical bonding-directed self-assembly of cobalt phosphide nanowires in reaction solutions into vertical and horizontal alignments", Shuang Yuan Zhang, Enyi Ye, Shuhua Liu, Suo Hon Lim, **Si Yin Tee**, Zhili Dong and Ming-Yong Han, *Adv. Mater.*, 2012, 24 (32), 4369-4375.
2. "Preparation of porosity-controlled calcium carbonate by thermal decomposition of volume content-variable calcium carboxylate derivatives", Hai-Dong Yu, **Si Yin Tee** and Ming-Yong Han, *Chem. Commun.*, 2013, (49), 4229-4231.
3. "Effect of La-Doping on optical bandgap and photoelectrochemical performance of hematite nanostructures", Ning Li, Sundaramurthy Jayaraman, **Si Yin Tee**, Palaniswamy Suresh Kumar, Coryl Jing Jun Lee, Siao Li Liew, Dongzhi Chi, Andy Hor, Seeram Ramakrishna and He-Kuan Luo, *J. Mater. Chem. A*, 2014, (2), 19290-19297.
4. "Structures, mechanical properties and applications of silkfibroin materials", Leng-Duei Koh, Yuan Cheng, Choon Peng Teng, Yin Win Khin, Xian-Jun Loh, **Si Yin Tee**, Bee Jin Low, Enyi Ye, Hai-Dong Yu, Yong-Wei Zhang, and Ming-Yong Han, *Prog. Polym. Sci.* 2015, (46), 86–110.
5. "Fabrication of Bimetallic Cu/Au Nanotubes and Their Sensitive, Selective, Reproducible and Reusable Electrochemical Sensing of Glucose", **Si Yin Tee**, Enyi Ye, Pei Hua Pan, Coryl Jing Jun Lee, Hui Kim Hui, Shuang-Yuan Zhang, Leng Duei Koh, Zhili Dong and Ming-Yong Han, *Nanoscale*, 2015, (7), 11190-11198.
6. "Cobalt sulfide nanoparticles decorated on TiO₂ nanotubes via thermal vapor sulfurization of conformal TiO₂-coated Co(CO₃)_{0.5}(OH)•_{0.11}H₂O core-shell nanowires for energy storage applications", Hong Fei Liu, Ming Lin, June Lay Ting Ong, **Si Yin Tee**, Dongzhi Chi, Yadong Wang, *Rsc Adv.*, 2015, 5, 48647-48653.
7. "Optimized Fabrication of Amorphous Ruthenium Nanoparticles for Enhanced Electrochemical Water Splitting", **Si Yin Tee**, Coryl Jing Jun Lee, Saman Safari

Dinachali, Szu Cheng Lai, Evan Laurence Willaims, He-Kuan Luo, Dongzhi Chi, Andy Hor, Ming-Yong Han, *Nanotechnology*, 2015, 26, 415401.

8. "En route to intrinsically toughest silk", Leng-Duei Koh, Yuan Cheng, **Si Yin Tee**, Choon Peng Teng, Yin Win Khin, Michelle Dela Cruz Regulacio, Hai-Dong Yu, Gui-Jian Guan, Enyi Ye, Shu-Hua Liu, Xian-Jun Loh, Yong-Wei Zhang, and Ming-Yong Han, submitted to *Nature Mater*.

9. "Amorphous Rare Earth-Incorporated Metal Oxide Nanoparticles: Composition- and Interparticle Distance-Dependent Luminescence and Chemical Sensing Application", **Si Yin Tee**, Enyi Ye, Choon Peng Teng, Shan Jiang, Yin Win Khin, Hui Ru Tan, Poh Chong Lim and Ming-Yong Han, manuscript in preparation.

10. "Systematic Screening and Multicolor Bioimaging of Highly Luminescent Ternary Rare Earth – Incorporated Metal Oxide Nanoparticles", Enyi Ye, **Si Yin Tee**, Yin Win Khin, Choon Peng Teng, and Ming-Yong Han, manuscript in preparation.

Patents

“Interparticle Distance-Dependent Sensing using Rare Earth-Incorporated Metal Oxide Nanoparticles”

Inventors: **Si Yin Tee**, Enyi Ye, Yin Win Khin, Suo Hon Lim, Ming-Yong Han

Application No: 13/420,523 (US)

“Solar-Driven Electrolytic Water Splitting using Amorphous Ruthenium Nanoparticles as Electrocatalyst”

Inventors: **Si Yin Tee**, Ming-Yong Han, He-Kuan Luo, Dongzhi Chi, Andy Hor

Application No: 10201402950V (SG)

“Dicobalt Phosphide Nanostructures as Water Splitting Electrocatalyst”

Inventors: Shuang Yuan Zhang, **Si Yin Tee**, Ming-Yong Han, Kwok Wei Shah, Chin Sheng Chua, Dongzhi Chi, Andy Hor

Application No: 10201505483T (SG)

Chapter 1

Background and Significance

1.1 Introduction to metal-based nanostructures

Metal-based nanostructures are materials typically defined at a scale range of 1 and 100 nm with at least one dimension. The metal-based nanostructures generally cover the range from transition metal, alloys, oxides, chalcogenides to pnictides. They have received tremendous interests owing to their extremely small feature size for wide applications which is more superior to their bulk counterparts. Their unique size and shape-dependent properties are promising for widespread commercial applications such as electronics, information storage, biomedical devices, personal care products, as well as environmental and energy technologies.¹⁻⁶ Here, the introduction is focussed on the synthetic methods used to develop transition metals and metal oxide nanostructures, factors influencing size and shape, and a survey of potential applications in biomedical and bioanalytical field. In this respect, discussion will be highlighted on the selected metal and metal oxides such as Fe, Cu, Ag, Au, Ru (transition metals), Ag/Pd, Ag/Au, Pt/Pd, Cu/Au, Cu/Pd, Cu/Pt, Cu/Ru (bimetallic metals), TiO₂, Fe oxides, Cu oxides (transition metal oxides), Eu₂O₃ and Tb₂O₃ (rare earth metal oxides). After which, a host of current and potential uses of nanostructures in the bioapplication will be described.

1.11 Metals

The elements in the centre of the periodic table, between groups 2 and 3, are called the transition metals (Figure. 1.1). The atom of these elements has an incomplete d sub-shell, or which can give rise to cations with an incomplete d sub-shell. They are the metals which make the transition to using the d-orbitals for their bonding, hence they are sometimes called the d-block elements. They are ductile, malleable, and conduct electricity and heat. Their valence electrons are found in more than one shell and that is the reason they have more than one oxidation number. There are more than 20 elements in the transition metals category, special attention is highlighted here on Cu, Ag, Au and Ru nanostructures fabrication and their properties. There are a large number of synthetic methods for developing different types of transition metal nanostructures with well-controlled dimensions. This includes hydro/solvothermal methods, seed/template-mediated synthesis, polyol synthesis and electrochemical synthesis, which the ultimate goal of these fabrication methods is to introduce new nanostructures and improve the existing ones for better functionalities. At present,

reaction parameters can be flexibly tuned to achieve various structures, which triggered great effort in the development of chemical controllable metal oxides synthesis. In this aspect, more attention is devoted to the progress of metal oxides nanostructures fabrication of Ti, Fe and Cu including the diverse properties of these nanostructures.

1.13 General synthetic methodology

The design and synthesis are crucial for fundamental research and technology development which remains a significant ongoing challenge. The distinct properties of nanoscaled materials that differentiate from their bulk are the increase in the surface area to volume ratio. The benefit of having large surface area to volume ratio is that the percentage of surface atoms becomes significant and this can lead to an increase in reactivity of the material. This provides enhanced opportunity for catalysis as catalytic chemical reactions occur at surfaces.^{11, 12} The first scientific study of inorganic materials dates back to 19th century. In 1856, Michael Faraday pioneered the preparation of colloidal Au solution by reducing gold chloride with phosphorus in water.¹³ Later, The well-known Stöber preparation for colloidal silica was developed in the late 1960s.¹⁴ Around the same time, Enüstün and Turkevich prepared the tunable sizes of spherical nanoparticles of gold and silver by the reduction of gold or silver salts by citrate in aqueous solutions in 1963¹⁵, also Ferrofluid (colloidal suspension of iron oxide nanoparticles in organic oil or water) was developed by NASA.¹⁶ In the 1970s, some of the first commercial products containing nanomaterials (TiO₂ or ZnO nanoparticles in sunscreen; Pt, Pd, Rh nanoparticles in catalytic converters) entered the market, and over the past two decades, nanomaterials of different inorganic nanomaterials have found an application in niche. Colloidal Pt and Pd nanoparticles have found widespread applications as catalysts in organic synthesis. Ag nanoparticles in antimicrobial agents^{17, 18} and Au nanoparticles have opened up new opportunities for the development of biomedical field.³

Research on nanostructured materials has greatly intensified due to the development of improved synthetic procedures which enable precise control over the size and shape. Many techniques, including both top-down and bottom-up approaches, have been developed and applied for the synthesis of different nanostructures. Top-down approaches generally involve in the use of expensive synthetic pathways that are

industrially non-scalable and nanomaterials produced have a relatively broad size distribution, varied particle shape or geometry. On the other hand, bottom-up approaches are far more popular in the synthesis of nanostructured materials. Wet chemical synthesis is a potential bottom-up method to produce controlled nanostructures in high yield and structural purity with varying size, shape, structure, composition, and surface chemistry. For example, in colloidal nanomaterials preparation, metal nanoparticles are typically prepared in liquid phase by reduction of metal salts with chemical reducing agents.⁷ The size and shape of the metal nanomaterials are typically controlled through the concentration, reducing agents and capping agents.^{4, 19} Spherical metal nanoparticles are usually prepared by the direct reduction of the metal salt with a strong reducing agent, such as sodium borohydride in the presence of the capping agents.¹⁹ Anisotropic metal nanomaterials, in contrast, are usually prepared using a seeded growth approach, in which a small metal seed particle is exposed to further metal salt in the presence of a weak-reducing agent and a shape-directing agent.¹⁹ Herein, the general route for the colloidal preparation of monodisperse nanoparticles is summarised into five different stages, namely (i) nucleation, (ii) growth, (iii) Ostwald ripening, (iv) surfactant capping and (v) precipitation. The nucleation process represents the initial stage of any crystallization process which refers to the production of monomers from the reaction of precursors. In the synthesis of metal nanoparticles, the concentration of metal atoms increases with time as the precursor is decomposed (typically from heat or sonication). Once the concentration of atoms reaches a point of supersaturation, the atoms start to aggregate into small clusters (i.e., nuclei) via self- (or homogeneous) nucleation. These nuclei will subsequently grow in an accelerated manner and the concentration of metal atoms in solution drops. If the concentration of atoms drops quickly below the level of minimum supersaturation, no additional nucleation events will occur. The existing nuclei will grow into nanocrystal until an equilibrium state is reached between the atoms on the surface of the nanocrystal and the atoms in the solution.^{7, 20} In many cases, Ostwald ripening occurs at a later stage of crystal growth, in which larger crystals are formed at the expense of smaller crystals to reduce the high surface energy. During the formation process, nanocrystals are stabilized by a layer of organic surfactants or capping agents attached to their surface, while the surfactant coating serves to prevent nanocrystal agglomeration, mediate in the growth process, and electronically passivate the nanocrystal surface. There are different types of surfactants

or capping agents ranging from hydrophobic to hydrophilic surfactants, from strong to weak coordinating ligands, and from sterically repulsive long multilayers to short attractive monolayers. Finally, the nanostructured products can be obtained by precipitation and further size-selective separation process can be performed to narrow the size distribution. With this colloidal synthesis, nanostructures with various sizes, shapes, compositions, crystal structures and surfactant coatings have been reported. For example, simple shapes like spheres and cubes, elongated morphologies like rods and wires, and more complicated faceted geometries such as plates and polyhedra, have been constructed.^{21, 22} Hybrid nanostructures (i.e., heterostructures) as well as nanoscale alloys of metals with varying compositions have also been created.^{23, 24}

1.2 Transition metal nanostructures and properties

1.2.1 Elemental transition metals

Copper

Copper with the electronic configuration of $3d^{10} 4s^1$ was the predominant early metal and is still considered as one of the important metal because of its excellent properties such as, ductility, malleability, and conductivity. The synthesis of stable, monodisperse, shaped copper nanostructures have been difficult, partly because of copper's propensity for oxidation. To date, relatively limited attempts have succeeded in synthesizing copper nanoparticles with controllable sizes, shapes, and surface properties. Various polymers or surfactants have been used as reducing agents and capping agents to prepare copper nanostructures in aqueous solutions, although few studies have been reported due to the ease with which the Cu is oxidized. Lisiecki et al. prepared Cu nanoparticles in an aqueous solution of anionic surfactant sodium dodecyl sulfate in a glove box to prevent oxidation.²⁵ Park et al. reported the synthesis of metallic Cu nanoparticles in the presence of PVP via a polyol method in ambient atmosphere. On the basis of XPS, it was demonstrated that the surface of the copper is surrounded by amorphous CuO on the copper surface.²⁶ Despite the advantage of chemical synthesis in aqueous phase can be operated at regular atmosphere and room temperature, the main disadvantages are the broad size distribution of the metal particles produced, and their relatively poor stability. Hence, a variety of organic-phase-based methods have been developed to produce Cu

nanostructures. This route not only yields copper nanoparticles of controllable sizes but also produces shaped nanoparticles, including rods and cubes. Such abilities are important for engineering the sizes and shapes of Cu-based nanoparticles of different compositions for diverse applications.^{27, 28}

Ye et al. demonstrated copper nanowires of 50 nm in diameter were chemically prepared in the organic phase through the controlled disproportionation of Cu^{I} , which involves the initial dissolution of CuCl through coordination with oleylamine in organic solvent and the subsequent disproportionation of the Cu^{I} complexes into metallic Cu^{0} and bivalent Cu^{II} at 200 °C (Figure 1.2).²⁹ The oleylamine-coated copper nanowires can be manipulated to obtain self-assembled copper nanowires facilitated by surface ligand exchange of oleylamine with trioctylphosphine. As a result, trioctylphosphine-coated copper nanowires became stable without a surface oxidation layer as observed on oleylamine-coated copper nanowires after storage in air.

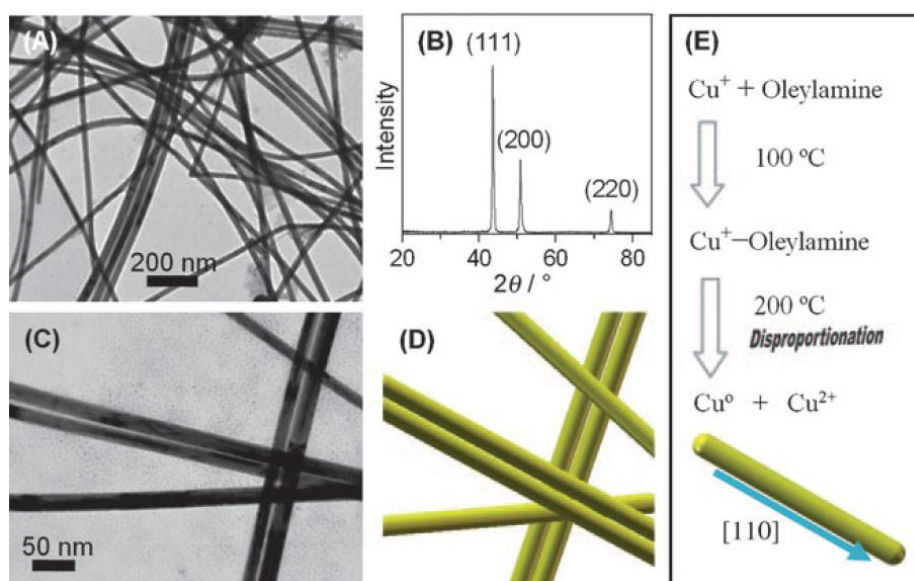


Figure 1.2 Fabrication of oleylamine-coated Cu nanowires by the disproportionational reaction. (A) TEM image and (B) XRD pattern of Cu nanowires. (C) Magnified TEM image and (D) schematic illustration of Cu nanowires. (E) Schematic disproportionational reaction for the formation of Cu nanowires.²⁹

The disproportionation reaction route was extended by Guo et al. who developed spherical or cubic shapes by manipulating the chemical additives (e.g., TOP and TOPO). Monodisperse Cu nanospheres were generated when TOP was introduced as a capping agent, while TOPO could be used for the synthesis of monodisperse Cu nanocubes with tunable sizes.³⁰ The shape selective effect of TOP and TOPO (Figure

1.3) is based on their different coordination effects to Cu^+ . The much stronger coordination of TOP to Cu^+ prevents the metallic ions from being fast reduced to $\text{Cu}(0)$, resulting in nucleation at a higher temperature (260 °C). The high reaction temperature avails the formation of isotropous crystals, which make the seeds grow equally in all directions into spherical-shaped crystals. Whereas, the weaker coordination effect of TOPO to Cu^+ , the nucleation process would happen at a relatively lower temperature (170 °C) leading to the (100) facets of the Cu crystal seeds selectively capped by ligands. As a result, the other facets grew at a faster rate than the (100) facets. This kinetic difference led to the formation of Cu nanocubes instead of nanospheres.

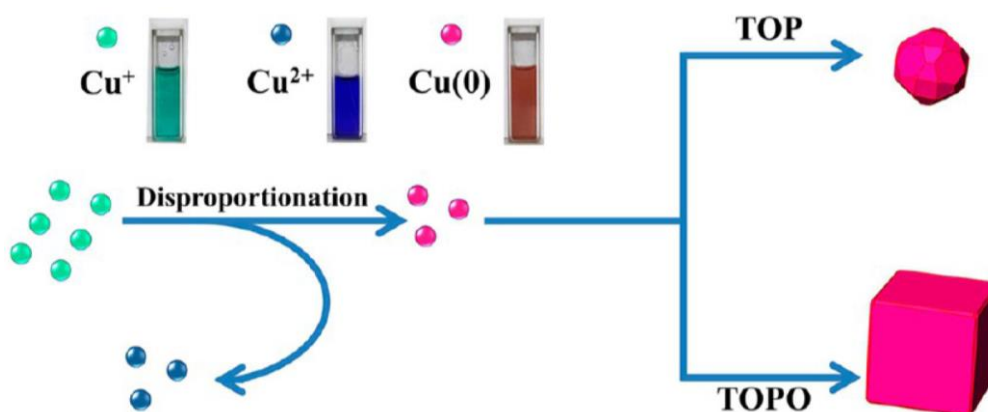


Figure 1.3 Schematic illustration of the shape-selective formation of Cu nanospheres and nanocubes via the disproportionation reaction route.³⁰

Huang et al. developed two distinct shapes copper nanostructures (i.e., cubic and 5-fold twinned nanowires) by the selective use of different additives as the shape controlling agents.³¹ Specifically, NH_4Cl was utilized to generate single crystal nuclei by a Cl^- - O_2 pair that could selectively remove twinned nuclei, which were then shaped into monodispersed cubic nanocrystals. Contrary to the formation of the Cu nanocubes, the addition of RuCl_3 to the reaction led to the formation of the 5-fold twinned nanowires. RuCl_3 could consume O_2 indirectly and prevent the twinned seeds from being oxidized and etched. As a result, the multiply twinned seeds could survive, allowing them to grow into nanowires.

Silver

Historically, Ag metal has been widely used in jewellery and ornaments, high-value tableware and utensils, trade, and as the basis for many monetary systems. In biomedical field, Ag containing materials have been used in wound dressings, as topical treatments to heal burn wounds.^{32, 33} However, the emergence of several antibiotics resulted in the declined usage of these Ag compounds remarkably. Recently, the advances in nanotechnology has opened up a whole new strategies to use Ag metal against a wide array of pathogens due to the capability of modulating metals into their nanosize, which drastically changes the chemical, physical and optical properties of Ag metal. In this aspect, several physical and chemical methods have been used for synthesizing Ag nanostructures, including evaporation-condensation, laser ablation and chemical reduction.^{7, 34-37} In physical processes, metal nanoparticles generated are found to be inefficient in materials and energy used.³⁸

Chemical reduction is the most commonly use method for the preparation of tunable Ag nanostructures in stable colloidal dispersions. Typically, reducing agents (i.e., borohydride, citrate, ascorbate and elemental hydrogen) are used to reduce Ag^+ ions to Ag^0 atoms, followed by agglomeration into oligomeric clusters and eventually to the formation of colloidal Ag particles.³⁹ During the preparation process, protective agents/capping agents (e.g., thiols, amines, acids and alcohols) are used to stabilize nanoparticles by absorbing or binding onto the nanoparticle surface, preventing their agglomeration and losing their surface properties.^{20, 40, 41} Polymeric compounds such as poly(vinyl alcohol), poly(vinylpyrrolidone), poly(ethylene glycol), poly(methacrylic acid) and polymethylmethacrylate have been reported to be effective protective agents to stabilize nanoparticles.³⁹ With the current technology, various shapes of Ag nanostructures (i.e., Ag nanorods, nanowires, nanotubes, nanoplates, nanospheres, nanopolyhedrons) have been well controlled and synthesized successfully as reported.⁴²⁻⁴⁹ Hu et al. proposed a template-less and non-seed process for synthesis of crystalline Ag nanorods and nanowires by reduction of Ag nitrate with tri-sodium citrate in the presence of sodium dodecylsulfonate. It is demonstrated that the concentration of tri-sodium citrate plays a critical role while sodium dodecylsulfonate as a capping agent plays an assistant role in controlling the diameters and aspect ratios (length/width) of the products.⁴⁴ The control and growth of

anisotropic Ag nanomaterials (nanocubes, nanowires and nanosphere) is demonstrated by Wiley et al. through tuning the ratio between the capping agent and the precursor salt in a polymer-mediated polyol process.³⁹ Pastoriza-Santos et al. devised a simple procedure for the synthesis of Ag nanoprisms in N,N-dimethyl formamide using PVP as a stabilizer. The size of the nanoprisms can be controlled through the reaction time at reflux. Although a mixture of nanoprisms and nanospheroids is formed during the synthesis by the method, the latter can be removed through careful centrifugation.⁵⁰

Gold

Traditionally, the chemically inert bulk Au is considered as a safe material for biomedical applications. However, Au has not been considered as a useful catalyst until recent studies have found that nanostructured gold can exhibit unusual catalytic properties in several important reactions when the feature size decreases to be within the nanometer regime.^{51, 52} Its renaissance now leads to enormous amount of research works, and recent studies have been devoted to the development of novel nanostructured gold with various morphologies to exploit the innovative nanoscale chemical effects for diverse applications from biomedical, catalysis, to energy and environmental technologies etc.^{53, 54}

The seed-mediated growth process is a widely used method to yield various size- and shape-controlled gold nanostructures, such as rods, wires, triangles, stars, flowers, and so on. This method is a modified form of Zsigmondy's method, which usually takes place over two steps for making metal nanostructures.⁵⁵ The metal salts are reduced initially with a strong reducing agent and subsequently added to a "growth" solution containing Au precursor and a weak reducing agent, in the presence of structure-directing agents. As a result, the newly reduced Au⁰ can only assemble on the surface of the gold seeds, and no nucleation of new particles occurs in solution leading to the controlled formation of nanostructures. The seed-mediated growth approach for synthesizing high aspect ratio Au nanorods is demonstrated by Jana et al. in good yield.⁵⁶ The citrate-capped gold particles, prepared by the reduction of HAuCl₄ with borohydride, are used as the seed. The aspect ratio of the nanorods is controlled by varying the ratio of seed to metal salt. Murphy et al. synthesized gold nanorods from precursor, HAuCl₄, which is reduced to HAuCl₂ by ascorbic acid in the presence of CTAB and AgNO₃, then citrate-capped spherical gold nanoparticles are added to this

HAuCl₂ solution. These spherical gold nanoparticles catalyze the reduction of Au^I to Au⁰ by ascorbic acid. A three-step procedure in the absence of AgNO₃ allows longer gold nanorods with aspect ratios of up to 25 to be prepared. The gold nanorods formed in the first stage serve as seeds for a second growth, and the latter are in turn used as seeds for the third growth (Figure 1.4).⁵⁷

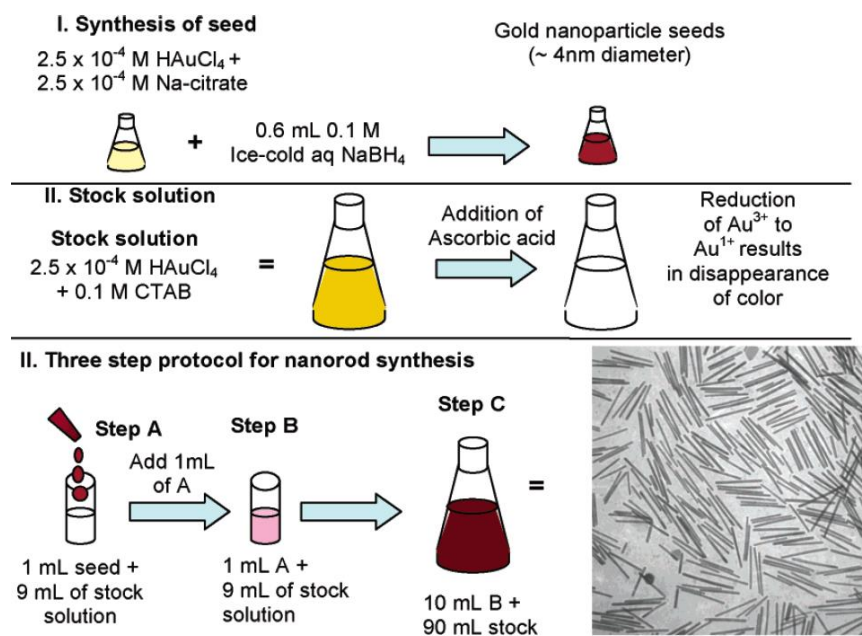


Figure 1.4 Three-step seed-mediated growth approach for preparing Au and Ag nanorods of controlled aspect ratio. TEM of Au nanorods.⁵⁷

The growth direction of the nanoparticles is influenced by the external agents such as molecules or ions result in the formation of various shaped nanoparticles. With the addition of a small amount of iodide ion in a growth solution, the major product of the gold nanostructures formed is notably changed into triangular nanoprisms from nanorods. The major role of the iodide ion is to retard the overall rate of crystal growth, and the iodide adsorption appeared to repress the crystal growth along Au(111) direction, resulting in Au(111)-faced triangular nanoprisms. When the counter anions of the surfactant were replaced with chloride ions, a novel nanostructure (i.e. nanorice) is formed, which demonstrates the effectiveness of the adsorption of halide ions.⁵⁸

There are other factors that influence the size and shape of the nanostructures. The concentration of surfactant molecules is one parameter that plays an important role in the shape determination, since the shape of the micelles formed by the surfactant

during the growth varies with the concentration. The synthetic method of gold nanoprisms developed by Millstone et al. is an example for the dependence of surfactant concentration on the morphology determination.⁵⁹ In this approach, small Au seed nanoparticles of 5 nm are subjected to a three-step growth process in an aqueous solution containing the capping agent CTAB, Au ions, reducing agent (ascorbic acid), and NaOH, resulting in the formation of gold nanoprisms in very good yield. Nanoprisms were formed only when saturated CTAB solution was used, which is a clear indication of the concentration dependence on the morphology of the nanoparticles

The properties of Au change with different size and shape of Au nanostructures. For instance, spherical Au nanoparticles exhibit a range of colors (e.g., brown, orange, red and purple) in aqueous solution as the core size increases from 1 to 100 nm, and generally show a size relative absorption peak from 500 to 550 nm.⁶⁰ This absorption band arises from the collective oscillation of the conduction electrons due to the resonant excitation by the incident photons which is called a “surface plasmon band”.⁶¹ However, this band is absent in both small nanoparticles (< 2 nm) and the bulk material. The aggregation of nanoparticles of appropriate sizes (> 3.5 nm) induces interparticle surface plasmon coupling, resulting in a visible color change from red to blue at nanomolar concentrations.⁶²

Ruthenium

The electronic configuration of elemental Ru is $4d^7 5s^1$, it has the widest state of oxidation states of all elements of the periodic, ranging from -II up to +VIII and thus giving rise to many compounds with interesting and often unique properties. Ru is widely used as a homogeneous catalyst in a variety of organic reactions.^{63, 64} Promoted metallic ruthenium is known to be the best hydrogenation catalyst for dinitrogen and therefore the most active catalyst in ammonia synthesis.⁶⁵ While the oxidised form of Ru, RuO_2 turned out to be an excellent oxidation catalyst in heterogeneous catalysis⁶⁶ and electrocatalysis.⁶⁷

The activity and selectivity of Ru-based catalysts for these structure-sensitive reactions would be strongly dependent on the morphology and surface structures of Ru nanostructures.^{68, 69} Therefore, the morphology and size-controlled synthesis of Ru

nanostructures would build a foundation for tuning and optimizing their catalytic performances in these important reactions. However, up to date, the synthesis of Ru nanostructures remains limited as compared with the finely controlled synthesis of fcc-structured noble metal nanostructures (i.e., Ag, Au, Pd, Pt). Moreover, the relatively low ox/red potentials, along with the hcp structures and different surface adsorption properties of Ru crystals, would raise the difficulty in the morphology-controlled preparation of Ru nanostructures.

The case of ruthenium is interesting because it is one of a very few easily reducible transition metals that crystallizes only in hcp structure. Viau et al. demonstrated the preparation of ruthenium nanoparticles by reduction of RuCl_3 in a liquid polyol.⁷⁰ In this method the liquid polyol acts as solvent for the metal salts, reducing agent, and growth medium for the metal particles. Two important parameters were found to determine the particle size are the temperature and the acetate concentration. The role of acetate ions is to present a strong affinity for ruthenium metal particles and provide them a high enough zeta potential to prevent agglomeration. On the other hand, the higher the temperature, the higher is the nucleation rate, and, for a given concentration of metal, the lower is the mean particle size. Lee et al. reported the preparation of Ru nanoparticles using $\text{RuCl}_3 \cdot x\text{H}_2\text{O}$ precursor in 1,2,3,4-tetrahydronaphthalene (tetralin) and oleylamine.⁷¹ Tetrabutylammonium borohydride was used as reducing agent while the reaction solvent was kept at a 1:1 mixture of oleylamine and tetralin, so that weakly binding oleylamine as a stabilizing agent can be easily removed in the next step. Recently, Yin reported the controlled synthesis of Ru nanostructures with different morphologies and sizes, including ultrathin Ru triangle nanoplates, irregular plates, Ru-capped columns with tunable column lengths, and Ru spherical nanocrystals, through hydrothermal approach in aqueous solutions (Figure 1.5).⁶⁸ The intrinsic structure characteristics, adsorption effects of certain facet-selective agents, and the perturbations of the surrounding environment during the growing process were crucial for the morphology control of Ru nanostructures. For instance, ultrathin Ru nanoplates exposed a large portion of (0001) facets due to the lower surface energy of Ru(0001). The selective adsorption of oxalate species on Ru(10-10) would retard the growth of the side planes of the Ru nanostructures, while the gradual thermolysis of the oxalate species would eliminate their adsorption effects, leading to the shape evolution of Ru nanostructures from prisms to capped columns.

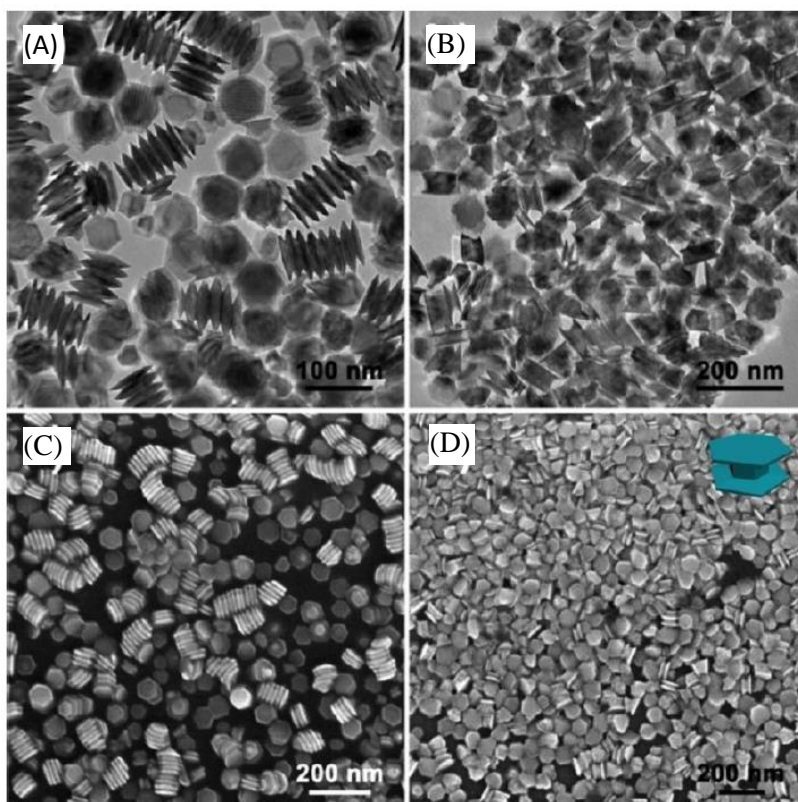


Figure 1.5 (A,B) TEM and (C,D) SEM images of Ru-capped columns prepared under (A,C) 160 °C and (B,D) 150 °C. The inset in (D) is the geometric model of the capped columns.⁶⁸

1.2.2 Bimetallic transition metal nanostructures and properties

Bimetallic nanostructures are a new class of nanomaterials which may have better technological usefulness with distinct properties from those of individual atoms and molecules or bulk matter. They have excelled the monometallic counterpart owing to their improved electronic, optical and catalytic performances.⁷²⁻⁷⁵ The properties and the applicability of these bimetallic nanostructures not only depend on their size and shape, but also on the combination of the component metals (composition) and their fine structure. Generally, bimetallic nanomaterials can be classified according to their mixing patterns. For example, zero dimensional nanomaterials (i.e., nanoparticles) can be classified into three main types (e.g., core-shell, dumbbell, mixed) of mixing patterns as shown in Figure 1.6 (A-C). Core-shell type (1.6A) consist of a shell of one type of atom (Y) surrounding a core of another (X), though there may be some mixing between the shells. Through controlling their core size and shell thickness, their properties can be well modulated.^{76, 77} Dumbbell type (1.6B) consists of X and Y subclusters, which may share a mixed interface. The interface may play an important role in controlling their behaviors.^{78, 79} Mixed X-Y type (1.6C) may be either ordered

or random which the randomly mixed are often termed “alloyed” in the literature. The intermixed pattern is common to many systems.^{80, 81} Similarly, one-dimensional bimetallic nanomaterials (i.e., nanowires, nanorods, nanotubes, etc) have three type of mixing patterns (core-shell, mixed, bamboo-like) as shown in Figure 1.6 (D-F). The core-shell structure (1.6D) can have a clear interface between the core and the shell⁸² or the two kinds of elements are mixed homogeneously in the alloying nanostructure (1.6E).^{83, 84} The two metal elements can also be placed like bamboo to form a one-dimensional structure, where the two kinds of clusters unite alternatively, with elemental distribution anisotropy along the axial direction (1.6F).^{85, 86}

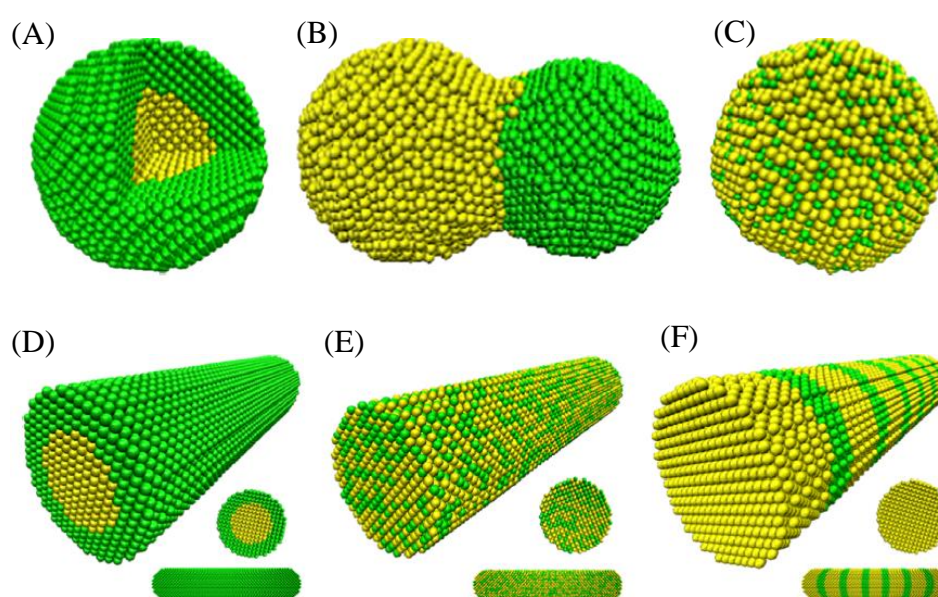


Figure 1.6 Schematic representation of possible mixing patterns of zero-dimensional (A-C) and one-dimensional (D-F) nanomaterial. Zero-dimensional: (A) core-shell, (B) dumbbell, (C) mixed. One-dimensional: (D) core-shell, (E) mixed, (F) bamboo-like.⁸⁷

Much progress has been reported on the controlled synthesis of single-metal nanomaterials (as discussed in the previous section). On the contrary, fabrication of bimetallic nanomaterials with tunable sizes is less developed and limited strategies have been investigated. Traditionally, methods such as the high-temperature melting technique and ball milling yield only bulky materials.^{88, 89} Controlled synthesis of bimetallic colloids can readily be prepared by chemical reduction of the appropriate mixture of salts in the solution phase using reducing agents such as sodium borohydride, hydrazine, and hydrogen.⁹⁰⁻⁹³ During the reduction process, the metal species with the highest redox potential generally precipitates first, forming a core on

which the second component is deposited as a shell.⁹⁰ The sequence of deposition can be changed by performing if the metal with the higher redox potential were bind strongly with a ligand, yielding the inverse-core-shell arrangement. An early example of Ag/Pd nanoparticles (70:30 weight %) fabricated by the co-reduction of Ag and Pd leads to the formation of Pd core Ag shell clusters attributed to the higher redox potential of Pd.⁹⁰ On the contrary, co-precipitation in the ammonia solution containing the two metal salts and hydrazine leads to formation of the reverse Ag core Pd shell cluster because of the stronger binding of NH₃ to Pd than to Ag. When the two metal ions have the similar redox potentials and relatively large enthalpies of mixing, bimetallic alloy particles can be generated.

This synthesis method is also known as galvanic replacement reaction which is a versatile strategy for engineering the architectural metal nanostructures with controllable hollow interiors and porous walls. In the redox process, the oxidised metal thus acts as a sacrificial template for the formation of hollow nanostructures through the galvanic exchange.^{94, 95} This approach has been widely used to produce Au-based hollow nanostructures with different morphologies (i.e., cubic nanoboxes, cubic nanocages).^{72, 96} These hollow nanostructures are attributed to template-engaged hollowing-out mechanism (Figure 1.7). Since the electrochemical potential of Au is more positive than that of Ag (i.e. reduction potential of AuCl₄⁻/Au is 0.99 V vs. SHE and AgCl/ Ag is 0.22 V vs. SHE), Ag nanocubes will act as sacrificial template/reducing agent and Au³⁺ will act as oxidising agent.⁹⁶ During the oxidation reaction, the electrons generated migrate to the Ag nanocube surface, and reduces Au³⁺ to Au⁰. The Au atoms grow epitaxially over the Ag nanocubes since Au and Ag are having the same fcc structure with closely matched lattice constants. In the beginning of the reaction, tiny pits are generated on the surface of the nanocube which allows the ionic species to diffuse continuously in and out of the oxidation sites. As the reaction proceeds, this pit evolves into a deep hole, with its opening at the surface eventually being closed, resulting in a seamless nanobox composed of Au/Ag alloy. Upon adding more amounts of Au³⁺, dealloying of the nanobox happens that leads to the formation of Au-based nanocages with porous walls.⁹⁷

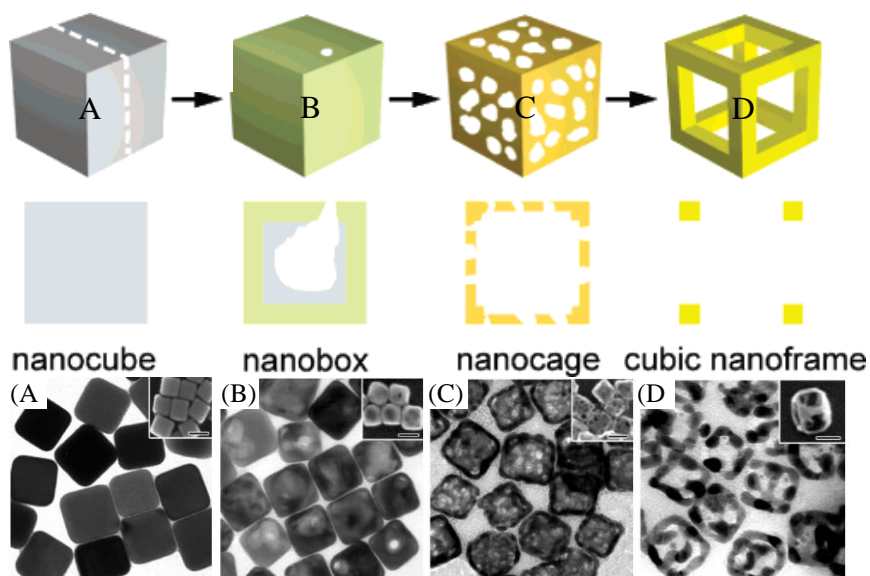


Figure 1.7 Schematic illustrating the formation of a nanocage made of Au/Ag alloy and then a cubic nanoframe made of pure Au by selectively removing the Ag atoms from Au/Ag alloy nanobox. (A) Ag nanocubes, (B) Formation of Au/Ag alloy nanobox, (C) selective removal of the Ag atoms from the nanobox, (D) complete removal of Ag from the nanocage. Corresponding TEM and SEM images (insets) of the Ag nanocube, Au nanobox, Au nanocage, and Au nanoframes, respectively.⁹⁷

Habas demonstrated the use of Pt seeds to direct the epitaxial overgrowth of a secondary metal.⁹⁸ This concept was demonstrated with lattice-matched Pd to produce shape-controlled core-shell particles, and then extend it to lattice-mismatched Au to give anisotropic growth (Figure 1.8).

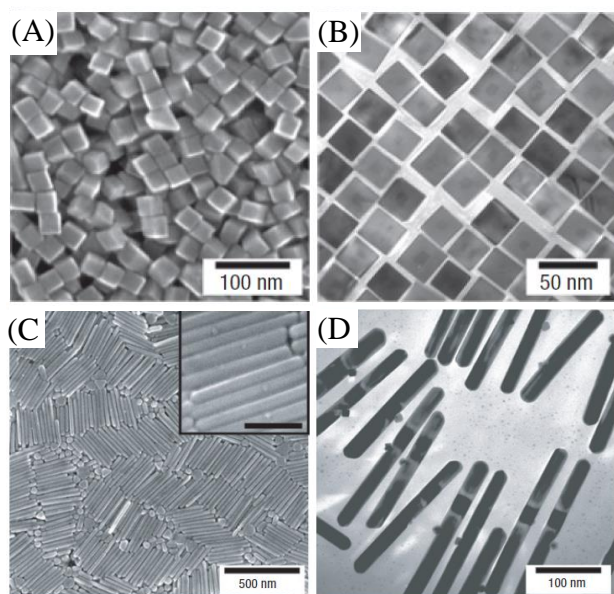


Figure 1.8 SEM (A, C) and TEM (B, D) of the Pt/Pd core-shell nanocubes (A, B) and Pt/Au nanorod (C, D).⁹⁸

Chen et al. reported intermetallic Cu/Au nanoparticles via the diffusion of newly produced Cu atoms into presynthesized Au nanoparticles.⁹⁹ With this method, the size and monodispersity of the sample could be fine-tuned based on those of the Au nanoparticles precursor. Additionally, selective synthesis of Cu/Au and Cu₃Au could also be realized readily by changing the molar ratio of the precursors. The protocol of galvanic replacement reaction has been successfully applied to prepare Cu/Pd and Cu/Pt bimetallic nanotubes. Mohl et al. developed the bimetallic nanotubes by reacting noble metal solutions with Cu nanowires in organic media (Figure 1.9).¹⁰⁰ Ultralong Cu nanowires of several micrometers were used as template material. By controlling the amount of noble metal salt added, nanotubes with different compositions were obtained. After the replacement of Cu with Pt, nanotubes composed of a Pt/Cu alloy were formed. As for the replacement of Cu with Pd, the thickening of the nanotubes was observed indicating that nanotubes composed of Pd nanoparticles were formed.

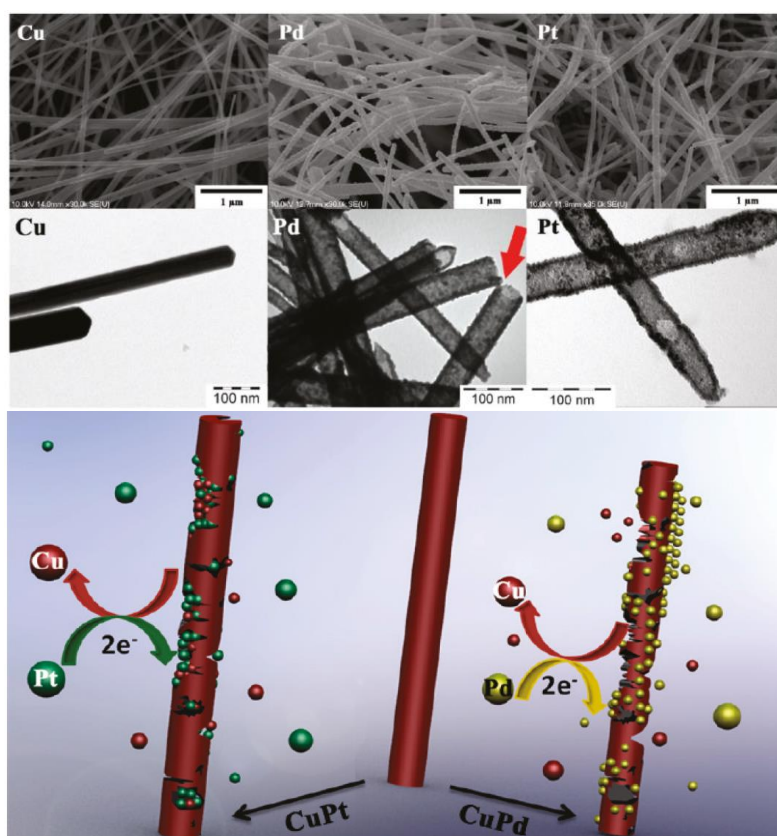


Figure 1.9 SEM (top row) and TEM images (bottom row) of Cu nanowires, Cu/Pd and Cu/Pt nanotubes. The schematic illustrating the formation mechanism of Cu/Pt alloy nanostructures and Cu/Pd bimetallic nanotubes from Cu nanowires.¹⁰⁰

Recently, Huang et al. developed the bimetallic Cu/Ru nanotubes via *in situ* galvanic replacement process.³¹ RuCl₃ plays a critical role in the preparation of Cu nanowires

and alloy structures. When the reaction temperature was further increased after the formation of Cu nanowires, the existing Ru salts can be reduced and react with the preformed Cu nanowires, leading to the *in situ* formation of bimetallic Cu/Ru nanotubes. As the reaction proceeded, nanotubes formed through a combination of galvanic replacement and alloying between Cu and Ru.

1.3 Transition metal oxide nanostructures and properties

Titanium oxide

TiO₂ is one of the most studied transition metal oxides, it occurs in nature in three different polymorphs, which, in order of abundance, are rutile, anatase, and brookite. TiO₂ has attracted much attention since the pioneer demonstration of photocatalytic performance in water splitting in early 1970s.¹⁰¹ It has been followed by extensive research on the fabrication, structure, and applications of TiO₂-based materials.^{102, 103} In fact, most TiO₂ applications were based on its nanoscale morphologies. Among the unique properties of nanoscale materials, the movement of electrons and holes in semiconductor nanomaterials is primarily governed by the well-known quantum confinement, and the transport properties related to phonons and photons are largely affected by the size and geometry of the materials.¹⁰⁴ The large surface-to-volume ratio of nanomaterials can significantly increase the surface reaction sites and might even modulate the catalytic activity of the surface atoms.¹⁰⁵ Thus, enormous efforts have been done to develop nanostructured TiO₂ materials with various morphologies such as nanoparticles, nanorods, nanowires, nanotubes, and other hierarchical nanostructures.^{103, 106}

Numerous routes have been explored to the synthesis of TiO₂ nanostructures from solution-based synthetic approaches (i.e., hydrothermal/solvothermal processes, sol-gel method, and so on). These methods offer several benefits for mass production of nanomaterials including low-cost, simple processing, and good scalability. Lin et al. developed a series of well-defined 3D hierarchical rutile TiO₂ architectures by hydrothermal method simply by changing the concentration of hydrochloric acid used in the reaction.¹⁰⁷ The production of these materials was identified as example of a ledge-wise growth mechanism in a rutile TiO₂ structure. Melcarne et al. applied a solvothermal method to prepare anatase TiO₂ nanorods using Ti(IV)-isopropoxide.¹⁰⁸

The use of benzyl alcohol and acetic acid in the reaction mixture is for a significant dimensional and morphological control over the resulting TiO₂ nanostructures, as well as to devise a simple and scalable synthetic protocol. The rod-like anatase TiO₂ nanostructures were possibly due to the binding of acetic acid to certain crystal facets, where the deposition rates were limited. The formation of anatase phase was attributed to the lower acidity environment and lower pressure due to the higher boiling point of benzyl alcohol compared to the growth conditions of rutile TiO₂ nanorods. Zhang et al. reported a nonhydrolytic route in obtaining highly crystalline anatase TiO₂ nanorods which involves the reaction of titanium alkoxide with an organic ether (Figure 1.10).¹⁰⁹ Briefly, the nucleophilic attack of an amine group on the carbonyl carbon atom of titanium carboxylate derivatives and the chemical modification of reactive molecular precursors with oleic as the chelating ligand. The high-temperature aminolysis of titanium carboxylate (titanium oleate) complexes can be well-controlled by using high-boiling long-chain oleylamine rather than volatile water.

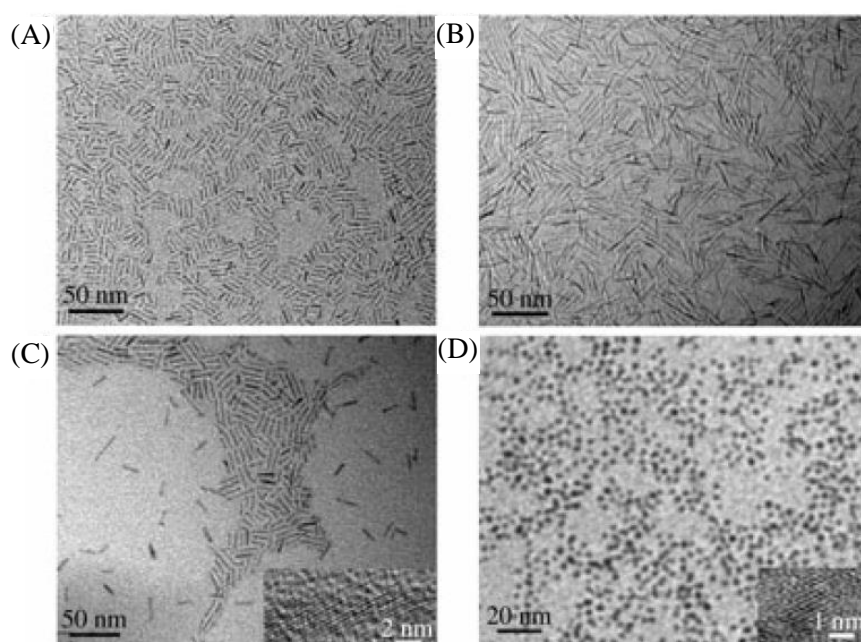


Figure 1.10 TEM images of TiO₂ nanostructures. (A-C) nanorods with different aspect ratio (D) nanoparticles. Inset in parts C and D: HRTEM image of a single TiO₂ nanorod and nanoparticle.¹⁰⁹

TiO₂ nanostructures have been widely applied in many fields involving energy and environmental research as well as biomedical engineering owing to their unique characteristics, comprising low density, large strength-to-weight ratio, photochemical

stability, high catalytic efficiency, excellent biocompatibility, good corrosion resistance, as well as excellent mechanical properties.¹⁰⁶

Iron oxide

Iron oxides are chemical compounds composed of iron and oxygen which are widespread in nature and readily synthesized in laboratory. There are eight iron oxides which are known.¹¹⁰ Several types of these iron oxides have been carried out in the field of magnetic nanoparticles (mostly includes the Fe_3O_4 magnetite, $\text{Fe}^{\text{II}}\text{Fe}^{\text{III}}_2\text{O}_4$, ferrimagnetic, superparamagnetic when the size is <15 nm), $\alpha\text{-Fe}_2\text{O}_3$ (hematite, weakly ferromagnetic or antiferromagnetic), $\gamma\text{-Fe}_2\text{O}_3$ (maghemite, ferrimagnetic), FeO (wüstite, antiferromagnetic), $\epsilon\text{-Fe}_2\text{O}_3$ and $\beta\text{-Fe}_2\text{O}_3$).^{110, 111} Among which magnetite and maghemite possess unique biochemical, magnetic, catalytic properties which equip suitability for specific technical and biomedical applications.¹¹¹

However, it is an ongoing challenge to synthesis iron oxides nanostructures with controlled size, shape, stability, and dispersibility in desired solvents. Magnetic iron oxide nanoparticles have a large surface-to-volume ratio and therefore possess high surface energies. Consequently, they tend to aggregate in order to minimize the surface energies. Moreover, the bare iron oxide nanomaterials have high chemical activity, and are easily oxidized in air (especially magnetite), generally resulting in loss of magnetism and dispersibility. Therefore, it is essential to provide effective surface protection strategies to keep the stability of magnetic iron oxide nanoparticles including grafting of or coating with organic molecules (e.g., small organic molecules or surfactants, polymers, and biomolecules), or coating with an inorganic layer (e.g., silica, metal or nonmetal elementary substance, metal oxide or metal sulphide).¹¹¹

To date, synthetic methods such as co-precipitation, thermal decomposition, hydrothermal and solvothermal syntheses, sol-gel synthesis and microemulsion have been applied to produce magnetic iron oxide nanostructures.¹¹¹⁻¹¹³ The most conventional method for obtaining Fe_3O_4 or $\gamma\text{-Fe}_2\text{O}_3$ is by co-precipitation. This method was first demonstrated by Massart more than 30 years ago,¹¹⁴ the chemistry of synthetic protocol remain the same despite it has gained broad variety of modifications. This method consists of mixing ferric and ferrous ions in a 1:2 molar ratio in highly basic solutions at room temperature or at elevated temperature, usually

under gas protection. The reaction mechanism can be simplified as: $\text{Fe}^{2+} + 2\text{Fe}^{3+} + 8\text{OH}^- \rightleftharpoons \text{Fe}(\text{OH})_2 + 2\text{Fe}(\text{OH})_3 \rightarrow \text{Fe}_3\text{O}_4 \downarrow + 4\text{H}_2\text{O}$. The nucleation of the Fe_3O_4 nucleus is easier when the solution pH is lower than 11, while the growth of the Fe_3O_4 nucleus is easier when the solution pH is higher than 11.

Ahn et al. reported that magnetite nanoparticles prepared from co-precipitation process by the phase transformation of iron oxyhydroxides, rather than the direct reaction of Fe^{2+} and Fe^{3+} in the aqueous phase.¹¹⁵ The co-precipitation method typically involves fast particle formation rates and therefore, particle size and size distribution are difficult to control. Moreover, co-precipitation reactions are usually carried out at room temperature; the obtained iron oxides often exhibit low crystallinity. In order to avoid the limitations of this method, different alternative strategies have been developed, such as nonaqueous thermal decomposition strategies. In comparison to co-precipitation method, higher monodisperse, narrow size distribution and highly crystalline magnetic iron oxides are obtained from high-temperature thermal decomposition of organometallic or coordinated iron precursors in organic solvents, which display superior properties to those obtained by co-precipitation, since nucleation can be separated from growth and complex hydrolysis reactions can be avoided.^{116, 117}

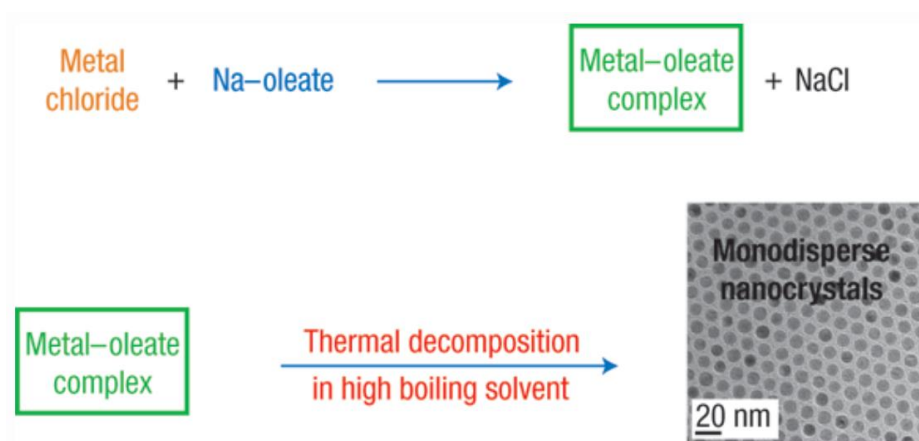


Figure 1.11 Schematic illustrating the synthesis of monodisperse nanoparticles. Metal-oleate precursors were prepared from the reaction of metal chlorides and sodium oleate. Thermal decomposition of the metal-oleate precursors in high boiling solvent produced monodisperse nanoparticles.¹¹⁸

Park et al. have reported a synthetic method of obtaining monodisperse nanoparticles by reacting iron chlorides and sodium oleate.¹¹⁸ The formation of iron-oleate complex in 1-octadecene was slowly heated to 320 °C, and was aged at that temperature for 30

min, generating iron oxide nanoparticles (Figure 1.11). The size of the iron oxide nanoparticles was controlled by various heating temperatures and times. The synthetic protocol is a generalized process that can be used to synthesize different kinds of monodisperse nanoparticles.

The thermal decomposition method is often used to prepare iron oxide with different shapes. For example, Palchoudhury et al. demonstrated the preparation of iron oxide nanowhiskers with dimensions of approximately 220 nm were successfully synthesized by selectively heating an iron oleate complex.¹¹⁹ Such nanostructures resulted from the difference in the ligand coordination microenvironments of the Fe^{III} oleate complex. The study of iron oxide nanostructures by thermal decomposition were further extended by Zhou et al. who recently reported iron oxide nanostructures with various shapes and surface structures by thermal decomposition of iron oleate in the presence of sodium oleate (Figure 1.12).¹²⁰ In a mild condition using 1-octadecene as solvent, sodium oleate may preferentially bind to Fe₃O₄ (111) facets and lead to the formation of Fe₃O₄ (111) facet exposed iron oxide plates, truncated octahedrons, and tetrahedrons. While in a high-boiling temperature tri-n-octylamine solvent, Fe₃O₄ (100) facet exposed iron oxide cubes, concaves, multibranches, and assembled structures were obtained by varying the molar ratios of sodium oleate to iron oleate.¹²⁰

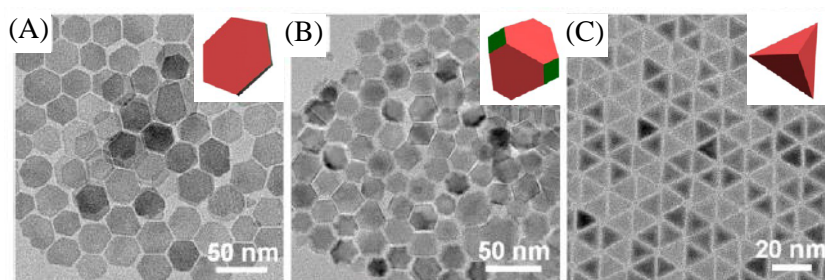


Figure 1.12 TEM images of iron oxides (A) plates, (B) truncated octahedrons, and (C) tetrahedrons.¹²⁰

Hydrothermal or solvothermal synthesis has also been used to grow dislocation-free single crystal particles, and grains formed in this process could have a better crystallinity than those from other processes, and hence hydrothermal and solvothermal synthesis are prone to obtaining highly crystalline iron oxides, including α -Fe₂O₃, γ -Fe₂O₃, and Fe₃O₄ nanoparticles. Hydrothermal and solvothermal route is also a facile and conventional method for obtaining hollow iron oxides nanomaterials. Jia et al. reported the preparation of single-crystalline hematite tube-in-tube

nanostructures by hydrothermal method.¹²¹ It was disclosed that the hematite tube-in-tube nanostructures were formed through a multisite dissolution process of the ellipsoid precursors (Figure 1.13). Moreover, with the hematite products as precursors, magnetite and maghemite tube-in-tube nanostructures were also prepared through a reduction or a reduction and reoxidation process.

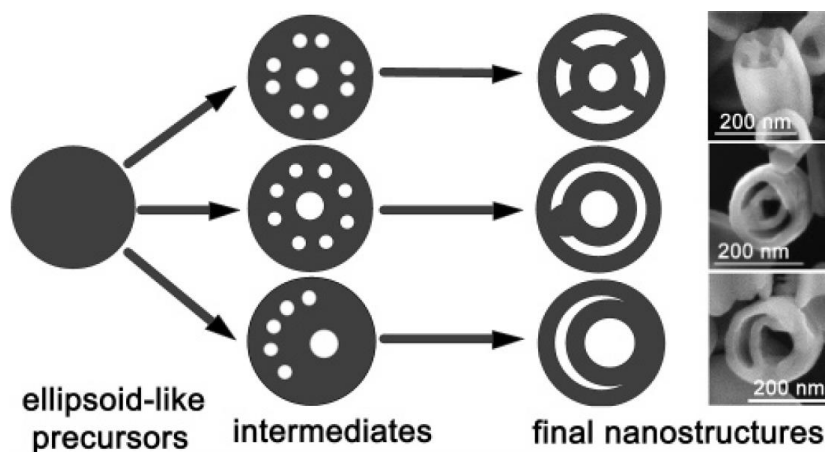


Figure 1.13 Formation process of hematite tube-in-tube nanostructures (top view).¹²¹

Copper oxide

Copper has two natural oxides: cuprous oxide (Cu_2O) and cupric oxide (CuO). Both are semiconductors with band gaps of 2.0 eV and 1.2 eV, respectively. Their band gaps make them good candidates for energy conversion devices and optoelectric devices.^{122, 123} Besides, numerous reports has been extensively studied their antibacterial activities relating to their particle size effect, morphology etc. In addition, CuO nanostructures are widely used in electrochemical studies relating to glucose¹²⁴ and H_2O_2 sensing,¹²⁵ hence extensive efforts have been put forward to address the size and shape control of CuO nanomaterials for the improvement in the cyclability of CuO -based electrodes.

Copper oxide nanostructures can be prepared using different approaches, thus the copper oxide nanostructures can have different morphologies or even chemical compositions. The composition of copper oxide can be cupric oxides (CuO) or cuprous oxides (Cu_2O), they can even be a mixture of crystalline and amorphous copper oxides (i.e., a cuprous oxide polycrystalline structure with a cupric amorphous sheath).¹²⁶ Therefore, the selection of preparation method is important in order to get the optimum

result. The advancement of nanotechnology enable copper oxides nanomaterials to be prepared in a variety of morphologies such as nanoparticles, nanoneedles, nanowhiskers, nanowires, nanoshuttles, nanorods, nanotubes, nanoleaves, and nanoribbons by using the solution-based approach and vapor phase growth techniques.¹²⁷⁻¹³¹ Jiang et al. demonstrated the synthesis of uniform CuO nanowires with controllable diameters in the range of 30-100 nm and with lengths of up to 15 μm by heating copper substrates in air.¹²⁷ Wang et al. synthesized Cu₂O nanowires via a reduction route in the presence of polyethylene glycol at room temperature.¹³² Firstly, Cu(OH)₂ nanowires were obtained from the reaction of CuCl₂, NaOH and shaping agent, polyethylene glycol. Subsequently, hydrazine was employed as the reducing agent to reduce Cu(OH)₂ to Cu₂O. The resulting Cu₂O nanowires were in large aspect ratio of 8 nm in diameter and 10-20 μm in length. Li et al. reported a facile method to selectively synthesize ultralong Cu(OH)₂ and CuO nanowire bundles on a large scale.¹³³ By monitoring the growth stages, under the action of polyethylene glycol, the Cu(OH)₂ and CuO nanowires were first formed through oriented attachment of colloidal particles, then through side self-assembly leading to nanowire bundles, and finally to CuO nanoleaves. Polyethylene glycol prevents the random aggregation of colloidal particles toward CuO nanoleaves and also helps to orientate nanowire growth by the coalescence and alignment in one direction of the colloidal particles. In the absence of polyethylene glycol, nanoleaves are formed by an Ostwald ripening process.

1.4 Rare-earth metal oxide nanostructures and properties

In the periodic table of elements, lanthanides are the fifteen elements that ranging from lanthanum to lutetium. The element yttrium and scandium have some of the same properties as the lanthanides, and the lanthanides together with yttrium and scandium form the group of *rare earth* (RE) as shown in Figure 1.14. They acquired their name because they were considered scarce when they were discovered in the late 18th century. Later it was found that RE are not less abundant in nature than Sn or Ag. RE ions are commonly found in +3 oxidation state despite +2 and +4 oxidation states have been found for some elements of the lanthanide ions, +3 states is the most stable under normal conditions for all of the elements in the series. The trivalent RE ions are commonly applied as the luminescent centers in nanomaterials, except Sc³⁺, Y³⁺, La³⁺

and Lu^{3+} are frequently applied as host materials due to the absence of unpaired 4f electrons. For luminescent ions from Ce^{3+} to Yb^{3+} , the partially filled 4f shell is shielded by $5s^25p^6$ sub-shells, resulting in intrinsic spectroscopic character with less interference from the chemical surroundings. Furthermore, the shielding effect could also account for the narrow-band emission and long lifetimes of the excited states.¹³⁴

Group	1	2	3	4	5	6	7	8	9	10	11	12	13	14	15	16	17	18
Period																		
1	H																	He
2	Li	Be											B	C	N	O	F	Ne
3	Na	Mg											Al	Si	P	S	Cl	Ar
4	K	Ca	Sc	Ti	V	Cr	Mn	Fe	Co	Ni	Cu	Zn	Ga	Ge	As	Se	Br	Kr
5	Rb	Sr	Y	Zr	Nb	Mo	Tc	Ru	Rh	Pd	Ag	Cd	In	Sn	Sb	Te	I	Xe
6	Cs	Ba	Lu	Hf	Ta	W	Re	Os	Ir	Pt	Au	Hg	Tl	Pb	Bi	Po	At	Rn
7	Fr	Ra	Lr	Rf	Db	Sg	Bh	Hs	Mt	Ds	Rg	Cn	Uut	Uuq	Uup	Uuh	Uus	Uuo
*Lanthanoids				La	Ce	Pr	Nd	Pm	Sm	Eu	Gd	Tb	Dy	Ho	Er	Tm	Yb	
**Actinoids				Ac	Th	Pa	U	Np	Pu	Am	Cm	Bk	Cf	Es	Fm	Md	No	

Figure 1.14 The periodic table of elements. The rare earth metals are boxed in red.

RE oxides are often regarded as an important class of compound and continuous efforts have been devoted to the research field of RE oxide nanomaterials to explore new properties and application. The classical method commonly used in industrial is by thermal pyrolysis of RE carbonates or oxalates at high temperature (600-1000 °C). This method usually results in fine powders with a relatively wide size distribution. After sintering, the surface OH^- and other solvent related species are generally removed, therefore, powder may exhibit better luminescence efficiency and longer decay time. The combustion techniques, such as the solution combustion, spray pyrolysis, flame pyrolysis, utilize the high temperature to decompose the precursor and crystallize the fine powders. Usually, large quantities of highly porous or fine particles are produced with varied composition and doping, while the volatile quenching impurities are removed. However, the particles also exhibit a wide size distribution which might be partially alleviated by size selection process. There are other conventional methods related to post heat treatment from precipitates from the aqueous solutions. For example, the ambient aqueous routes and the hydrothermal methods at

elevated temperature usually lead to RE precipitates like hydroxides, carbonates, instead of oxides. In fact, the hydrothermal treatment of RE oxide powders results in a hydration process to form hydroxides. Subsequently, the precursor could be used to produce RE oxide with post annealing at varied temperatures and in appropriate atmosphere.

The colloidal synthesis in nonhydrolytic approach (i.e., oleic acid, trioctylphosphine oxide and poly alcohols) involve in the thermolysis of organometallic precursors or precipitation. The experimental parameters such as ligands, precursors, and reaction temperature can be controlled to tune the kinetics and thermodynamics of the nucleation and growth of nanocrystals are tuned leading to size and shape controlled nanomaterials. High quality monodisperse and uniformly sized colloidal nanostructures with varied shapes, including nanoparticles, nanorods, nanowires, nanotubes, and nanoplates were obtained through this approach. An earlier work was demonstrated by Si et al. using nonhydrolytic approach in oleic acid/oleylamine/1-octadecene with various RE complexes to develop high-quality RE₂O₃ (La to Lu, Y) nanopolyhedra, nanoplates and nanodisks.^{135, 136} The transformation from the complex precursors to RE₂O₃ was proposed to occur in two stages: first, the formation of rare-earth oleates by ligand exchange in solution, and second, the subsequent decomposition of the oleates into RE₂O₃ catalyzed by the base of oleylamine. Due to the selective adsorption of the capping ligands on certain cubic faces during crystal growth, nano-crystals with different morphologies, such as nanopolyhedra, nanoplates, and nanodisks, were created. Paek et al. reported the synthesis of colloidal cubic Gd₂O₃ nanorings and nanoplates from low-temperature (90 °C) hydrolysis of Gd-(acac)₃ and subsequent *in situ* thermal dehydration of the hydrolyzed precursor-surfactant aggregates at 320 °C.¹³⁷ The synthetic protocol could be extended to other metal oxide systems such as Er and Yb. Han et al. reported the synthesis of heavy lanthanide sesquioxide (RE₂O₃, RE= Y, Dy, Ho, Er) nanobelts by thermolysis of solid RE nitrate hydrates in a dodecylamine/1-octadecene mixed solvent system.¹³⁸ The nitrate hydrates showed poor solubility in the mixed solvent, and the heat-transport differences between the liquid and the solid assisted in separation of the nucleation and growth processes.

emitter, thus lead an efficient energy transfer to lanthanide ions. Accordingly, lanthanide-doped inorganic materials can exhibit efficient luminescence emissions from the UV, passing through the whole visible, to the mid-infrared light region upon excitation. Moreover, compared with lanthanide chelates, quantum dots, and organic dye molecules, lanthanide -doped inorganic materials hold all the advantages of a large Stokes shift, a sharp emission spectrum, a long lifetime, high chemical/photochemical stability, low toxicity, and reduced photobleaching.¹⁴⁰

Europium oxide

Europium is one of the most interesting RE activators which is well-known for its red emission. Being a typical member of the lanthanide series, europium usually assumes the oxidation state +3, but the oxidation state +2 is also common (highly reducing). The +2 state has an electron configuration $4f^7$ because the half-filled f-shell gives more stability. As an important activator, Eu^{3+} ions have pure red emission transitions with a series of sharp lines arising from the excited state $5D^0$ to the lower energy state $7F_{0-6}$. The $^5D_0 \rightarrow ^7F_2$ electric dipole transitions around 612 nm are highly hypersensitive, which is highly sensitive to the symmetry of the Eu^{3+} sites in the lattices. $^5D_0 \rightarrow ^7F_1$ magnetic dipole transitions around 590 nm are allowed, which is insensitive to the symmetric environment of the RE ion. The 7F_0 and 5D_0 levels are non-degenerate and the spectra associated with transitions between them should contain as many lines as the number of non-equivalent sites.¹⁴¹ The luminescence decay time of the emitting 5D_0 level (ms) is longer; therefore, Eu^{3+} ions have been widely investigated for applications as phosphors, electroluminescent devices, optical amplifiers and high-density optical storage.¹⁴⁰

The important factor that affects the emission of the Eu^{3+} is the environment in the host lattices. A small difference in host structure can have an important influence on the luminescent properties of Eu^{3+} ion-doped phosphors. Generally, the activators are embedded into the host lattice in low concentrations (<5 mol %) so as to reduce the concentration quenching of luminescence, and not change the crystal structure of the host material.¹⁴⁰ The commonly investigated systems involve Eu^{3+} doped semiconductors (e.g., ZnO ,¹⁴²⁻¹⁴⁴ TiO_2 ¹⁴⁵⁻¹⁴⁷, ZrO_2 ¹⁴⁸), vanadates,¹⁴⁹ fluorides,^{150, 151} and other RE oxides (e.g., Y_2O_3 ,^{152, 153} Gd_2O_3 ^{154, 155}). Li et al. synthesized $\text{TiO}_2:\text{Eu}^{3+}$ nanorods and spindle-shaped nanoparticles through calcination and hydrothermal

process respectively using titanate as the precursor.¹⁴⁶ Under UV light excitation, both the $\text{TiO}_2:\text{Eu}^{3+}$ nanorods and spindle-shaped nanoparticles exhibit the strong red emission. It was found that the luminescence intensity of $\text{TiO}_2:\text{Eu}^{3+}$ nanorods is higher than that of $\text{TiO}_2:\text{Eu}^{3+}$ spindle-shaped nanoparticles due to the increases of the bandgap of the TiO_2 nanorods. Liu et al. developed 5 nm tetragonal $\text{ZrO}_2:\text{Eu}^{3+}$ (10 mol%) nanoparticles in the presence of capping ligands (benzyl alcohol) via a modified solvothermal method.¹⁴⁸ When the typical emissions of Eu^{3+} at 607 nm ($^5\text{D}_0 \rightarrow ^7\text{F}_2$) and were monitored, the PL excitation spectra are dominated by an intense broad excitation band centered at 280 nm, which is ascribed to the host absorption and consistent with the bandgap energy (~ 288 nm) determined from the UV-vis absorption spectrum for pure ZrO_2 nanoparticles, suggesting that the Eu^{3+} emissions can be realized through an energy transfer from the ZrO_2 host to the emitters. The absolute quantum yield was determined to be 32.8% which is much higher than that under direct excitation at 395 nm for Eu^{3+} (9.8%).

Terbium oxide

Trivalent terbium (Tb^{3+}) is one of the most studied RE ions owing to its green emission. It exhibits narrow emission lines in the UV and Visible spectral region at 384, 416 and 438 nm due to $^5\text{D}_3 \rightarrow ^7\text{F}_j$ ($J = 6,5,4$) transitions and at 493, 543, 584, 620, 700 nm due to $^5\text{D}_4 \rightarrow ^7\text{F}_j$ ($J = 6,5,4,3,2$) respectively (Figure 1.16).

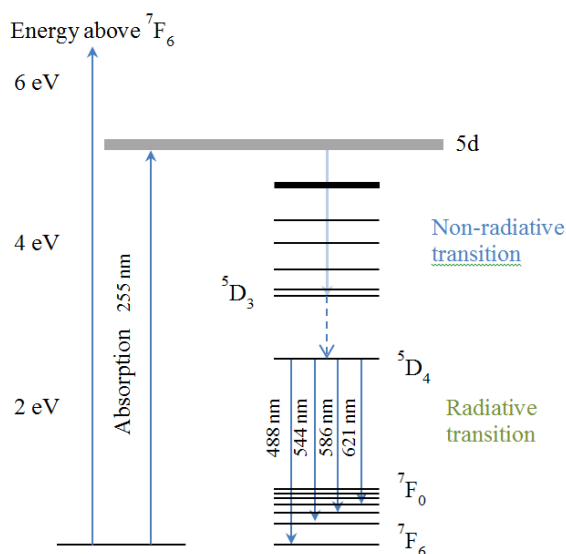


Figure 1.16 Energy level diagram of Tb_2O_3 system.

Tb³⁺ is frequently used as a dopant and incorporated into a host. The energy transfer from the host to RE ions significantly modified the optical properties leading to various promising applications in catalyst, luminescence devices, medical diagnostics etc. The most thoroughly investigated systems involve Tb³⁺ doped semiconductors (e.g., ZnO,¹⁵⁶⁻¹⁵⁸ ZrO₂,¹⁵⁹ TiO₂,¹⁶⁰), phosphates,¹⁶¹⁻¹⁶³ vanadates,¹⁶⁴ fluorides^{150, 165-167}, other, and other RE oxides (e.g., Y₂O₃,¹⁶⁸⁻¹⁷⁰ Gd₂O₃¹⁷¹). Among which ZnO nanostructures doped with Tb³⁺ are particularly attractive since the optical properties of the material can be strongly modified by the doping processes.¹⁷²⁻¹⁷⁴ Various wet chemical routes (e.g., combustion, sol gel, high-temperature thermolysis, chemical precipitation)^{156, 157, 172, 174} have been used to prepare Tb³⁺ doped ZnO nanostructures. Ji et al. developed a two-step method to synthesized isocrystalline core-shell nanocrystals of ZnO:Tb³⁺@ZnO. The nanocrystals demonstrated effective doping and good crystallinity and efficient energy transfer from host material (ZnO) to guest ions (Tb³⁺) was observed. Isocrystalline nanocrystals with effective doping of RE ions in the interior and excellent optical properties make them ideal candidates in the application of light emitting devices. Besides semiconductor ZnO, CaF₂ is a well-known host for luminescent ions due to its high transparency in a broad wavelength range, low refractive index and low phonon energy. Recently, Song et al. demonstrated the efficient sensitization of Tb³⁺ in oleic acid-modified CaF₂:Tb³⁺ nanoparticles through surfactant coating.¹⁶⁵ Another host material, Y₂O₃ has been widely investigated as the host for RE ions for optical application. It has a broad transparency range (0.2-8 μm) with a band gap of 5.6 eV, a high refractive index, better thermal conductivity, and low photon energy that make it an attractive choice as the host material.¹⁷⁵ Sotiriou et al reported the synthesis of Tb-doped Y₂O₃ nanophosphors by flame spray synthesis and dry-coated in situ by thin silica films.¹⁶⁸ The role of SiO₂ coating prevented the monoclinic core particle growth and phase transformation until 850 °C, while their crystallinity was improved by annealing that increased their phosphorescence. This process facilitates the synthesis of bright green nanophosphors with a biocompatible coating suitable for display and bioimaging applications.

1.5 Biomedical applications

The development of metal, metal oxide and bimetallic functional nanostructures has progressed tremendously over the past two decades. These nanostructures are

attracting considerable interest as viable biomedical materials, and research in nanotechnology. The following discussions focus on diverse range of available nanostructures as a promising platform for a wide variety of bioapplications such as antibacterial activity, targeted drug delivery, bioimaging, SERS, fluorescence-based sensing, and electrochemical sensing.

Antibacterial activity

Bacteria are among the most diverse living organisms and capable to adapt to a great variety of ecological environments. Bacterial adhesion to material surfaces is the initial step in colonization and biofilm formation, which is a significant problem to both healthcare and industrial processes. Numerous efforts have been devoted to the development of antibacterial materials using different synthesis strategies. The oldest strategy for antibacterial surface design, focuses on leaching biocides (i.e., cytotoxic compounds from a surface) and inducing the death of both the adhered bacteria and nearby bacteria.¹⁷⁶ However, there is a growing concern that the overuse of biocides can result in higher bacterial resistance and the cross resistance to clinically important antibiotics.¹⁷⁷ It has thus been suggested that biocides should be much more prudently used. Antibacterial metals (e.g., Ag and Cu) are also used as a type of antibacterial agent.^{178, 179} Recent advances in the design and study of these metallic nanostructures have revealed their biological activity, structural and functional changes induced in bacterial cells.^{18, 178-182} Particular progress has been made in understanding the size, shape and surface chemistry of these metal nanostructures and their influence on the biocidal activity. The aim of these nanostructures is attach and anchor the surface of the bacterial cell wall, which involve a large number of electrostatic forces and molecular interactions,¹⁸³ and cause structural, morphological changes and damage, even cell death.¹⁸⁴

Silver has been known to exhibit strong toxicity to a wide range of microorganisms among all other metals. The antimicrobial activity of colloid silver particles are influenced by the dimensions of the particles which the smaller particles impart greater antimicrobial activity than bigger particles due to their larger surface to volume ratios. Panacek et al. reported a one-step protocol for synthesis of silver colloid nanoparticles. The pH and type of reducing saccharide of the reaction system were found to influence the size of particles. A wide range of particle size, particularly 25-100 nm with narrow

size distributions were obtained using four different saccharides. High antimicrobial and bactericidal activity of silver nanoparticles on Gram-positive and Gram-negative bacteria including multiresistant strains such as methicillin resistant *S. aureus* were demonstrated which reveals that the nanoparticles of size 25 nm possessed highest antibacterial activity.¹⁷⁸ In contrast to Ag, Au shows low or no toxicity to bacteria due to its elemental properties. Nalawade studied the antibacterial activity of Ag and bimetallic Ag/Au nanoparticles against gram-negative and grampositive bacteria.¹⁸⁵ It was found that the bimetallic Ag/Au nanoparticles synthesized in the presence of glycerol, triethylamine and sodium dodecylsulfate exhibited enhanced antibacterial activity with equal concentration of silver.

Size-dependent interaction of metal nanostructures with bacteria has been widely reported, however reports on the shape dependence of the antibacterial activity of metal nanostructures are limited. Pal et al. reported that truncated triangular silver nanoplates exhibited the strongest antibacterial activity against *E. coli*, when compared with spherical and rodshaped nanoparticles and also with silver ions.¹⁸¹ Li et. al. reported silver nanodendrites which possess highly effective antimicrobial activities for *E. coli*, *Candida albicans* and *S. aureus*, which are over 10 times that of silver nanoparticles. These investigations suggest that the antimicrobial efficiency of silver nanoparticles depends on their shape and size, particularly silver nanostructures with highly active surfaces can make the most of silver nanostructures' function as multiple antibiotics.¹⁸⁶

Considering the high cost associated with Ag-based materials, Cu and CuO nanoparticles offer a more economical solution.^{182, 187} Shankar et al. reported the effect of Cu salts (copper acetate, copper chloride and copper sulfate) and reducing agents (NaOH and ascorbic acid) on the size, shape and antimicrobial activity of copper nanostructures.¹⁸⁷ The Cu synthesized by NaOH as reducing agent was fibrous in shape which the length and width of nanostructures are dependent on the type of Cu salts as starting material. On the contrary, when ascorbic acid was used as a reducing agent, nanorod, nanotriangular and spherical nanoparticles were obtained depending on the starting materials. The Cu nanostructures exhibited strong antimicrobial activity against both Gram-positive (*Listeria monocytogenes*) and Gram-negative (*E. coli*) food-borne pathogens. The result also shows that the fibrous in shaped Cu nanostructures prepared by reducing with NaOH, in general, exhibited stronger

antimicrobial activity against both, Gram-positive and Gram-negative bacteria than those prepared with ascorbic acid.

Recently, the use of photocatalytic material such as TiO₂ in antibacterial application has attracted much interest.¹⁸⁸ Under the UV or visible light irradiation, TiO₂-based materials produce a strong oxidative effect (i.e., hydroxyl radical, hydrogen peroxide and superoxide) to kill bacteria. This method has been successful in killing *E. coli* cells and some other types of bacteria. In addition, TiO₂-based materials can be used as a photocatalytic disinfectant without the need of electrical power or chemical reagents.¹⁸⁸ Fujishima et al. first reported the photocatalytic bactericidal effect of TiO₂ thin films with *E. coli* suspension.¹⁸⁹ Under the irradiation with a 15 W black light for 1 hour, no survival *E. coli* cell was found. In the absence of TiO₂, UV light only caused 50% sterilization within 4 hours. This indicated that the efficient bactericidal effect can be attributed to the photocatalytic reaction of the TiO₂ film, which can be observed even when the cells were separated from the TiO₂ surface with a porous membrane. However, TiO₂ is mainly active in UVA light and thus in order to exploit the visible-light region and achieve dark sensitive antibacterial effect, recently Hashimoto et al. reported the grafting of nanometer-sized Cu_xO clusters (Cu⁺ and Cu²⁺ species) onto TiO₂ as hybrid nanocomposites for risk-reduction material in indoor environments.¹⁹⁰ It was found that Cu²⁺ species endow TiO₂ with efficient visible-light photocatalysis, whereas the Cu⁺ species impart antipathogenic properties under dark conditions. By controlling the balance between Cu⁺ and Cu²⁺ in Cu_xO, efficient decomposition and antipathogenic activity were achieved in the hybrid Cu_xO/TiO₂ nanocomposites. Further, the Cu_xO/TiO₂ nanocomposites are very stable under long-term light irradiation and display multifunctional properties, which make them promising materials for a wide range of applications, including air purification in private housing and public places.

Targeted drug delivery

In traditional drug administration routes (i.e., oral ingestion or intravascular injection), the medication is distributed throughout the body through systemic blood circulation. By these routes of drug administration, the drug is unable to be directed to their desired site of action. Targeted drug delivery, sometimes called smart drug delivery,¹⁹¹ is a method of delivering medication to a patient in a manner that seeks to concentrate

the medication in the tissues of interest while reducing the relative concentration of the medication in the remaining tissues and crossing the biological barriers by active accumulation or an active targeting strategy.¹¹³ The advantages to the targeted release system is the reduction in the frequency of the dosages taken by the patient, having a more uniform effect of the drug, reduction of drug side-effects, and reduced fluctuation in circulating drug levels.

The magnetic nanoparticles have been actively investigated as the next generation of targeted drug delivery for more than thirty years.¹⁹² The magnetic nanoparticles can be directed by means of a magnetic field gradient towards the vicinity of the targeted location. When magnetic nanoparticles are conjugated with tumor-targeting ligands (e.g., monoclonal antibodies, peptides, or small molecules), biodegradable magnetic nanoparticles have many advantages in targeted delivery of therapeutic and imaging agents.¹⁹³ Magnetic nanoparticles based drug targeting (Figure 1.17) is a promising cancer treatment method for avoiding the side effects of conventional chemotherapy by reducing the systemic distribution of drugs and lowering the doses of cytotoxic compounds.¹⁹⁴

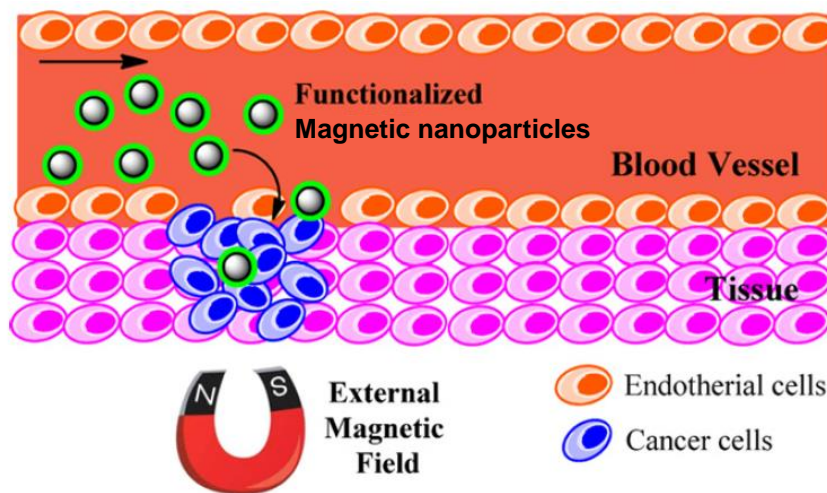


Figure 1.17 Schematic illustrating magnetic nanoparticle-based drug delivery system: these magnetic carriers concentrate at the targeted site using an external high-gradient magnetic field. After accumulation of the magnetic carrier at the target tumor site *in vivo*, drugs are released from the magnetic carrier and effectively taken up by the tumor cells.¹¹³

Generally, magnetic nanoparticles are used as the core and biocompatible components act as a functionalized shell to form the core-shell structure for targeted drug delivery carriers, they can be used to treat tumors in three different ways: (i) specific antibodies can be conjugated to the nanoparticles to selectively bind to related receptors and

inhibit tumor growth; (ii) targeted nanoparticles can be used for hyperthermia (also called thermal therapy or thermotherapy) for tumor therapy; and (iii) drugs can be loaded onto the nanoparticles for targeted therapy. The targeted delivery of anti-tumor agents adsorbed on the surface of magnetic nanoparticles is a promising alternative to conventional chemotherapy. The particles, loaded with the drug, are concentrated at the target site with the aid of an external magnet. The drugs are then released on the desired area.

In a drug carrier system, the effective use of magnetic nanoparticles depends on a number of factors related to the size and magnetism of the biocompatible nanoparticles. Increasing the magnetization is advantageous to facilitate manipulation in drug delivery schemes. The nanoparticles must be small so that they can be superparamagnetic in order to avoid agglomeration after stopping magnetic field and to remain in circulation without being removed by the body's natural filters such as the liver or the immune system. Therefore, nanoparticles with a diameter ranging from 10 to 100 nm are optimal for intravenous injection and have the most prolonged blood circulation times.¹¹³ Colloidal iron oxide nanoparticles have been the most extensively investigated magnetic nanoparticles for biomedical applications due to their excellent biocompatibility and ease of synthesis. Typically composed of nanocrystalline magnetite (Fe_3O_4) or maghemite ($\gamma\text{-Fe}_2\text{O}_3$) which were coated or functionalised with biocompatible organic polymers (e.g., poly(ethylene glycol), chitosan, dextran, etc), liposomes, silica, and bioceramics^{111, 195} to further boost the potential use in medicine. These multifunctional Fe oxide nanoparticles not only serve as a vehicle for targeted drug delivery but also have applications in magnetic resonance imaging,¹⁹⁶ targeted thermosensitive chemotherapy,¹⁹⁷ and fluorescent/luminescence imaging.¹⁹⁸ For example, Kakki et al. reported biocompatible nanosystems, which are useful for cancer therapeutics and diagnostics.¹⁹⁹ These systems are the superparamagnetic Fe oxide nanoparticles carrying the anticancer drug doxorubicin and coated with the covalently bonded biocompatible polymer poly(ethylene glycol), native and modified with the biological cancer targeting ligand folic acid. These multifunctional nanoparticles are designed to rationally combine multilevel mechanisms of cancer cell targeting (magnetic and biological), bimodal cancer cell imaging (magnetic resonance imaging and fluorescence), and bimodal cancer treatment (targeted drug delivery and hyperthermia effect). It was demonstrated that the anticancer drug doxorubicin is

attached to the Fe oxide surface and buried under the polymer layers, while folic acid is located on the extreme surface of the organic coating. Interestingly, the moderate presence of folic acid on the particle surface does not increase the particle surface potential, while it is sufficient to increase the particle uptake by MCF-7 cancer cells.¹⁹⁹

Bimetallic or metal alloy nanoparticles also exhibit superparamagnetic properties which make them attractive candidates as magnetic resonance imaging contrast agents or magnetic carriers for drug delivery. Recent advances in the synthesis and surface modification of FePt nanoparticles have made these magnetic nanoparticles a viable option for biomedical applications.²⁰⁰ Interactions between the transition metal and noble metal lead to greater chemical stability in comparison to other high moment metallic nanoparticles. Furthermore, the surface chemistry of these nanoparticles allows for binding of carboxylate- and amine-based surfactants which may be utilized to improve the water solubility of these nanoparticles. Gao et al. developed FePt nanoparticles encapsulated with a shell composed of CoS₂ to serve as multifunctional nanostructures with cytotoxicity toward cancer cells while the shell composed of CdO offer fluorescence detection (quantum yields of 2.3-9.7%).^{201, 202}

Bioimaging

Bioimaging plays a crucial role in medical diagnostic field, which offers a unique approach for visualizing morphological details in tissue and thus has become a powerful noninvasive tool for visualizing the full range of bio-species from living cells to animals.^{203, 204} It is an important tool for fast diagnosis of diseases at an early stage which is essential for successful treatment. In optical bioimaging, fluorescent proteins or organic dyes are the most common markers. Yet, these conventional fluorescent markers suffer from color fading restricting their temporal use, autofluorescence of the biological tissue leading to background emission overlaying the emission of interest from the marker, thus resulting in reduced image contrast, and phototoxicity. Much effort has been made to overcome these limitations. Bioimaging (i.e., downshifting) based on Ln-incorporated nanoprobe exhibits many prominent optical features such as high quantum yield, narrow bandwidth, long-lived emission, and large apparent Stokes shifts. So far, most studies of the downshifting luminescence-related bioimaging are based on Eu³⁺, Tb³⁺, and Dy³⁺ that can produce strong and practically useful luminescence.²⁰³ Ln³⁺-doped inorganic nanoparticles have been under intensive

investigation and proposed as an ideal candidate for optical imaging, because the rigid crystal host matrices not only provide a steady microenvironment for the lanthanide emitters but also reduce the risk of toxic ion leaching *in vivo*.

Setua et al. developed a bio-nanoprobe based on monodisperse RE oxide, Eu^{3+} and Gd^{3+} doped Y_2O_3 nanoparticles which exhibit both paramagnetism that enable magnetic resonance imaging of cancer cells, target specifically to their molecular receptors.²⁰⁵ Briefly, Y_2O_3 nanocrystals of average size ~ 20 nm were doped with Eu^{3+} for bright red (612 nm) fluorescence. Co-doping with Gd^{3+} resulted in a transition from diamagnetic to paramagnetic functionality suitable for T1-weighted magnetic resonance imaging as well as enhances quantum efficiency. The targeted cancer imaging using Y_2O_3 was demonstrated by conjugating with a potential cancer targeting ligand, folic acid, which detect folate receptor expressing cancer cells. Cytotoxicity studies and reactive oxygen stress analysis showed that these nanocrystals neither hamper the cellular viability nor cause any oxidative stress. As a typical red emission material, Eu^{3+} is incorporated in YVO_4 as versatile luminescent bioprobes. Shen et al. synthesized $\text{YVO}_4:\text{Eu}^{3+}$ nanoparticles via phosphinopolyacrylic acid-mediated hydrothermal reaction.¹⁴⁹ The biocompatible nanoparticles are employed in cell imaging studies, which the nanoparticle-labeled mouse macrophage cell were detected by both laser confocal microscopy and microscopic spectral mapping.

Zhang et al. demonstrated a template-mediated protocol for the large-scale preparation of high-aspect-ratio, single-crystalline Tb^{3+} CePO_4 nanowires, measuring ~ 12 nm in diameter and over $10 \mu\text{m}$ in length.²⁰⁶ The resulting nanowires demonstrated an intense redox-sensitive green photoluminescence, which was exploited, in addition to their inherently high biocompatibility and low toxicity, for potential applications in biological imaging and labeling of cells. Sotiriou et al. generated Tb^{3+} activated Y_2O_3 nanophosphors encapsulated in situ by a thin amorphous inert SiO_2 film.²⁰⁷ The nanocrystalline core exhibits a bright green luminescence following the Tb^{3+} ion transitions, while the hermetic SiO_2 -coating prevents any unspecific interference with cellular activities. The SiO_2 -coated nanophosphors display minimal photobleaching upon imaging and can be easily functionalized through surface absorption of biological molecules. The nanophosphors are particularly attractive for cell detection and for long-term monitoring of cellular activities due to the minimal photobleaching. Using this protocol, interaction between epidermal growth factor-functionalized

nanophosphors and mouse melanoma cells was studied. Recently, Liu et al. developed an inorganic oxide bioprobe based on tetragonal $\text{ZrO}_2:\text{Tb}^{3+}$ nanoparticles of sub-5.0 nm were synthesized via solvothermal method.¹⁴⁸ After bioconjugation with amino-terminal fragment of urokinase plasminogen activator, the oxide nanoparticles exhibited specific recognition of cancer cells overexpressed with urokinase plasminogen activator receptor (an important marker of tumor biology and metastasis). Intense Tb^{3+} green signal was observed from nanoparticles bound to the membrane of cancer cells (H1299) upon 488-nm laser excitation.

1.6 Bioanalytical applications

SERS sensing

Surface-enhanced Raman scattering (SERS) is a powerful analytical tool for determining chemical information for molecules on metallic substrates on the 10-200 nm size scale.⁵⁷ Raman vibrations of molecules are in general very weak; but in the presence of metals (i.e., Cu, Ag, and Au) with nanoscale roughness, the molecular Raman vibrations excited by visible light are enhanced by orders of magnitude. Particularly, the anisotropic metallic nanoparticles possess all characteristics that make them excellent candidates as SERS substrates.²⁰⁸ Plasmon absorption bands can be tuned with nanocrystal aspect ratio to be in resonance with common visible laser sources, optimizing the electromagnetic enhancement mechanism. Moreover, anisotropic nanocrystals have highly curved, sharp surface features with dimensions less than ~100 nm. This can increase the local electric field up to 100-fold at the tip.⁵⁷

Guo et al. reported the correlation of shape of Au nanorods prepared by seed-mediated technique to SPR and SERS (Figure 1.18).²⁰⁹ A series of Au nanorods with various aspect ratios was prepared and found that increasing the aspect ratio finely tunes the position of the longitudinal plasmon mode of the nanorods in a wide spectral range. As it is easy to shift the longitudinal SPR of Au nanorods to the spectral range of 650-900 nm, a “clear” window for in vivo optical imaging and sensing that separates the major absorption peaks of blood and water, these findings may serve as the basis for developing near-infrared SERS nanoprobe for bioanalytical applications.

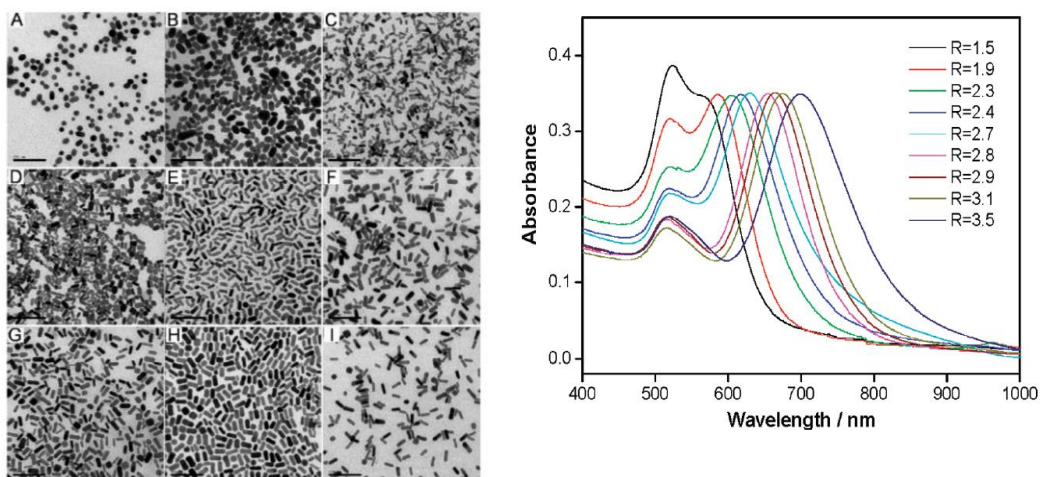


Figure 1.18 TEM images of Au nanorods with varying aspect ratios: (A) 1.5, (B) 1.9, (C) 2.3, (D) 2.4, (E) 2.7, (F) 2.8, (G) 2.9, (H) 3.1, (I) 3.5 and the corresponding UV-vis spectra of Au nanorods.²⁰⁹

Rodríguez-Lorenzo et al. described the performance of Au nanostars synthesized in PVP and N,N-dimethylformamide for SERS detection.²¹⁰ It was compared that the spherical nanoparticles present a surface plasmon band centered at 527 nm, while star-shaped colloids of comparable size present a strongly red-shifted surface plasmon resonance, with a maximum absorbance at 730 nm, in the near-infrared region. The SERS enhancement by nanostars was enhanced by several fold when tested on analytes (e.g., Alexa Fluor 750 C5-maleimide and 1-naphthalenethiol), thus demonstrating the potential of nanostars for ultradetection of nonfunctionalized analytes.

As compared to Au and Ag metals, Ru usually shows a weak SERS effect. Yin demonstrated the controlled synthesis of Ru nanostructures with different morphologies and sizes could exhibit enhanced SERS properties due to their distinct morphologies. The SERS signals of these Ru nanocrystals with 4-mercaptopyridine as molecular probes showed an enhancement sequence of capped columns > triangle nanoplates > nanospheres, probably due to the sharp corners and edges in the capped columns and nanoplates as well as the shrunk interparticle distance in their assemblies (Figure 1.19).⁶⁸

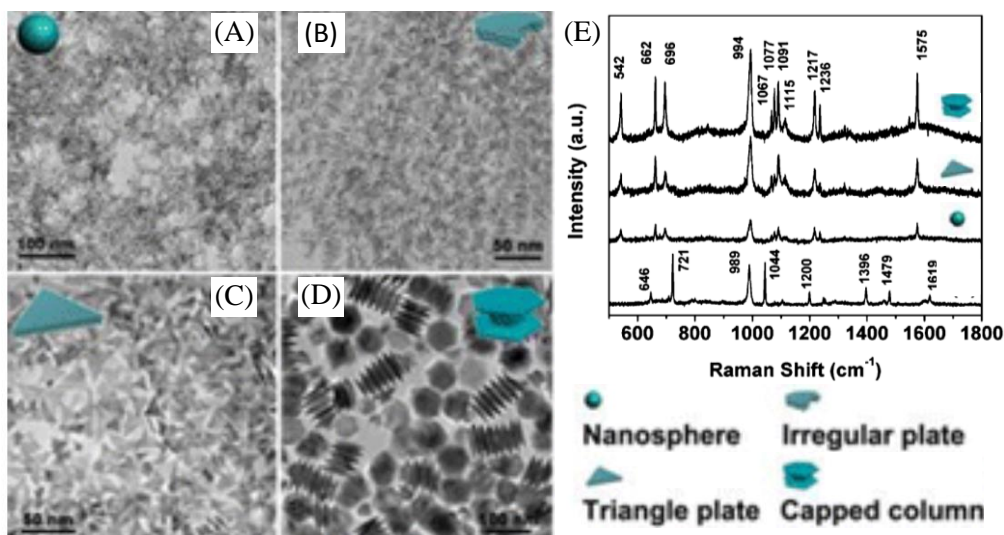


Figure 1.19 TEM images of Ru nanostructures (A) nanospheres, (B) irregular plates, (C) triangle plates, (D) capped columns, and (E) SERS spectra of 4-mercaptopyridine on films of Ru nanostructures: capped columns, triangle plates, nanospheres, and Raman spectra of bulk 4-mercaptopyridine solids.⁶⁸

In recent years, bimetallic nanoparticles have been developed as substrates capable of providing large electromagnetic enhancements for surface enhanced spectroscopy. Cu/Au alloy nanostructures have received considerable attention in application of SERS detection. Jiang et. al. demonstrated a template-based strategy to synthesize high quality Cu/Au alloy nanotubes with five-fold twinned structure by using Cu nanowires as templates.²¹¹ Compared with Au and Ag, Cu has the advantage of reducing cost when used in applications such as catalysis and SERS detection. However, Cu is more susceptible to oxidation upon exposure to air compared with Au and Ag. To overcome this limitation, Cu-based binary alloy nanostructures are used. When the SERS measurement was excited using 638 nm laser, the enhancement of the SERS on Cu/Au alloy nanotubes is at least three times larger than that on the Cu nanowires using 4-mercaptopyridine solution as the probe molecule. It was pointed that a large number of hot spots were produced at the intersection of the two nanotubes for contributing to the SERS enhancement.

Electrochemical sensing

Electrochemical sensing is commonly used for metabolic disorder detection in human body.²¹² A metabolic disorder occurs when the abnormal chemical reactions in the body disrupt metabolism and causes the body to have either too much or too little of the essential substances needed to stay healthy. For example, an excess of uric acid,

oxalic acid and citric acids in the urine is considered a key factor in the development of renal calculi (stones), while elevated levels of creatinine in the serum and urine are recognized as a sensitive and specific index for evaluating the glomerular filtration rate and, in general, for assessing renal, thyroid and muscular functions. Elevated level of H_2O_2 is generated from many fundamental biological oxidative reactions as a by-product or an intermediate product, indicating the existence of an illness. Among these metabolic disorders, diabetes is the most common metabolic disease which is caused by the high level of blood glucose in the body over a prolonged period (further discussed in chapter 2 and 3). Therefore, the study on glucose sensing is of practical significance and the development of an ideal glucose sensor has been the top issue for the biosensor industry. Despite numerous processes and methodologies have been developed for creating new glucose biosensors (i.e., electrochemical methods, colorimetry, conductometry, optical methods, and fluorescent spectroscopy)¹²⁴ electrochemical glucose sensors have attracted the most attention over the last 40 years because of their unbeaten sensitivity and selectivity. Additionally, electrochemical techniques show lower detection limit, faster response time, better long term stability and inexpensiveness.^{124, 213}

Electrochemical sensing which is typically operated in amperometric mode has gained increasing popularity for the monitoring of glucose. It is a sensitive technique in which the signal of interest is current that is linearly dependent on the target concentration by applying a constant bias potential. Glucose is oxidized at the working electrode composed of a metal which is capable of performing redox reaction or biorecognition species such as GOx for glucose sensing. A typical amperometric biosensor comprises three electrodes such as reference, working electrode and auxiliary counter electrode having a large surface area to make most of current flows between the counter and the working electrodes, though voltage is still applied between the working and the reference electrodes. With the aim of producing cost effective and sensitive biosensors, Cu-based nanomaterials have been studied for the synthesis of nanostructures able to introduce new features to glucose detection. During the oxidation of glucose to glucolactone, it is proposed that the catalytic component is Cu(III) oxyhydroxide species, the oxidised partner to the $Cu(OH)_2/CuOOH$ redox couple, thus the catalytic reaction is highly dependent on Cu(II)/Cu(III) redox couple. A further recent progress of copper-based electrochemical glucose biosensor is described in chapter 2 and 3.

Gao et al. reported a nonenzymatic amperometric electrochemical sensor for the detection of H_2O_2 which was fabricated based on highly dense Ag nanowires and chitosan film.²¹⁴ The sensor offers several advantages including high sensitivity, low detection limit, fast response, satisfactory reproducibility, and good long-term stability due to the nanowires and also the architecture stability through the chitosan polymer film. Besides Ag nanostructures, Au nanostructures are widely used in electrochemical sensing arise from their large surface area-to-volume ratio and their interface-dominated properties. They can decrease the overpotentials of many electroanalytical reactions and maintain the reversibility of redox reactions. Kopasova et al. described an enzyme electrode comprised of the ultrathin Au nanowires and their assembly with horseradish peroxidase enzyme for bioelectrochemical sensing of hydrogen peroxide.²¹⁵ The sensors exhibited a lower detection limit, wide working concentration range, higher reproducibility as well as better long-term stability compared to the planar horseradish peroxidase enzyme sensor, thereby improving the sensor response. The improved performance of the Au nanostructures electrodes is attributed to the geometrical signal enhancement due to the higher effective surface area, and as a consequence, a larger amount of the immobilized protein. Plowman et al. reported a nanostructured Au surface consisting of closely packed outwardly growing spikes for the electrochemical detection of dopamine and cytochrome c.²¹⁶ A significant electrocatalytic effect for the electrooxidation of both dopamine and ascorbic acid at the nanostructured electrode was attributed to the presence of surface active sites which allowed the detection of dopamine in the presence of excess ascorbic acid. This nanostructured surface also shows promising behaviour once modified with a monolayer of cysteine for the electrochemical characterisation of cytochrome c and may be a potential surface for the analysis of many more biological processes and in biomolecule sensing.

Fluorescence-based sensing

Fluorescence-based sensing is an optical technique for the detection of low-concentration analytes, owing to its simple, inexpensive and rapid implementation. Target analytes could affect the fluorescent intensity signal of the nanoparticles and thus attracted active field of research for chemicals, drugs and biomolecules sensing.⁵³ Typically, small Au nanoparticles of $< 3\text{nm}$ are used as fluorescence sensing materials

in the visible to near-infrared region.⁵³ The benefits of long lifetime, large Stokes shift, and biocompatibility facilitate Au nanoparticles as a promising sensing systems for various heavy metals analytes (e.g., Hg^{2+} , Cd^{2+} , Pb^{2+} , and Cu^{2+}).⁵³ These heavy metals bind to various cellular components, such as proteins, enzymes, and nucleic acids, leading to alteration of their biological functions, which may cause serious diseases and death. For instance, the sensing mechanism of Hg^{2+} detection is based on the alteration of the electronic structures of Au nanoparticles through the $5d^{10}$ – $5d^{10}$ interaction between Hg^{2+} and Au^+ , as a result, the fluorescence of Au nanoparticles decreases upon increasing the concentration of Hg^{2+} .²¹⁷ Besides the heavy metal cations, Au nanoparticles have been employed for the selective detection of inorganic anions such as CN^- . Liu et al. reported a fluorescent sensor based on Au nanoparticles for CN^- in aqueous solution.⁵⁴ The sensing mechanism is based on the oxidation of Au nanoparticles in the presence of O_2 by CN^- to form stable $[\text{Au}(\text{CN})_2]^-$ complexes, thus resulting in fluorescent quenching. This assay is extremely selective, mainly because of high stability of Au nanoparticles.

The Au sensing systems have been utilized for the detection of small organic biomolecules. Xia demonstrated a Gox-functionalized Au nanoparticles probe for glucose detection.²¹⁸ In the presence of glucose, the fluorescence of the Au nanoparticles quenches due to the oxidation of the Au core to form Au^+ by the enzymatic product of H_2O_2 as well as the aggregation of the nanoparticles. Likewise, Nair demonstrated a sensitive assay using urease-stabilized Au nanoparticles for the detection of urea.²¹⁹ Urea is an important marker for evaluating uremic toxin levels and kidney and hepatocellular functions. Urease catalyzes the conversion of urea into NH_3 and CO_2 , leading to generation of NH_4^+ . The interaction of NH_4^+ with the negative surface charge of the Au nanoparticles caused the aggregation of Au nanoparticles and leading to fluorescence quenching.

In addition to Au, RE oxides nanomaterials are promising luminescent candidate to alleviate the limitation of organic fluorophores, quantum dots, which are toxic, expensive, vulnerable to photobleaching and degradation etc. Their excellent luminescent properties could be used as luminescence indicators for different chemical, drugs, and biological substances based on fluorescence quenching or enhancement. Zobeiri et al. reported the potential application of $\text{Y}_2\text{O}_3:\text{Eu}$ nanoparticles

as fluorescence probes for the determination of pyridoxine.²²⁰ Pyridoxine ($C_8H_{11}NO_3$) is one form of vitamin B₆. It plays an important role in human body by balancing sodium and potassium ions, promoting red blood cell production as well as involving in some metabolic processes. The pyridoxine can be detected through the fluorescence quenching of $Y_2O_3:Eu$ nanoparticles in which the extent of the fluorescent intensity quenching is proportional to the concentration of pyridoxine. The quenching mechanism can be described based on charge transfer from the 2p orbital of oxygen to the LUMO of pyridoxine. So, emission from Eu centers decreased because the charge transfer of Y_2O_3 to the 4f orbitals of Eu ions reduced. The fluorescent probes have good fluorescence intensity and chemical stability and can be used for the sensitive, simple, convenient, rapid and efficient detection of pharmaceutical molecules. Lanthanide-doped inorganic nanoparticles have been extended to the determination of Rhodamine B through FRET system. Di et al. demonstrated an aqueous route to synthesize the $CePO_4:Tb$ nanorods which emits bright green light with a long fluorescence lifetime (~ 3.50 ms) upon UV excitation.²²¹ Upon treatment of $CePO_4:Tb$ with aqueous Rhodamine B, an efficient FRET occurs from the Tb^{3+} to the RhB molecules, giving rise to well resolved and ratiometric emissions of donors and acceptors, respectively.

1.7 Objectives and scopes

The use of metal-based nanostructures in medical diagnosis represents an important discipline in advance medical healthcare. The fast diagnosis of diseases at an early stage is crucial for successful treatment. Herein, this thesis aims to fabricate metal-based nanostructures for bioapplications including chemical sensing, bioimaging and bacterial inhibition. We target to work on metal-based nanostructures which compose of earth abundant transition metals and noble metals, which firstly cost effective and also the benefit of improved bimetallic properties in electrochemical sensing. Similarly, this strategy is also applied to RE-incorporated metal oxides which the crucial role of transition metal oxides is to isolate RE emission centers in the amorphous metal oxides matrices so as to prevent concentrating quenching and a higher doping concentration can be achieved for bioimaging application.

This thesis compose of six chapters which the first chapter covers a brief introduction of metal, bimetallic, metal oxides, RE oxides and their properties. Firstly, a general

synthetic methodology of the metal-based nanostructures will be presented, followed by an overview of the current research in fabrication of metal, bimetallic and metal oxides nanostructures. It follows that the current and potential applications of nanostructures in the biomedical area will be presented. The principles of colloidal fabrication are applied in the following chapters to prepare the desired products with controlled size, shape, composition, crystal structure and surfactant capping for various bioapplications. Chapter 2 introduces the anisotropic growth of Cu nanowires through the disproportionation reaction. The prepared Cu nanowires are developed as electrochemical glucose sensing and the excellent antibacterial properties are exploited for reusable Cu nanowires glucose sensor. Chapter 3 extends the works on Cu nanowires with noble metals, Au. The displacement of Cu by Au in the reaction yields the Cu/Au bimetallic Cu nanotubes which enhanced the sensitivity of glucose sensing attributed to high chemical stability and large surface active sites. Chapter 4 is devoted to the synthesis of amorphous RE-incorporated metal oxides to synthesize highly luminescent $\text{ZrO}_2:\text{Tb}^{3+}$ nanoparticles in pesticides sensing through luminescent quenching. Chapter 5 emphasizes the fabrication of amorphous $\text{ZrO}_2:\text{Tb}^{3+}$ and $\text{TiO}_2:\text{Eu}^{3+}$ nanoparticles, followed by the subsequent polymer encapsulation to render aqueous solution dispersibility. The highly luminescent red emission is employed in cellular biomaging by confocal microscopy. The high photostability and low cytotoxicity of the RE-incorporated metal oxides are potentially the next generation bioprobes in bioapplications. Chapter 6 summarizes the outcomes of the research project and the future works that can be extended from current results.

Chapter 2
Fabrication of Copper Nanowires for
Glucose Sensing

2.1 Introduction

Diabetes mellitus is a group of metabolic diseases causing by the high level of blood glucose in the body over a prolonged period. With more than 220 million of people affected globally, it is a raising concern as the prevalence of the disease increases at an alarming rate, and the number of diabetes patient is expected to double in 20 years.²²² The clinical diagnostic of diabetes requires regular monitoring of blood glucose daily, therefore, it is of significance importance to develop rapid, sensitive and reliable glucose sensor for the growing demand.

The fifty years of glucose sensor progress (Figure. 2.1) was first demonstrated by Clark and Lyons²²³ in 1962 using glucose oxidase (GOx) enzyme. The active component of GOx is flavin adenine dinucleotide (FAD) which is reduced on interaction with glucose, hence producing the redox product of glucolactone. GOx was immobilised over an oxygen electrode and the oxygen consumption by the enzyme-catalyzed reaction was monitored. The further development of the oxygen sensor was conducted by Updike and Hicks²²⁴, but the major limitation of the first generation enzymatic glucose sensors is the strong dependence of oxygen and the presence of electroactive interferences species in the blood. The second generation glucose sensor was introduced in 1980s,^{225, 226} making use of mediators to facilitate electron transfer. However, the soluble nature of most mediators results in short operation time, irreproducible results and potential biotoxicity. Without the use of mediator, the third generation of glucose sensor was introduced which allow direct transfer between the enzyme and the electrode. The significant lower operating potential minimise the electroactive species interferences. However, due to its relatively smaller linear range in comparison to first and second glucose sensors, further development of glucose sensor is highly desirable.

The non-enzymatic glucose sensor using metal-based nanostructures is expected as the promising fourth generation glucose sensor to alleviate the limitation of enzymatic glucose sensor (e.g. complicated immobilization processes, highly sensitive to pH, temperature, humidity and oxygen concentration in the environment). Recent advances in synthesizing various nanostructured materials in glucose oxidation have received much attention due to their unique capabilities to enhance mass transport and sensing performance with high effective surface area.^{27, 212, 227, 228} Particularly, the use of the

noble metal nanostructures (e.g. Au, Pd and Pt) and their bimetallic nanostructures for glucose sensing was widely studied in the past decade (Table 1).

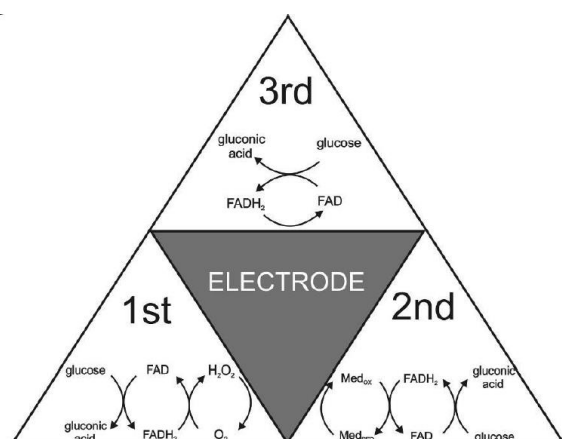


Figure 2.1 Summary of enzymatic glucose oxidation mechanism illustrating first, second and third generation sensors²²⁹

Although exhibiting improved sensitivity towards the oxidation of glucose, the major limitation associated with chemically inert noble metals is the high cost, which makes it less competitive in the practical application. Moreover, noble metals such as Pt have a low tolerance to many species in the physiological conditions, especially chlorides anions. The anions adsorb to the surface strongly and make the electrode surface inaccessible to the analytes.²³⁰ Also, the poisoning by the adsorbed intermediates in the blood such as amino acids, ascorbic acid, uric acid, and creatinine severely reduces the electrocatalytic activity of the Pt electrode.^{222, 231}

Table 2.1 List of noble metals non-enzymatic glucose sensors. The table is presented with respect to electrode materials, sensitivity, linear range, limit of detection and publication year.

Electrode composition	Sensitivity (mA mM ⁻¹ cm ⁻²)	Linear Range (mM)	LOD (μM)	Year	Ref.
Au					
Au macroporous	0.0466	0.005 - 10	3.2	2008	[232]
Au nanowire array	0.309	1-10	50	2009	[233]
Au nanotube array	1.13x10 ⁻⁴	1 - 42.5	10	2009	[234]
Au nanoparticles	not given	0.4 - 10.7	370	2009	[235]
Au particles/MWCNTs ^a	not given	0.2 - 40	50	2014	[236]
Pd					
Pd nanoparticles/SWNTs ^b	1.6x10 ⁻⁴	0.5 - 17	0.2	2009	[237]
Pd nanoparticles/CNTs	0.0114	0 - 46	nil	2010	[238]
Pd nanoparticles/graphene	0.0312	0.001 - 1	0.2	2011	[239]
Pd nanoparticles/graphene	not given	0.01 - 5	1	2011	[240]
Pd nanoparticles/grapheme Oxide	not given	0.2 - 10	nil	2012	[241]

Pt					
Pt nanotube arrays	1×10^{-4}	2 - 14	1	2005	[242]
Pt nanoparticles	0.1377	0.2 - 3.2	5	2007	[243]
Pt nanoporous	0.642	0.1 - 1.5	nil	2008	[244]
Pt 3D dendritic structure	0.0121	1 - 20	1.2	2013	[245]
Pt nanoflower	0.011	1 - 7	nil	2014	[246]
Bimetallic alloys					
PtAu/C nanocomposites	0.0047	0 - 10	2	2010	[247]
PtAu/MWCNTs	0.01071	up to 24.44	10	2010	[248]
Pt/Au macroporous	0.03953	1- 20	25	2011	[249]
PtAu dendritic structure	0.03117	up to 7.5	nil	2013	[250]

List of abbreviations: a- multi-walled carbon nanotubes, b- single-walled carbon nanotubes

In view of cost-effectiveness, transition metals (e.g., Ni and Cu) and their bimetallic nanostructures (e.g., Cu/Ni) are promising in mass production to develop disposable non-enzymatic glucose sensors (Table 2.2).^{28, 222, 231, 251, 252} Ni and Cu electrodes are generally conducted in the alkaline medium for glucose oxidation. Upon immersion of these metal electrodes (Me) in alkaline electrolyte results in the formation of $\text{Me}(\text{OH})_2$, and further undergoes electrooxidation leads to MeOOH species. The catalytic component which is responsible for the glucose oxidation is mainly based on the $\text{Me}(\text{OH})_2/\text{MeOOH}$ redox couple.²⁸ The promising Ni and Cu nanomaterials as glucose sensor have attracted considerable attention in the recent years.^{251,253,254}

Table 2.2 List of transition metals non-enzymatic glucose sensors. The table is presented with respect to electrode materials, sensitivity, linear range, limit of detection and publication year.

Electrode composition	Sensitivity ($\text{mA mM}^{-1} \text{cm}^{-2}$)	Linear Range (mM)	LOD (μM)	Year	Ref.
Ni					
Ni powder	4×10^{-8}	5×10^{-4} - 5	0.1	2005	[255]
Ni nanoflakes	7.32	0.05 - 0.6	1.2	2008	[256]
Ni nanowire arrays	1.043	0.0005-7	0.1	2009	[253]
Ni/CNT	0.0672	up to 17.5	0.89	2012	[257]
Ni nanoparticles	0.1038	0.0001 - 0.5	0.03	2015	[254]
Cu					
Cu nanoparticles	3.6	0.003 - 10	0.7	2006	[258]
Cu nanobelts	4.433	0.01 - 1.13	10	2009	[259]
Cu nanocubes/MWCNTs ^a	1.096	up to 7.5	1	2010	[260]
Cu polyhedron	not given	0.2 - 4.2	70	2011	[261]

Cu nanowires	0.4203	up to 3	35	2012	[251]
Bimetallic NiCu					
NiCu nanoparticles/MWCNTs	2.633	2.5×10^{-5} - 8	0.025	2013	[262]
NiCu nanoparticles	1.5909	0.01 – 3.2	5	2013	[263]
NiCu nanoparticles	0.01916	0.007 – 23.67	2.3	2014	[252]

List of abbreviations: a- multi-walled carbon nanotubes

In this research, we report a fabrication of non-enzymatic glucose sensors comprise of Cu nanowires which chemically prepared in the organic phase through the controlled disproportionation of Cu^+ in organic solvent and the subsequent disproportionation of the Cu^+ complexes into metallic Cu^0 and bivalent Cu^{2+} at 220 °C. The long nanowires structure is expected to highly promote electron transfer in glucose oxidation resulting in fast response time. The fabrication process is facile and easy to scale-up which are promising in mass production to develop non-enzymatic glucose sensors. In addition, the antibacterial activity of Cu nanowires in thin film was further evaluated to promote the reusable glucose sensors for a more economical health care.

2.2 Experimental section

2.2.1 Materials

Cuprous chloride (99%) and oleylamine (70%) were purchased from Sigma-Aldrich. All the chemicals were used as received without further purification.

2.2.2 Colloidal synthesis of Cu nanowires

Cuprous chloride (3 mmol) was dissolved in oleylamine (10 mL) while temperature was increased to 100 °C under argon flow. After degassing under a reduced pressure for 30 min, the resulting solution was quickly heated to 220 °C under argon protection. After maintaining at 220 °C for 30 minutes to produce colloidal Cu nanowires, the reaction system was allowed to cool to room temperature. The Cu nanowires were separated from the reaction medium by centrifugation. The collected Cu nanowires were purified by three rounds of centrifugation/ re-dispersion in 10 mL of toluene prior to characterization.

2.2.3 Sample preparation for characterization

TEM images were recorded on a Philips CM 300 FEG transmission electron microscope (300 kV). TEM samples were prepared by depositing a drop of diluted colloidal nanostructures in toluene on copper grids and dried under ambient conditions. SEM images (5 kV) was characterized by a JEOL JSM6700F field-emission scanning electron microscope (FESEM). SEM samples were prepared by depositing a drop of diluted colloidal nanostructures in toluene on glass substrates and dried under ambient conditions. XRD of samples on glass substrates was performed with a Bruker General Area Detector Diffraction System using Cu K α radiation ($\lambda = 1.54 \text{ \AA}$).

2.2.4 Thin film fabrication of Cu nanowires

FTO-coated glass substrates were sequentially cleaned by ultrasonication in acetone and water for 10 minutes each and dried in a nitrogen stream. Uniform thin films of Cu nanowires were prepared by drop casting two times of 50 μL of the as-prepared stock solution in toluene onto FTO substrate with a working area of 1.0 cm^2 . The thin films on FTO substrates were vacuum annealed at 220 $^\circ\text{C}$ for 2 h prior to electrochemical characterization as working electrodes. The average weight loading of each thin film were controlled to be approximately 1.3 mg Cu nanowires on 1- cm^2 surface of FTO substrates (measured by microbalance, Sartorius).

2.2.5 Evaluation of electrocatalytic activities of Cu nanowires

A standard three-electrode configuration system was used with a Pt sheet as counter electrode, an Ag/AgCl electrode as reference electrode, and FTO substrates coated with Cu-based nanostructures as working electrodes. Electrochemical measurements were performed in a deoxygenated sodium hydroxide solution (0.1 M) with a potentiostats (Autolab PGSTAT101) connected to Nova 1.9 software. CV profiles of Cu nanowires were recorded in the potential window from 0 to 0.7 V (vs. Ag/AgCl) under a constant stirring. Electrocatalytic activities of Cu nanowires were evaluated at a potential of 0.6 V (vs. Ag/AgCl) in the absence and presence of glucose with a cumulative concentration up to 10.5 mM. All the experiments were conducted at room temperature (25 $^\circ\text{C}$).

2.2.6 Examination of antibacterial activities

The bacterial strains used in these studies were *S. aureus* ATCC 29213 and *E. coli* ATCC 10536. 1.5 mL of bacteria suspension at a concentration of 2×10^5 CFU/mL (CFU, colony forming unit) was added onto Cu nanowires thin film on glass (1×1 cm) that were placed in 24-well plate followed by culturing at 37 °C. The control is bacterial solution without sample. After 1, 3, 6 and 24 hours of incubation time, the serial 10-fold dilutions of bacterial suspension from each sample were spread on the surface of petri dish covered with LB agar. The agar plates were cultivated for 24 hours in a biological thermostat at 37 °C and then the agar plates with countable numbers of bacterial colonies were counted. The antibacterial efficiency E was determined according to the following formula:

$$E (\%) = (A-B)/A \times 100\%$$

Here A is the number of bacterial colonies grown from the control suspension and B is the number of bacteria colonies grown from the suspension which was in contact with the sample.

2.3 Results and discussion

2.3.1 Colloidal synthesis of Cu nanowires

Typically, colorless Cu^+ ions become pale yellow after reacting with oleylamine at 100 °C. When the temperature was increased to ~180 °C, the resulting Cu^+ -oleylamine complex started to disproportionate and formed a reddish brown solution, indicating the formation of copper nanostructures.^{29, 264} With the increase of temperature to 220 °C, the disproportionation reaction was accelerated to rapidly grow copper nanostructures (Figure 2.2A). The SEM image of the as-prepared Cu nanostructures at 220 °C shows the anisotropic growth of uniform nanowires with ~ 50-100 nm (inset) in diameter and > 20 μm in length (Figure 2.2B). The XRD pattern of the Cu nanowires (Figure 2.2C) exhibits three diffraction peaks at 43.5, 50.7 and 74.4°, which are indexed to the (111), (200) and (220) crystal planes of the fcc copper (JCPDS #03-1018), respectively. No peak of impurities was observed, indicating the formation of pure Cu nanowires.

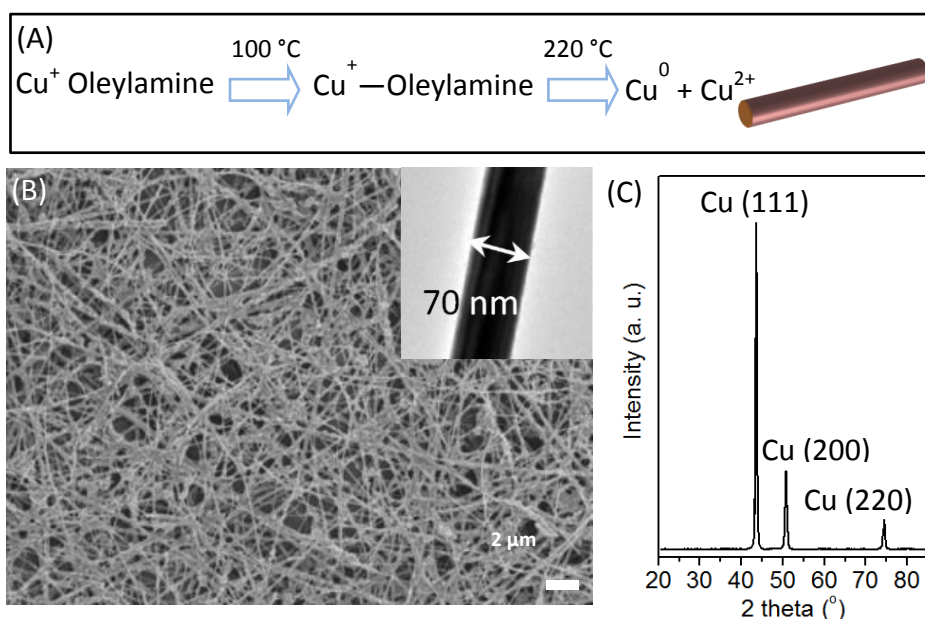


Figure 2.2 Anisotropic growth of Cu nanowires by the controlled disproportionation of CuCl in oleylamine at 220 °C. (A) Schematic disproportionation reaction for the formation of Cu nanowires. (B) Low magnification SEM image of Cu nanowires and the magnified TEM image at inset. (C) XRD pattern of copper nanowires.

2.3.2 Electrocatalytic activities of Cu nanowires towards glucose oxidation

To examine the electrocatalytic oxidation of glucose, Cu nanowires were drop casted on FTO substrates as electrode. Subsequently, the resulting thin film of Cu nanowires on FTO substrate was annealed in vacuum at 220 °C to remove the remained organic molecules and improve the adhesion of the nanostructures on the substrates. After the heat treatment of copper nanowires, the respective XRD pattern still remains the diffraction peaks of metallic copper at 43.5, 50.7 and 74.4°, which are indexed to the (111), (200) and (220) crystal planes of fcc Cu (JCPDS #03-1018), respectively. This resulting Cu nanowires electrode and their blank FTO substrates were tested for their electrocatalytic activities in 0.1 M sodium hydroxide electrolyte at a scan rate of 50 mV s⁻¹.

The blank FTO does not give an obvious signal in the range of 0-0.7 V in the absence or presence of 3.0 mM glucose (Figure 2.3A). In contrast, the CV profile of Cu nanowires as an electrode exhibits redox behaviour (0.2-0.7 V) through Cu²⁺/Cu³⁺ redox couple in the blank alkaline solution (Figure 2.3B).²⁶⁵ With the addition of 3.0 mM glucose, the current density is greatly increased corresponding to the oxidation of glucose, starting at ~0.15 V, indicating Cu nanowires play the role in the glucose oxidation via an intermediate, high valence Cu³⁺.²⁵⁸

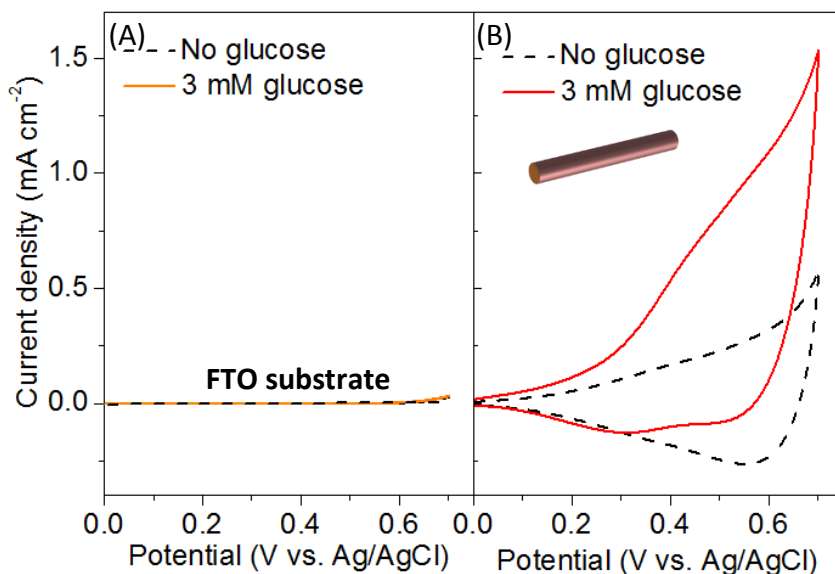


Figure 2.3 CV profiles of (A) blank FTO substrate and (B) Cu nanowires on FTO substrates as electrodes at a potential window of 0-0.7 V and a scan rate of 50 mV s⁻¹ without (---- dash line) and with (— solid line) 3.0 mM of glucose in 0.1 M sodium hydroxide solution.

Figure 2.4 shows the electrochemical responses of FTO and copper nanowires electrodes, which were tested at a fixed potential of 0.6 V by a successive addition of glucose solutions with a cumulative concentration range from 0 to 10.5 mM. Upon the successive addition of glucose, the chronoamperometric profile of FTO exhibits no increment in current density whereas Cu nanowires display a substantial increment in current density, indicating the electrocatalytic activities originated from Cu nanowires. The sensor exhibits a linearity in a concentration range of 0 to 2 mM with sensitivity of 0.34 mA mM⁻¹ cm⁻².

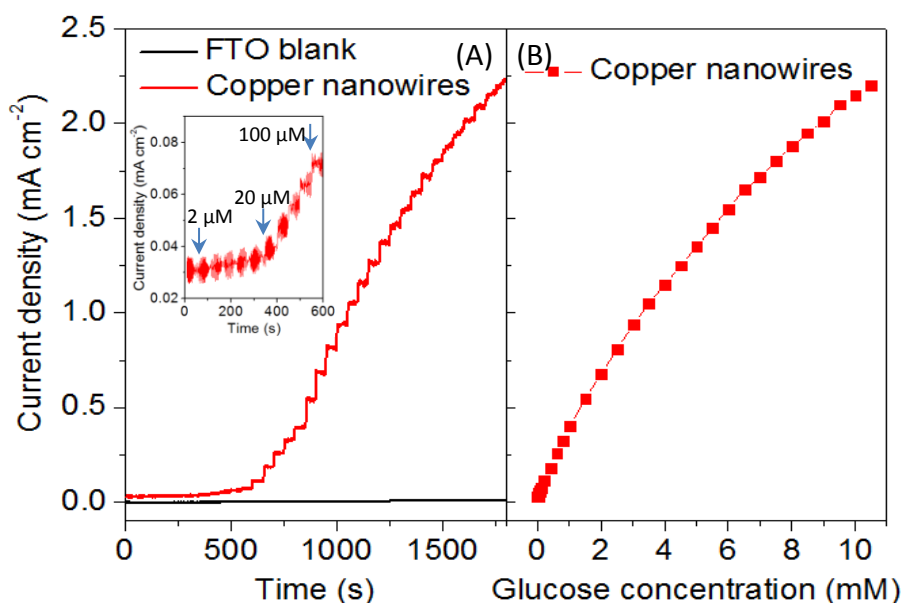
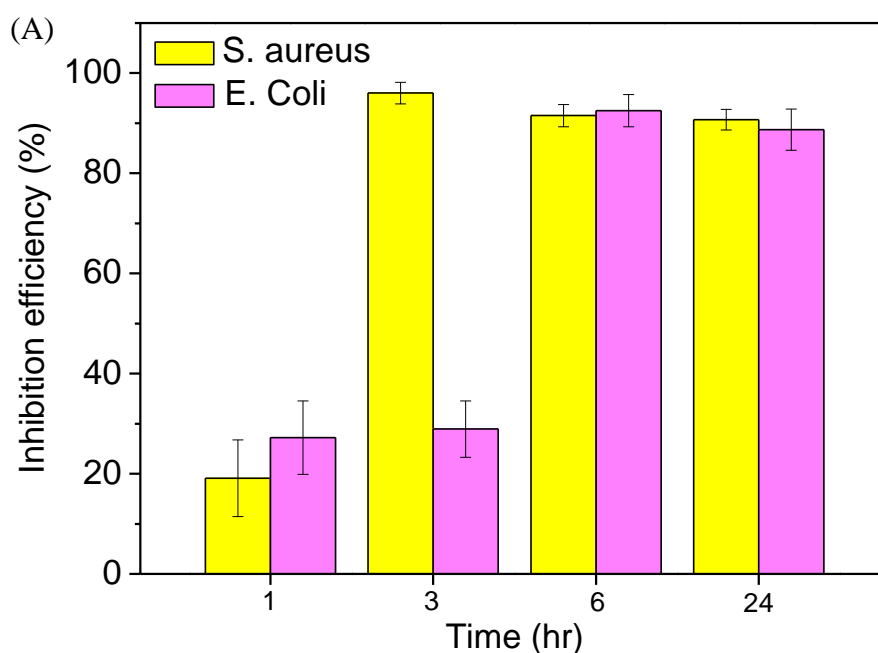


Figure 2.4 Electrocatalytic activities of copper nanowires on FTO substrates as electrodes up to 1800 s. (A) Chronoamperometric curves of copper nanowires at a constant potential of 0.6 V upon a successive addition of a glucose solution to obtain a cumulative concentration from 0 to 10.5 mM. Inset shows the enlarged current density region from 0-600 s. (B) The respective calibration curves of copper nanowires.

2.3.3 Antibacterial activities of Cu nanowires

The antibacterial effect of the Cu nanowires was tested with gram-positive bacteria *S. aureus* and gram-negative bacteria *E. coli*. After 1 hour of contact with *S. aureus*, Cu nanowires inhibited ~ 20% of bacterial cells growth but there are no significant inhibition ($p>0.05$) (Figure 2.5A). After 3 hours and 6 hours, the antibacterial efficiency increased to more than 90%, indicating that the samples can inhibit the bacterial cells growth efficiently ($p<0.05$). After 24 hours, Cu nanowires still maintained over 90% of bacterial inhibition. On the other hand, the antibacterial efficiency of Cu nanowires against *E. coli* is lower than 30% after 1 h and 3 hours of contact time and increased to over 80% after 6 h (Figure 2.5A), indicating that the Cu nanowires have lower antibacterial capability against gram-negative bacteria compared with gram-positive bacteria. After 24 hours, Cu nanowires still maintained over 80% of bacterial inhibition. The typical photos of LB agar plate where *S. aureus* and *E. coli* bacteria in contact with samples and control for 6 hours were cultivated are shown in (Figure 2.5B). The high bacteria inhibition efficiency suggests that the Cu nanowires can be potentially applied as reusable sensing material in glucose sensor.



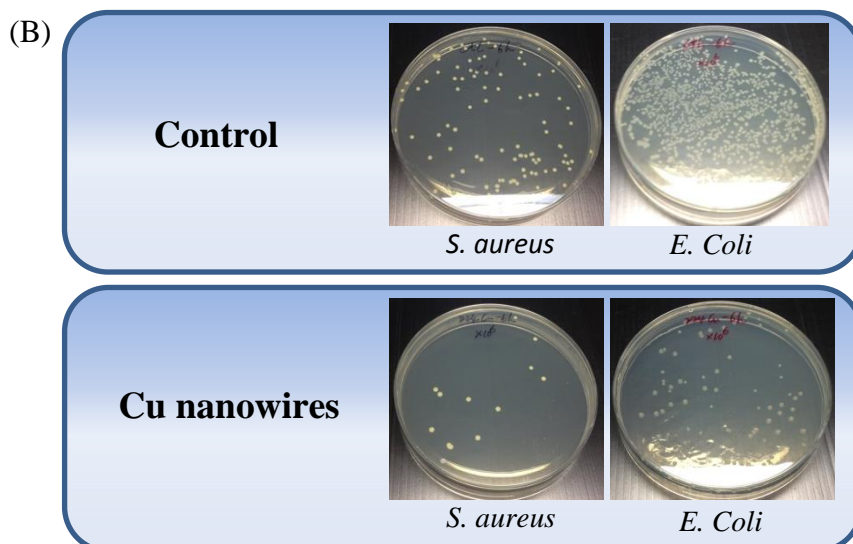


Figure 2.5 Antibacterial activities of Cu nanowires. Antibacterial efficiency of samples against (A) *S. aureus* and (B) *E. coli* bacterial cells as a function of the contact time of 1, 3, 6, 24 hours. The bars indicate the standard errors. (C) Photos of petri dishes with *S. aureus* and *E. coli* bacteria cultivated on LB agar covered with bacterial suspension which was in contact with samples and control for 6 hours.

2.4 Summary

The crystalline anisotropic growth of metallic Cu nanowires were prepared through the controlled disproportionation of Cu^+ complexes into metallic Cu^0 , which involves the initial dissolution of CuCl through coordination with oleylamine in organic solvent and the subsequent disproportionation of the Cu^+ bivalent Cu^{2+} at 220 °C. The Cu nanowires exhibited good sensing capability towards glucose due to the synergistic effect of Cu(II)/Cu(III) redox couple and high aspect ratio of Cu nanowires. Besides, the prepared Cu nanowires were inhibitive towards gram-positive (*S. aureus*) and gram-negative bacteria (*E. coli*). It was demonstrated that Cu nanowires still maintained over 80% of bacterial inhibition after 24 hours, revealing the potential reusability of the Cu nanowires for glucose sensing.

Chapter 3
Bimetallic Cu/Au(Ru) Nanostructures
for Glucose Sensing

3.1 Introduction

To combine the use of the merits of transition and noble metals, Cu and Au are incorporated together to form bimetallic nanostructures for their synergistic effect in glucose sensing. Although there are reports on the use of $\text{Cu}_3\text{Au}_{97}$ ²⁶⁶ and CuAu ²⁶⁷ alloy nanostructures for glucose sensors, there is a great demand to control the amount of noble metal to achieve the excellent electrochemical inertness and biocompatibility while maintaining great cost-effectiveness and glucose sensitivity. As a consequence, the motivation to design a reproducible glucose sensor for a long-term usage is highly desirable. In this research, we report an innovative development of advanced glucose sensors through the optimized synthesis of bimetallic Cu/Au nanotubes (Figure 3.1) by incorporating a very small amount of Au into long and smooth Cu nanowires produced by the controlled disproportionation of Cu^+ . A layer of Au passivates the surface of copper nanowires followed by the formation of chemically stable Cu_3Au alloys at high temperature, which have Cu-rich core and Au-rich surface.⁷⁵ With a large surface area, the bimetallic Cu/Au nanotubes have exhibited their synergistic enhancement in electrocatalytic properties in comparison with Cu nanowires and other shaped Cu/Au nanostructures in terms of lower glucose oxidation onset potential and higher oxidation current response. Also, they have been demonstrated with high sensitivity, low detection limit and fast response towards glucose sensing. The enhanced electrocatalytic performance results from large surface area, increased chemical stability to maintain high conductivity and rapid electron transfer during test. Meanwhile, the bimetallic Cu/Au nanotubes show negligible response to other sugars/ reducing species to demonstrate their very good selectivity in glucose sensing. Without compromising the reproducibility and long-term stability, the present fabrication of highly stable Cu/Au nanotubes enable their reusability as non-enzymatic glucose sensors. Furthermore, with the introduction of a low level of Au at 3, 1 and 0.1 mol% relative to initial Cu precursor, a significant electrocatalytic enhancement has been achieved at 1 mol% as compared to Cu nanowires. In this research, we have developed very stable and low cost Cu/Au nanostructures for sensitive, selective, reproducible and reusable glucose sensing with highly desirable long-term performance through our correlated study of various Cu/Au nanostructures to their electrocatalytic properties.

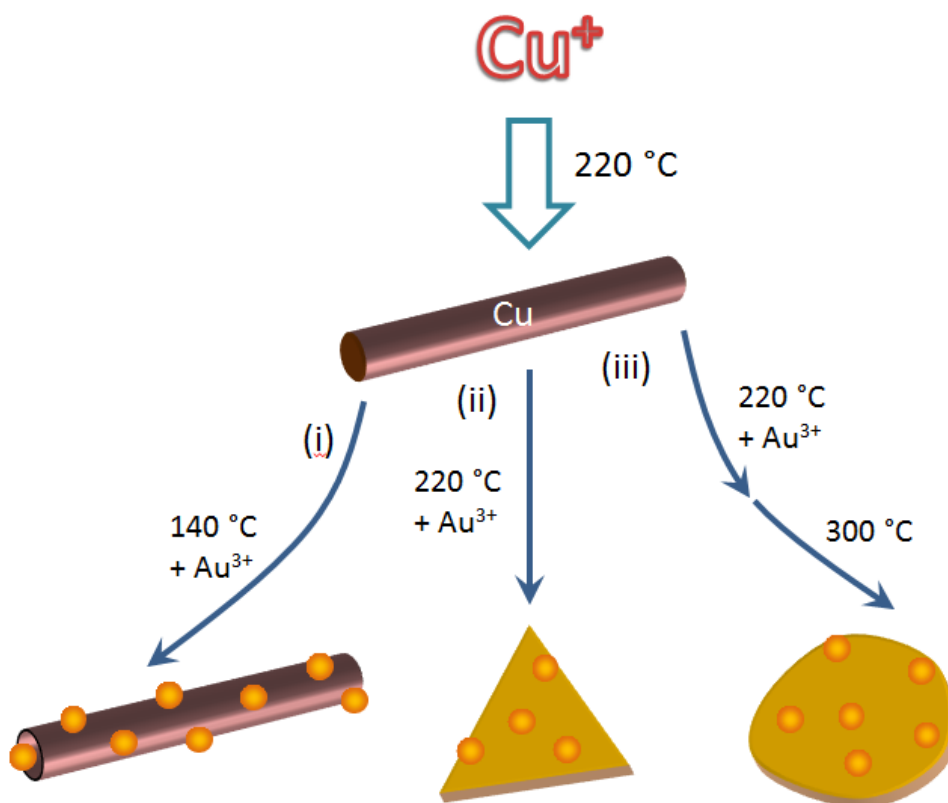


Figure 3.1 Schematic fabrication of bimetallic Cu/Au nanostructures. The reaction temperatures of $220\text{ }^\circ\text{C}$ is anticipated to form Cu nanowires via Cu^+ disproportionation, whereas $140\text{ }^\circ\text{C}$, $220\text{ }^\circ\text{C}$ and $300\text{ }^\circ\text{C}$ are anticipated to form various bimetallic Cu/Au nanostructures as labelled as 220/140, 220/220 and 220/300 °C, respectively.

3.2 Experimental section

3.2.1 Materials

Cuprous chloride (99%), gold (III) bromide (99.9%), Ruthenium (III) chloride hydrate (99.9 %) and oleylamine (70%) were purchased from Sigma-Aldrich. D-(+)-Glucose (99%), lactose (99%), sucrose (99%), maltose (95%), mannose (99%), fructose (99%), uric acid (99%), L-ascorbic acid (99%), acetamidophenol (98%) and dopamine hydrochloride (99%) were purchased from Alfa Aesar. All the chemicals were used as received without further purification.

3.2.2 Colloidal synthesis of Cu/Au (Ru) nanomaterials

3.2.2.1 Bimetallic Cu/Au nanotubes ($220/140\text{ }^\circ\text{C}$)

Cuprous chloride (3 mmol) was dissolved in oleylamine (10 mL) while temperature was increased to $100\text{ }^\circ\text{C}$ under argon flow. After degassing under a reduced pressure for 30 minutes, the resulting solution was quickly heated to $220\text{ }^\circ\text{C}$ under argon

protection. After maintaining at 220 °C for 30 minutes to produce colloidal Cu nanowires, the reaction system was allowed to cool to 140 °C. Then, auric bromide (0.1 mmol) in oleylamine (3 mL) was quickly injected into the reaction mixture and maintained at 140 °C for 20 minutes. The reaction system was then allowed to cool to room temperature and purified by three rounds of centrifugation/ re-dispersion in 10 mL of toluene prior to characterization. Besides the molar ratio of Au/CuCl at 1:30, lower ratios at 1:100 and 1:1000 were also chosen to repeat the above synthetic protocol.

3.2.2.2 Other bimetallic Cu/Au nanostructures (220/220 °C and 220/300 °C)

Cuprous chloride (3 mmol) was dissolved in oleylamine (10 mL) while temperature was increased to 100 °C under argon flow. After degassing under a reduced pressure for 30 minutes, the resulting solution was quickly heated to 220 °C under argon protection. After maintaining at 220 °C for 30 minutes to produce colloidal Cu nanowires, auric bromide (0.1 mmol) in oleylamine (3 mL) was quickly injected into the reaction mixtures and maintained at 220 °C for 20 minutes. In another case, after the formation of Cu nanowires at 220 °C for 30 minutes, auric bromide (0.1 mmol) in oleylamine (3 mL) was quickly injected into the reaction mixtures followed by increasing temperature to 300 °C for 20 minutes. The reaction system were then allowed to cool to room temperature and purified by the same way as above.

3.2.2.3 Bimetallic Cu/Ru nanowires (220/270 °C)

Cuprous chloride (3 mmol) was dissolved in oleylamine (10 mL) while temperature was increased to 100 °C under argon flow. After degassing under a reduced pressure for 30 minutes, the resulting solution was quickly heated to 220 °C under argon protection. After maintaining at 220 °C for 30 minutes to produce colloidal Cu nanowires, the reaction system was allowed to cool to room temperature. The Cu nanowires were separated from the reaction medium by centrifugation. The collected Cu nanowires were purified by three rounds of centrifugation/ re-dispersion in 3 mL of oleylamine. 0.1 mmol of ruthenium chloride was dispersed in 3 mL of oleylamine and added simultaneously with 3 mL Cu nanowires dispersion to 10 mL oleylamine at 270 °C. The reaction system was allowed to cool to room temperature. The reaction system was then allowed to cool to room temperature and purified by the same way as above.

3.2.3 Sample preparation for characterization

TEM images were recorded on a Philips CM 300 FEG transmission electron microscope (300 kV). TEM samples were prepared by depositing a drop of diluted colloidal nanostructures in toluene on copper grids and dried under ambient conditions. EDX mapping and line scan analysis were examined using a JEOL JEM 2100 and JED 2300T (200 kV) transmission electron microscope. Scanning electron microscopy (SEM) images (5 kV) and EDX (15 kV) was characterized by a JEOL JSM6700F FESEM. SEM samples were prepared by depositing a drop of diluted colloidal nanostructures in toluene on glass substrates and dried under ambient conditions. XRD of samples on glass substrates was performed with a Bruker General Area Detector Diffraction System using Cu K α radiation ($\lambda = 1.54 \text{ \AA}$).

3.2.4 Thin film fabrication of bimetallic Cu/Au(Ru) nanostructures

Same preparation procedures applied as section 2.2.4.

3.2.5 Evaluation of electrocatalytic activities of bimetallic Cu/Au(Ru) nanostructures

Same electrochemical set-up as section 2.2.5. CV profiles of Cu-based nanostructures were recorded in the potential window from 0 to 0.7 V (vs. Ag/AgCl) under constant stirring. Electrocatalytic activities of Cu-based nanostructures were evaluated at a potential of 0.6 V (vs. Ag/AgCl) in the absence and presence of glucose with a cumulative concentration up to 10.5 mM. The potential interference of lactose, sucrose, maltose, mannose, fructose, uric acid, ascorbic acid, acetamidophenol and dopamine was studied at a potential of 0.6 V by injecting individuals into the test solution. The stability test was also conducted in 0.1 M sodium hydroxide solution at a potential of 0.6 V. All the experiments were conducted at room temperature (25 °C).

3.3 Results and discussion

3.3.1 Colloidal synthesis of bimetallic Cu/Au nanostructures

The monometallic Cu nanowires can be used as template for the possible fabrication of various bimetallic Cu/Au nanostructures at different temperatures as shown in Figure 3.1. As observed, the reduction of Au³⁺ in oleylamine occurs at a much lower tempera-

ture of ~ 110 °C than that for the disproportionation of CuCl,⁷⁴ and it led to the formation of uniform Au nanoparticles at an elevated temperature of ~ 140 °C (Figure 3.2).

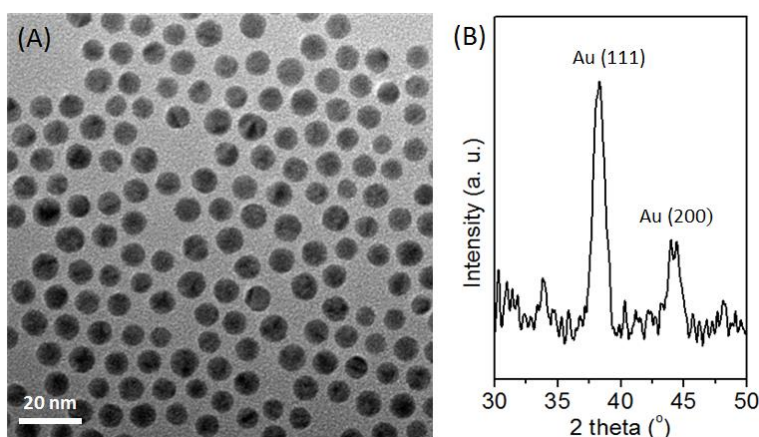


Figure 3.2 (A) TEM image of uniform gold nanoparticles prepared by reacting 0.1 mmol of AuBr₃ in oleylamine at 140 °C for 30 minutes. (B) XRD pattern of the spherical Au nanoparticles with fcc structure (JCPDS #04-0784).

Therefore, the incorporation of Au³⁺ into Cu nanowires was carried out at 140 °C to yield bimetallic Cu/Au nanostructures. Experimentally, Cu nanowires were first prepared at 220 °C (Figure 3.3A-B) and auric bromide in oleylamine was introduced when the temperature cooled to 140 °C. The morphology of nanostructures analysed by SEM is presented in Figure 3.3C. SEM image shows the formation of bimetallic Cu/Au nanostructures with similar dimension to monometallic Cu nanowires. Their coarse surfaces were observed with pits and holes as compared to the smooth Cu nanowires. The respective XRD pattern in Figure 3.3D shows the metallic Cu diffraction peaks at 43.5, 50.7 and 74.4° together with an additional diffraction peak at 38.2°, which is indexed to the (111) of fcc structure of Au (JCPDS #04-0784). A small bump between 40 to 42° is due to the formation of Cu/Au intermediate, indicated by the overlapped distribution of Cu and Au as observed by TEM EDX mapping below. To further investigate the bimetallic Cu/Au nanostructures prepared at 220/140 °C, high magnification TEM images (Figure. 3.4A-B) shows the formation of hollow nanotubes with spherical nanoparticles of ~ 20 nm formed inside the hollow tubes. Tiny pits of 20-50 nm in size were observed on the surface of nanotubes in agreement with the above observation by SEM. Chemical composition of the Cu/Au nanotubes was analysed by TEM EDX mapping and EDX line scan analysis in Figure. 3.4C-F. The even distribution of Cu and Au across the nanostructures exhibits that all the surface of Cu nanowires reacted with Au³⁺ to form a layer of Au. With a higher

electron density of Au than Cu, the darker surface in TEM images indicates the existence of more Au in the region.

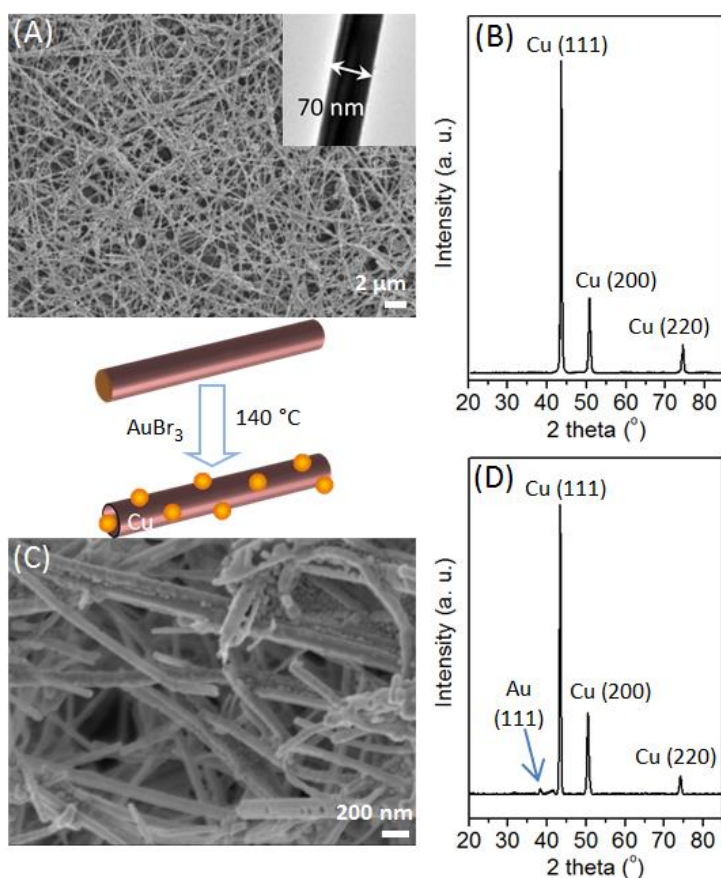


Figure 3.3 Anisotropic growth of Cu nanowires by the controlled disproportionation of CuCl in oleylamine at 220 °C (A-B) for the subsequent formation of Cu/Au nanostructures after reaction with AuBr₃ at 140 °C (C-D). (A) Low magnification SEM image of Cu nanowires and the magnified TEM image at inset. (B) XRD pattern of Cu nanowires. (C) High magnification SEM image. (D) XRD pattern of Cu/Au nanostructures.

The plausible formation mechanism of Cu/Au nanotubes is presented in Figure 3.4G. Firstly, Cu nanowires are formed by controlled disproportionation of CuCl in oleylamine at 220 °C. With a much higher reduction potential of Au³⁺/Au pair than Cu²⁺/Cu pair (1.50 V vs. 0.34 V vs. SHE), copper can be easily oxidised to Cu²⁺ in the presence of Au³⁺.^{96,99} As a sacrificial material, the preformed Cu nanowires can react with Au³⁺ to form a layer of Au at 140 °C as observed by EDX mapping and EDX line scan analysis (Figure 3.4C-F). The high production yield of Cu nanowires at >46% shows that >92% of Cu⁺ is consumed through controlled disproportionation at 220 °C ($2\text{Cu}^+ \rightarrow \text{Cu}^{2+} + \text{Cu}^0$).²⁹ As the disproportionation only takes place at ~180 °C or above, the as-formed Cu nanowires at 220 °C become very stable when the temperature is reduced to a much lower temperature of 140 °C. The reversible disproportionation

($\text{Cu}^{2+} + \text{Cu}^0 \rightarrow 2\text{Cu}^+$) is then negligible to maintain a low level of Cu^+ in reaction solution. A small amount of Au^{3+} is then introduced at 140 °C to oxidize Cu^0 to a higher oxidation state of Cu^{2+} while Au^{3+} is reduced to Au^0 . As the reaction proceeds, the surface passivation initiated randomly on the surface through a pitting effect,³¹ i.e. metal corrosion (anode reaction: $6\text{Cu}^0 \rightarrow 3\text{Cu}^{2+} + 6\text{e}^-$; cathode reaction: $2\text{Au}^{3+} + 6\text{e}^- \rightarrow 6\text{Au}^0$), giving rise to the formation of corrosion pits on the surface of the Cu nanowires. In addition, Au nanoparticles are formed and trapped in the Cu nanotubes as observed by TEM (Fig. 3.4A-B) and confirmed by XRD (Figure 3.2D).

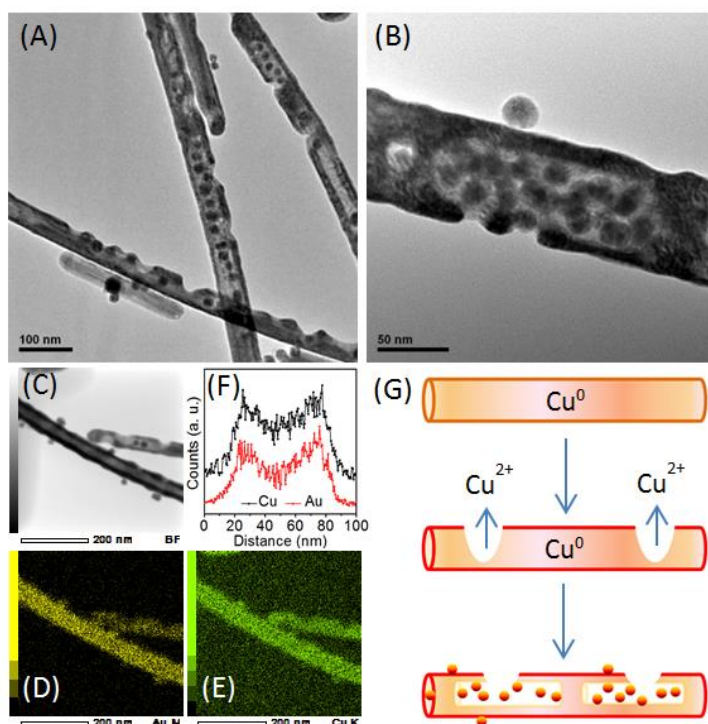


Figure 3.4 (A-B) TEM images, (C-E) TEM EDX mapping of bimetallic Cu/Au nanotubes and (F) line scanning across bimetallic Cu/Au nanotubes. (G) Schematic formation of Cu/Au nanotubes with Au-incorporated nanoparticles.

In comparison, bimetallic Cu/Au nanostructures were further prepared at elevated temperatures of 220 and 300 °C. With introducing a small amount of Au^{3+} at 220 °C into mother solution of the as-prepared copper nanowires, a mixture of nanotriangles and nanorods were obtained while lengthy copper nanowires disappeared. SEM image shows the triangles of 100-150 nm in size and the rods of 50-100 nm in diameter and 1 μm in length (Figure 3.5A). As stated above, at 220 °C, the disproportionation of Cu^+ ($2\text{Cu}^+ \rightarrow \text{Cu}^{2+} + \text{Cu}^0$) is dominant to convert more than 92% of Cu^+ to Cu^{2+} and Cu^0 , indicating the

reversed disproportionation ($\text{Cu}^{2+} + \text{Cu}^0 \rightarrow 2\text{Cu}^+$) does not play a major role at this temperature. In the absence of Au^{3+} , Cu nanowires are stable at 220 °C.

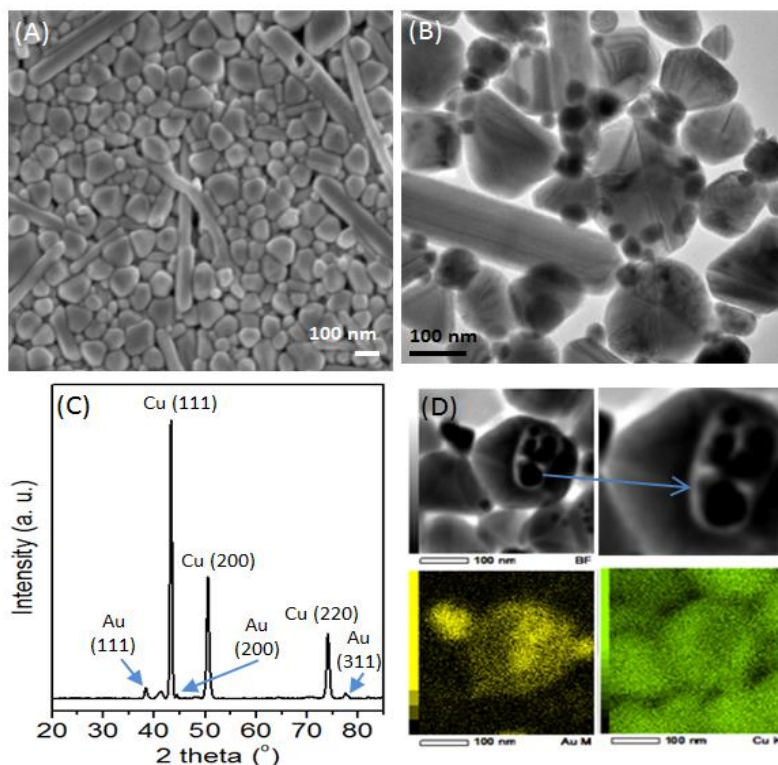


Figure 3.5 (A) SEM image, (B) TEM image, (C) XRD pattern and (D) TEM EDX mapping of Cu/Au nanostructures prepared by heating the as-prepared Cu nanowires at 220 °C after injecting a low amount of Au^{3+} in the solution.

In the presence of Au^{3+} , Cu nanowires become unstable at 220 °C. Through fast oxidation of Cu^0 by Au^{3+} to form Au^0 on the surface of Cu nanostructures, the surface passivation lead to an accelerated corrosion (anode reaction: $6\text{Cu}^0 \rightarrow 3\text{Cu}^{2+} + 6\text{e}^-$; cathode reaction: $2\text{Au}^{3+} + 6\text{e}^- \rightarrow 6\text{Au}^0$) to release Cu^+ and Cu^{2+} . Together with the reversed disproportionation, more Cu^+ ions are produced and further disproportionated to form shape-controlled nanoparticles of up to 150 nm and much smaller nanoparticles of 10-20 nm in size (Figure 3.5B). XRD pattern (Figure 3.5C) of product exhibits three diffraction peaks at 43.5, 50.7 and 74.4° attributed to fcc copper together with three diffraction peaks at 38.2, 44.4 and 77.5°, which are respectively indexed to the (111), (200) and (311) crystal planes of fcc Au (JCPDS #04-0784). A small bump between Au (111) and Cu (111) is due to the formation of Cu/Au intermediate indicated by TEM EDX mapping (Figure 3.5D), which shows the co-existence of both Cu and Au on the surface of shaped nanoparticles or in spherical nanoparticles.

When the reaction temperature was further increased to 300 °C after introducing Au³⁺ at 220 °C, rough nanoparticles of 100-200 nm in size were obtained while no Cu nanowires were remained, as shown in SEM image in Figure 3.6A.

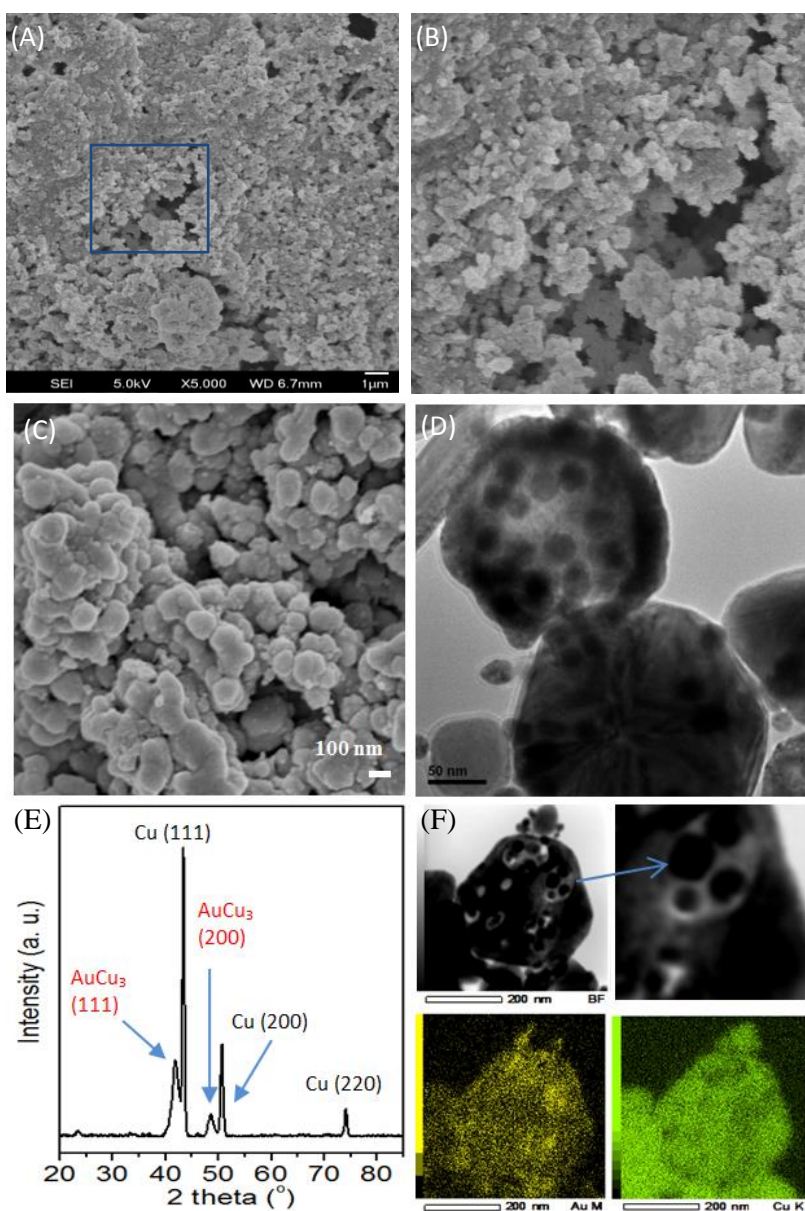


Figure 3.6 (A) SEM image of Cu nanoparticles obtained by disproportionation of CuCl at 220 °C for 30 minutes followed by further heat treatment at 300 °C for 20 minutes. (B) Enlarged region of the blue box in (A). (C) SEM image, (D) high resolution TEM image, (E) XRD pattern, (F) TEM EDX mapping of Cu/Au nanostructures prepared by heating the as-prepared Cu nanowires at 300 °C after injecting a low amount of Au³⁺ at 220 °C.

Similarly, at 300 °C, only rough nanoparticles were also obtained by thermal treatment of Cu nanowires in mother solution prepared at 220 °C in the absence of Au³⁺. The fast dissolution of Cu nanowires is due to the accelerated reversed disproportionation ($\text{Cu}^{2+} + \text{Cu}^0 \rightarrow 2\text{Cu}^+$) at temperature far above 180 °C to

remain rough Cu nanoparticles (Figure 3.6A-B). This is helpful to understand the formation of rough Cu nanoparticles in the presence of Au³⁺. After the surface passivation with Au at 220 °C, the Cu corrosion occurs rapidly upon increasing temperature to 300 °C, leading to the formation of hollow nanoparticles (Figure 3.6D). XRD pattern (Figure 3.6E) also confirms the co-presence of Cu and Cu₃Au in the product. TEM EDX mapping (Figure 3.6F) shows the co-existence of both Cu and Au on the surface of rough nanoparticles of up to 200 nm and in spherical nanoparticles of 10-20 nm in size.

3.3.2 Electrocatalytic activities of bimetallic Cu/Au nanostructures towards glucose oxidation

To examine the electrocatalytic oxidation of glucose, Cu/Au nanotubes were individually drop casted on FTO substrates as electrodes and annealed in vacuum at 220 °C. After the heat treatment, in addition to the three diffraction peaks of metallic Cu, the respective XRD pattern (Figure 3.7A) also shows two more diffraction peaks at 41.7 and 48.5°, which are indexed to the (111) and (200) crystal planes respectively of the cubic Cu₃Au (JCPDS #35-1357). Clearly, there is no XRD peak from fcc Au (JCPDS #04-0784). These show that all the Au on Cu nanostructures was completely converted to Cu₃Au after heating at 220 °C. After the heat treatment of Cu/Au nanostructures prepared at 220 °C, a similar XRD pattern was obtained as well. Besides the three diffraction peaks of metallic copper, two more diffraction peaks at 41.7 and 48.5°, are indexed to the (111) and (200) crystal planes respectively of the cubic Cu₃Au (JCPDS #35-1357)(Figure 3.7B). For the bimetallic Cu/Au nanostructures prepared at 300 °C, the compositions including Cu and Cu₃Au remain unchanged after heating at 220 °C. These resulting copper-based nanostructure electrodes and their blank FTO substrates were tested for their electrocatalytic activities in 0.1 M sodium hydroxide electrolyte at a scan rate of 50 mV s⁻¹.

The CV profile of Cu/Au nanotubes in the absence of glucose (Fig. 3.8B) exhibits a drastic increase in current in the range of 0 to 0.7 V. In the presence of 3.0 mM glucose, the current is further increased to show the greatly increased sensitivity of Cu/Au nanotubes for glucose sensing. Furthermore, the onset of

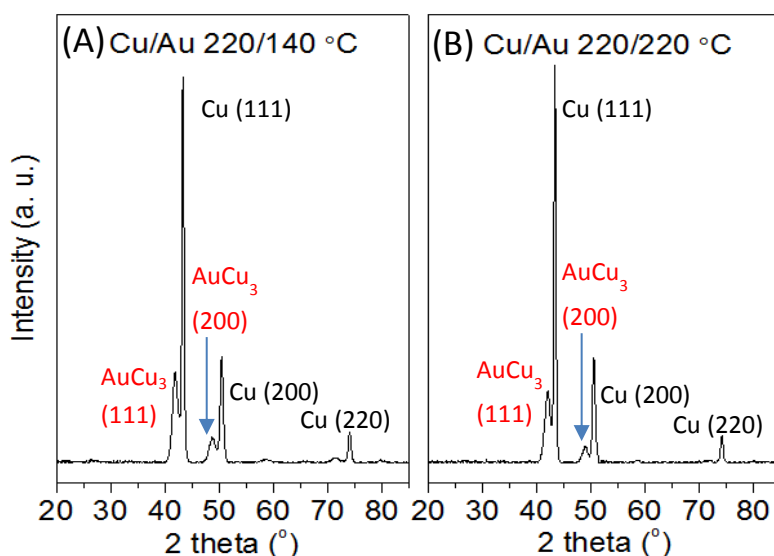


Figure 3.7 XRD pattern of the (A) Cu/Au nanotubes and (B) Cu/Au nanostructures after annealing in vacuum at 220 °C.

glucose oxidation is drastically decreased to ~ 0 V, exhibiting greatly enhanced electrocatalytic activity of Cu/Au nanotubes than Cu nanowires. This shows that the incorporation of Au into Cu nanostructures plays a major role to enhance the glucose oxidation. Similarly, other Cu/Au nanostructures prepared at 220/220 °C and 220/300 °C were tested as well. Their CV profiles in Fig. 3.8C and D also display the improved oxidation response in comparison with copper nanowires, which clearly evidenced the incorporation of Au. Among these Cu/Au nanostructures, the Cu/Au nanotubes show the highest electrocatalytic activity towards glucose oxidation.

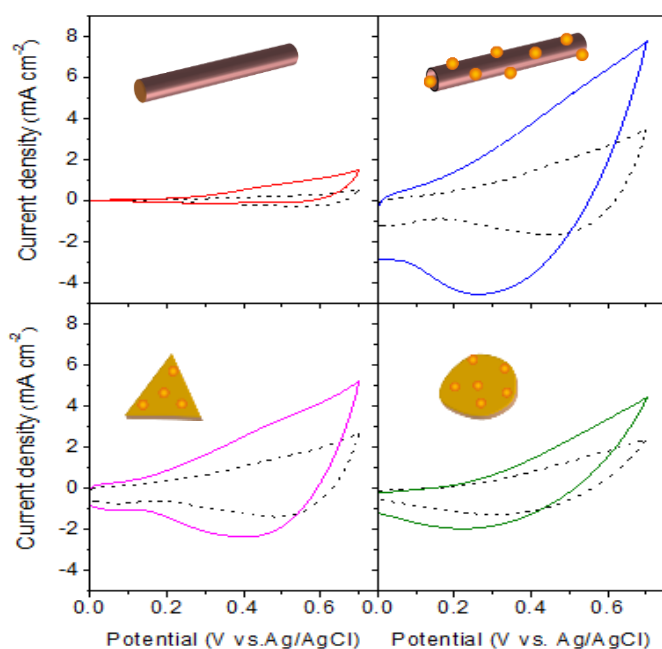


Figure 3.8 CV profiles of Cu nanowires and Cu/Au nanostructures on FTO substrates as electrodes at a potential window of 0-0.7 V and a scan rate of 50 mV s⁻¹ without (---- dash line) and with (— solid line) 3.0 mM of glucose in 0.1 M sodium hydroxide solution. (A) Pristine Cu nanowires (220 °C) and various Cu/Au nanostructures prepared at (B) 220/140 °C, (C) 220/220 °C and (D) 220/300 °C.

Figure 3.9 shows the electrochemical responses of Cu/Au nanostructures as electrodes, which were tested at a fixed potential of 0.6 V by a successive addition of glucose solutions with a cumulative concentration range from 0 to 10.5 mM. The electrochemical responses are compared against FTO and pristine Cu nanowires. Upon the successive addition of glucose, the Cu/Au nanostructures display a substantial increment in current density. The increase of current density follows the order of Cu/Au nanostructures prepared at 220/140 °C > 220/220 °C > 220/300 °C, which are much better than copper nanowires (220 °C). Among the electrodes, Cu/Au nanotubes (220/140 °C) yield a significantly larger current response with rapid, well-defined and stable electrochemical response.

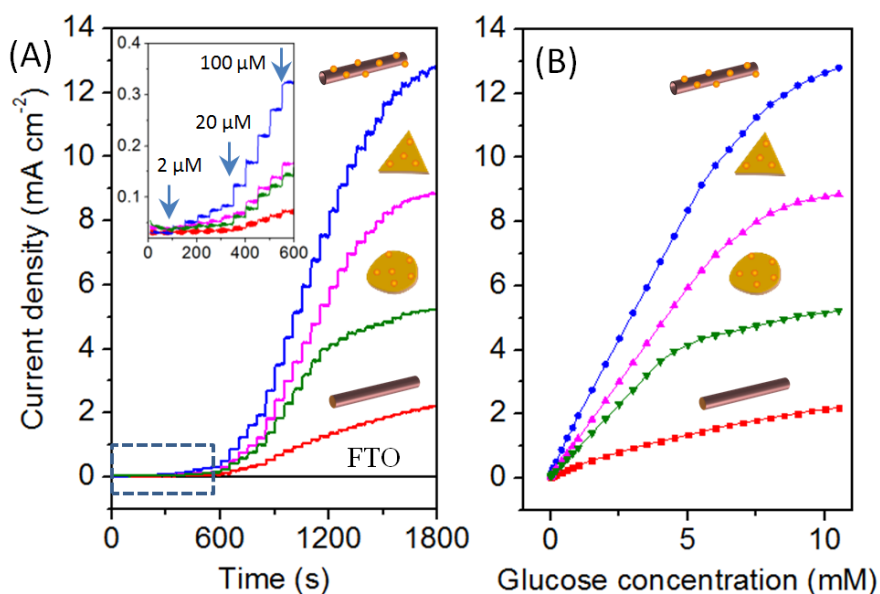


Figure 3.9 Electrocatalytic activities of Cu nanowires and Cu/Au nanostructures on FTO substrates as electrodes up to 1800 s. (A) Chronoamperometric curves of Cu nanowires (220 °C) and various Cu/Au nanostructures prepared at 220/140 °C, 220/220 °C and 220/300 °C at a constant potential of 0.6 V upon a successive addition of a glucose solution to obtain a cumulative concentration from 0 to 10.5 mM. Inset shows the enlarged current density region from 0-600 s. (B) The respective calibration curves of Cu nanowires and Cu/Au nanostructures.

The sensor exhibits an excellent linearity in a concentration range of 0 to 5.5 mM, which is expressed by $I = 0.138 + 1.656C$ with a correlation coefficient

0.99923, where I is current density in mA and C is concentration in mM (Figure 3.10). The sensitivity was found to be $1.656 \text{ mA mM}^{-1} \text{ cm}^{-2}$ with a low detection limit of $2 \text{ }\mu\text{M}$. The great sensing capability is firstly attributed to the synergistic effect from the incorporation of gold to copper nanostructures. The small amount of gold brings a significant effect on the sensing performance. Secondly, with the introduction of 3 mmol% Au relative to initial copper precursor, the resulting Cu/Au nanostructures with different shapes play different role in determining the glucose oxidation. The high aspect ratio copper nanotubes with a larger surface area optimise the electroactive sites and facilitate mass transport leading to a higher sensitivity with higher current density as compared to other Cu/Au nanostructures. In overall, the enhanced electrocatalytic performance of Cu/Au nanotubes results from large surface area, enhanced chemical stability to maintain high conductivity and rapid electron transfer during test.

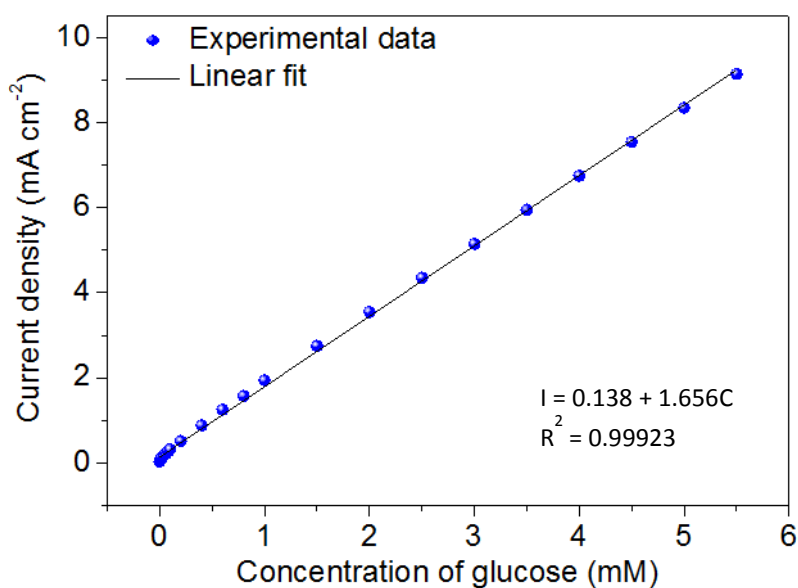


Figure 3.10 Linear range of Cu/Au nanotubes at 3 mol% Au (220/140 °C) as glucose sensors at an applied potential of 0.6 V.

3.3.3 Selectivity, stability and reproducibility of Cu/Au nanotubes towards glucose sensing

One of the important analytical factors for an amperometric biosensor is its high selectivity, which is crucial to discriminate other potential interfering species. In real physiological samples, many organic interfering species such as uric acid, ascorbic acid, acetaminophenol and dopamine normally co-exist with glucose

and generally the concentration of glucose is at least thirty times higher than those of the potential interfering species in human blood.²⁶⁸⁻²⁷⁰ In the present work, the selectivity of glucose sensors using bimetallic Cu/Au nanotubes was investigated by the amperometric response through successive testing 0.02 mM uric acid (very low water solubility), 0.1 mM ascorbic acid, 0.1 mM acetamidophenol and 0.1 mM dopamine followed by 1.0 mM glucose in 0.1 M sodium hydroxide solution. Other sugars including lactose, sucrose, maltose, mannose and fructose at a concentration of 0.1 mM were also tested. As shown in Fig 6, the glucose sensor demonstrates high selectivity with no significant response from the potential interfering species (Figure 3.11A) and other sugars (Figure 3.11B), exhibiting solely well-defined current of glucose oxidation.

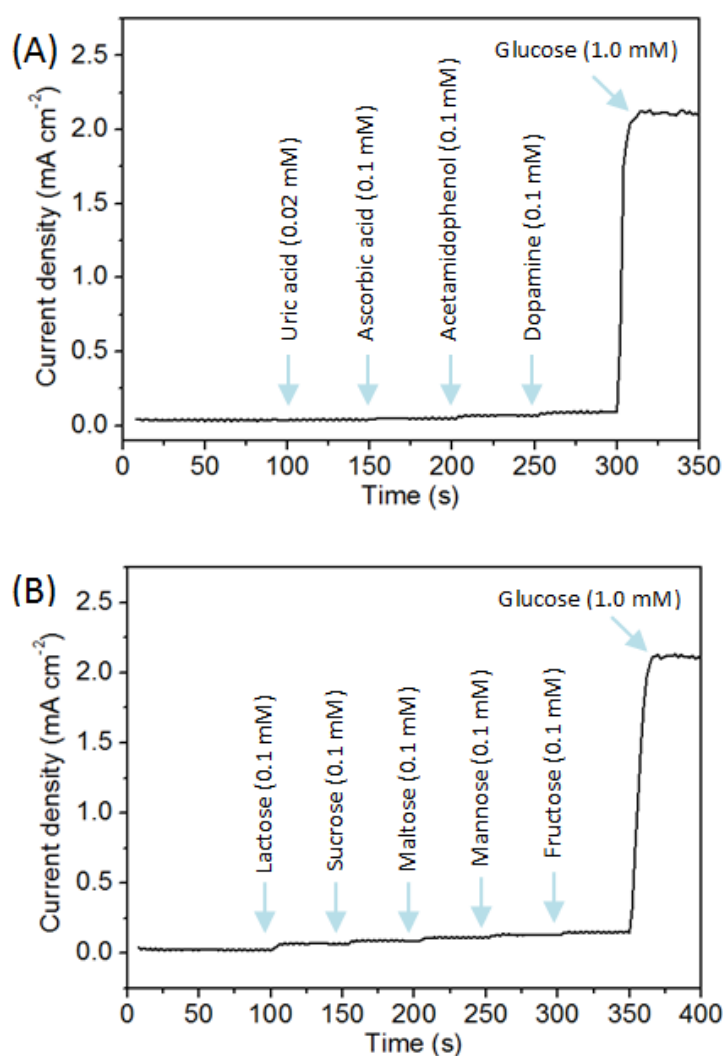


Figure 3.11 Amperometric response of Cu/Au nanotubes as an electrode at a potential of 0.6 V to various organic species in comparison with 1.0 mM glucose. (A) Various interfering species including 0.02 mM uric acid, 0.1 mM acetamidophenol, 0.1 mM ascorbic acid and 0.1

mM dopamine were tested at an interval of 50 s. (B) Various sugars including fructose, mannose, maltose, sucrose and lactose at a concentration of 0.1 mM were tested sequentially at an interval of 50 s. These concentrations are final concentrations prior to test.

The stability of the non-enzymatic glucose sensor based on Cu/Au nanotubes as an electrode was further evaluated intermittently for a period of 3 months. Figure 3.12 shows the amperometric response of the same electrode to 3.0 mM glucose solution for 1000 s at the beginning of 1 day, 2 day, 1 month and 3 months. After each test, the electrode was washed with deionised water and stored at room temperature for the next test. A reproducible current response was observed for a period of 3 months. The electrocatalytic current response maintained more than 95 % of its initial value, indicating a long-term stability of the non-enzymatic glucose sensor. The aging tolerance result is promising for recycling the sensing elements rather than the current disposable strips.

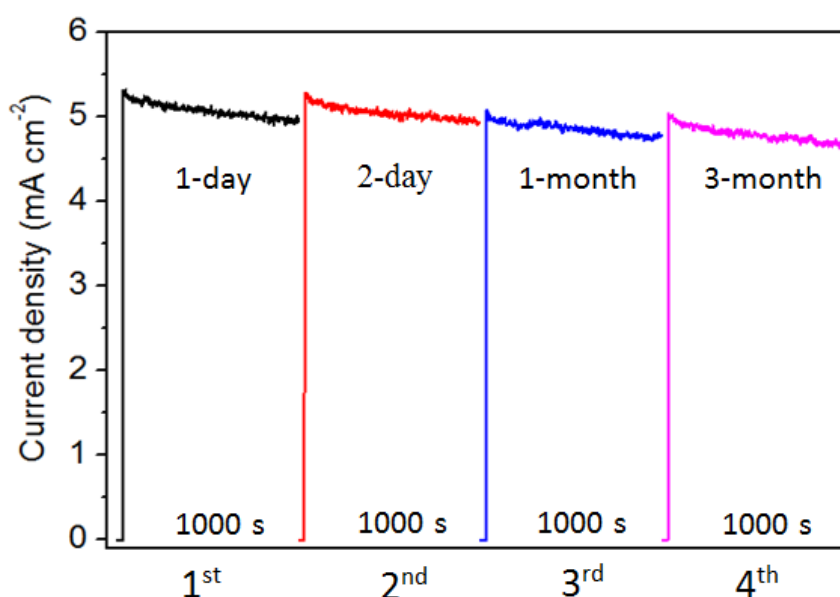


Figure 3.12 Amperometric response of bimetallic Cu/Au nanotubes as an electrode to 3.0 mM of glucose at a potential of 0.6 V. The stability test was conducted at the beginning of 1 day, 2 days, 1 month and 3 months. The glucose solutions were freshly prepared prior to each test for 1000 s.

3.3.4 Influence of Au loading in Cu/Au nanostructures on glucose sensing

By introducing a low level of Au³⁺ with a molar ratio of Au³⁺/Cu⁺ at 1:30 (i.e., 3 mol%), various bimetallic Cu/Au@3% nanostructures were prepared during thermal heating copper nanowires at 140, 220 and 300 °C, exhibiting great electrocatalytic activities to glucose oxidation. With the incorporation of Au, the

resulting bimetallic Cu/Au nanotubes prepared at 140 °C demonstrated its best performance as compared to the others. While maintaining the other reaction conditions the same as the preparation of Cu/Au nanotubes, the loading of gold was greatly reduced to 1 and 0.1 mol% (i.e., molar ratios of $\text{Au}^{3+}/\text{Cu}^+$ at 1:100 and 1:1000). The resulting Cu/Au@1% and 0.1% nanostructures were analysed by TEM as shown in Figure. 3.13. At 1 mol%, the Cu/Au@1% shows porous nanowire with obvious corrosion pits formed throughout the surface. At 0.1 mol%, the Cu/Au@0.1% shows non-porous nanowires with selectively etched. Apparently, the very low level incorporation of gold was not very effective to influence the surface of copper nanowires.

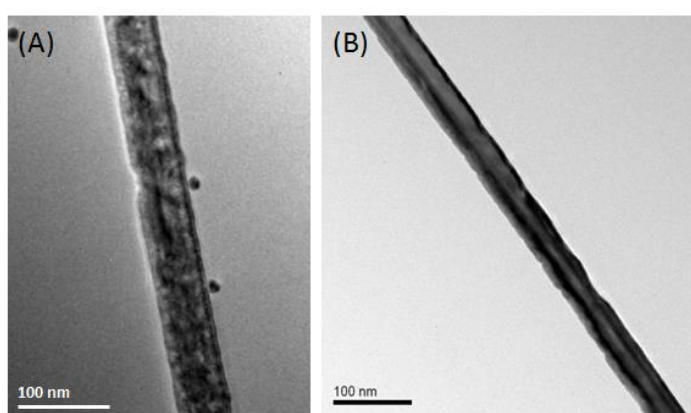


Figure 3.13 TEM images of (A) Cu/Au@1% and (B) Cu/Au@0.1% nanostructures prepared by heating Cu nanowires at 140 °C after the introduction of a lower level of Au^{3+} with a molar ratio of $\text{Au}^{3+}/\text{Cu}^+$ at 1:100 and 1:1000, respectively.

Similarly, the electrochemical responses of Cu/Au@1% and Cu/Au@0.1% nanostructures as electrodes were tested by a successive addition of glucose solutions with a cumulative concentration range from 0 to 10.5 mM in Figure. 3.14.

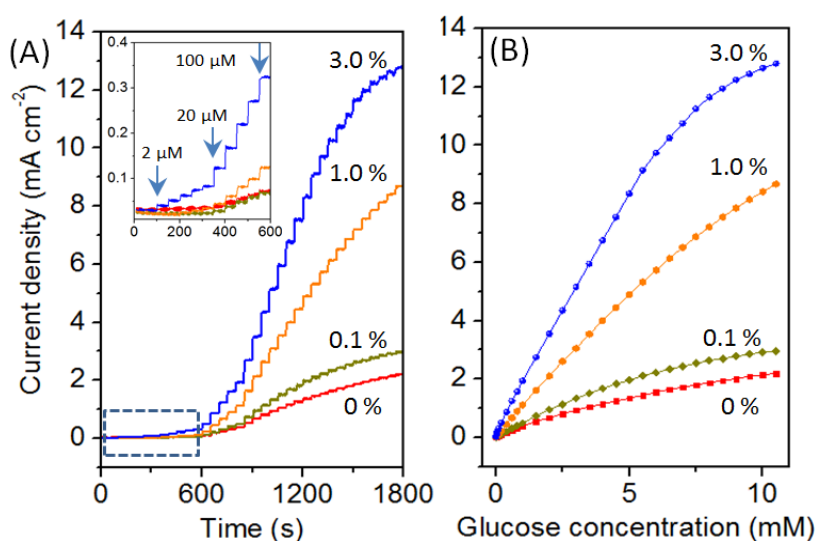


Figure 3.14 Electrocatalytic activities of different Au-incorporated Cu nanowires with different incorporation levels of 0.1, 1 and 3 mol% Au on FTO substrates as electrodes up to 1800 s. (A) Chronoamperometric curves of Cu nanowires (220 °C) and Cu/Au nanostructures prepared at 220/140 °C at a constant potential of 0.6 V upon a successive addition of a glucose solution to obtain a cumulative concentration from 0 to 10.5 mM. Inset shows the enlarged current density region from 0-600 s. (B) The respective calibration curve of Cu nanowires and Cu/Au nanostructures.

Interestingly, the chronoamperometric profile of Cu/Au@0.1% exhibits a clear improvement in current density at a fixed potential of 0.6 V as compared to copper nanowires. In contrast, the chronoamperometric profile of Cu/Au@1% displayed significantly higher signals and generated steady-state current within one second, exhibiting linearity in a concentration range of up to 5 mM, and sensitivity of $0.991 \text{ mA mM}^{-1} \text{ cm}^{-2}$. This is expressed by $I = 0.048 + 0.991C$ with a correlation coefficient 0.99902 where I is current density in mA and C is concentration in mM (Figure 3.15). Clearly, the porous Cu/Au@1% nanowires exposed more electroactive sites and higher surface area for glucose molecules to adsorb and react, while the fast and sensitive electrocatalytic performance is attributed to the promoted electron transfer afforded by the incorporation of Au. In comparison, the CV analysis of the Cu/Au@1% shows a higher current response to glucose oxidation with a bigger area under the CV curves (Figure 3.16). The very low amount of gold loading in Cu/Au@1% resulted in much higher oxidation current response to almost four-fold compared to copper nanowires, and three-fold compared to Cu/Au@0.1%. As a consequence, Cu/Au@1% electrode with a lower gold loading is equipped with adequate sensitivity and linear range to be applied as glucose sensor, possessing comparable performance of Cu/Au@3% nanotubes in terms of high sensitivity and wide linear range.

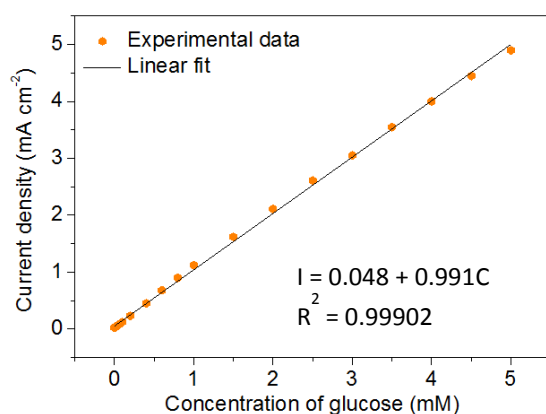


Figure 3.15 Linear range of Cu/Au porous nanowires at 1 mol% Au as glucose sensors at an applied potential of 0.6 V.

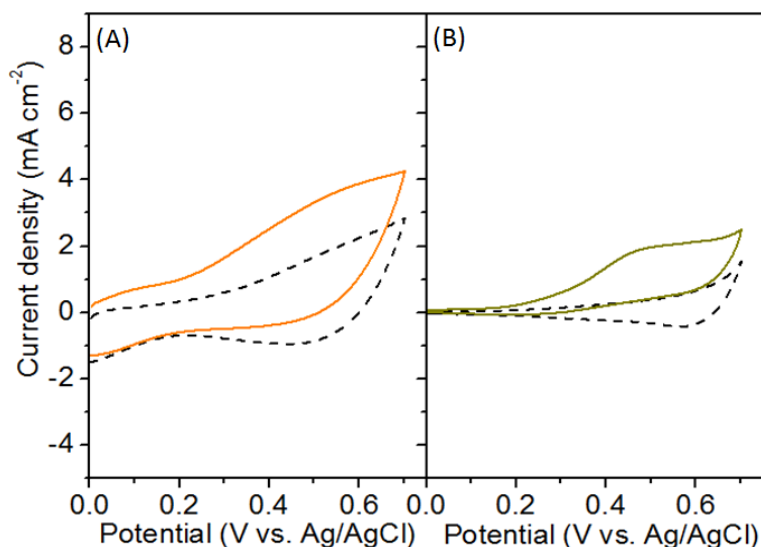


Figure 3.16 CV profiles of different composition Au-incorporated Cu nanowires on FTO substrates as electrodes at a potential window of 0-0.7 V (vs. Ag/AgCl) and a scan rate of 50 mV s^{-1} without (---- dash line) and with (— solid line) 3.0 mM of glucose. (A) Molar ratio of Au/CuCl at 1:100 (i.e., 1 mol% Au) and (B) molar ratio of Au/CuCl at 1:1000 (i.e., 0.1 mol% Au).

3.3.5 Colloidal synthesis of bimetallic Cu/Ru nanostructures

In addition to bimetallic Cu/Au nanostructures, the monometallic Cu nanowires can be used as template for the fabrication of CuRu nanostructures. As observed, the reduction of Ru^{3+} in oleylamine occurs at a much higher temperature of $\sim 270^\circ\text{C}$ than that for the disproportionation of CuCl, and it led to the formation of uniform Ru nanoparticles at an elevated temperature of $\sim 270^\circ\text{C}$ (Figure 3.17A). The as-synthesized Ru nanoparticles gave a very broad XRD peak, and the amorphous phase remained after annealing at 150, 200, 250, 300 and 350 $^\circ\text{C}$. At 400 $^\circ\text{C}$, the phase started to crystallize as indicated by the newly formed sharper peaks imposed on the amorphous one. At 450 $^\circ\text{C}$ and above, fully crystallized structure was observed by a set of very intense peaks at 38.4° , 42.3° and 44.0° , corresponding to the (100), (002) and (101) crystal planes of hexagonal phase Ru (JCPDS 006-0663), respectively. This study shows that amorphous Ru nanoparticles were stable at annealing temperature below 400 $^\circ\text{C}$. At higher temperature, the amorphous phase converted to hexagonal phase without the formation of RuO_2 , as evidenced from the XRD analysis.

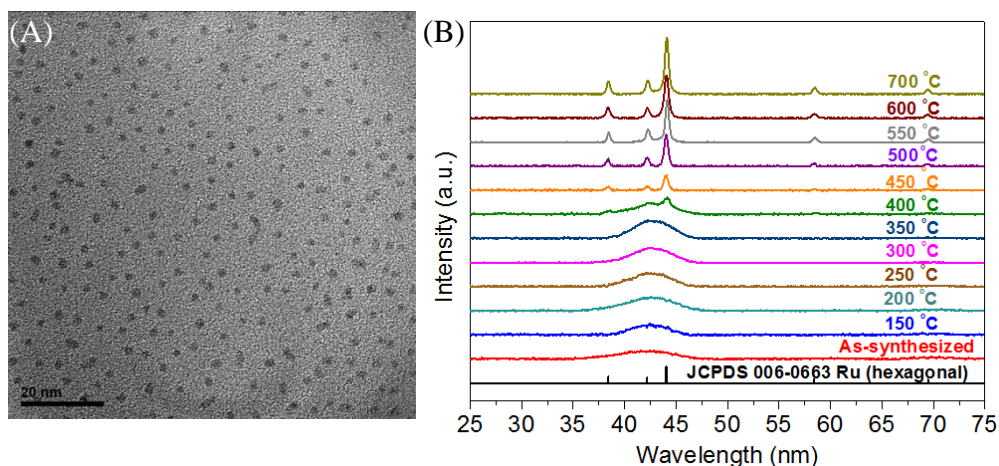


Figure 3.17 (A) TEM of as-synthesized Ru nanoparticles and (B) XRD of as-synthesized and annealed Ru nanoparticles from 150 to 700 °C in Ar atmosphere.

In order to prevent reversed disproportionation of Cu, the incorporation of Ru^{3+} was carried out in purified copper nanowires at 270 °C to yield bimetallic Cu/Ru nanostructures. Experimentally, copper nanowires were first prepared at 220 °C, purified and subsequently it was added simultaneously with Ru^{3+} to a heated oleylamine at 270 °C. The morphology of nanostructures analysed by TEM is presented in Figure 3.18A. TEM image shows the formation of bimetallic Cu/Ru nanowires with Ru nanoparticles on the surface of Cu nanowires. The respective XRD pattern in Figure 3.18B shows the metallic Cu diffraction peaks at 43.5, 50.7 and 74.4° together with an additional overlapping bump at 44°, which is indexed to the (101) of hcp structure of Ru (JCPDS #06-0663). The Cu/Ru phases remain unchanged after annealing at 220 °C. Since the annealing temperature at 220 °C is not high enough to cause a crystalline structure, the Ru phase in Cu nanowires is amorphous.

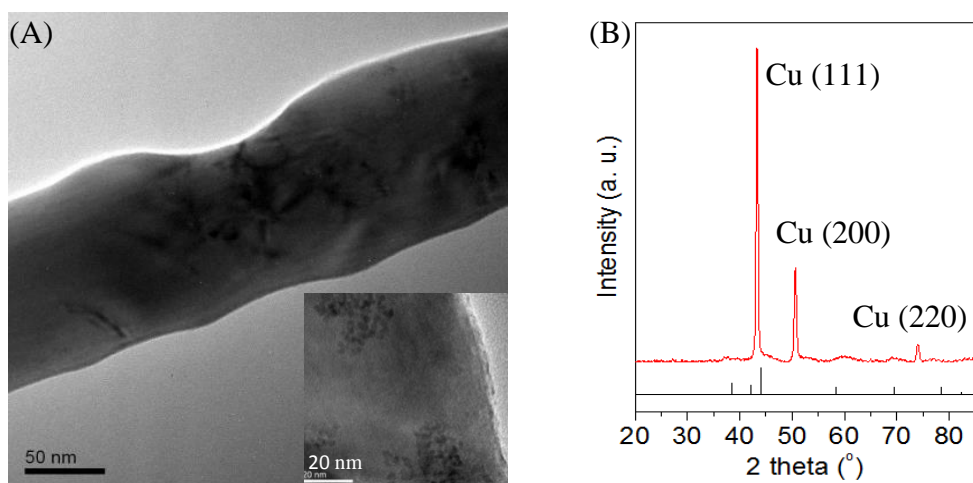


Figure 3.18 TEM image of bimetallic Cu/Ru nanowires prepared by reacting Cu nanowires with 0.1 mmol of RuCl₃ in oleylamine at 270 °C and enlarged surface of the nanowires at inset. (B) XRD pattern of the as-synthesized Cu/Ru nanowires with Ru JCPDS # 006-0663.

3.3.6 Electrocatalytic activities of bimetallic Cu/Ru nanostructures towards glucose sensing

Similarly, electrochemical activities of Cu/Ru nanowires electrode was tested at a fixed potential of 0.6 V by a successive addition of glucose solutions with a cumulative concentration range from 0 to 10.5 mM (Figure 3.19). Upon the successive addition of glucose, the chronoamperometric profile of Cu/Ru nanowires exhibits increment in current density. The Cu/Ru nanowires electrode responded rapidly achieving the steady-state current within 2 seconds. Such a rapid respond implies a fast electron transfer on the surface of Cu/Ru nanowires and a greater stability by incorporating Ru in the Cu nanowires. Moreover, amorphous Ru nanoparticles possess a higher concentration of coordinatively unsaturated sites with high degree of local structural flexibility, which makes adsorption of reactants easier than on the corresponding crystalline counterparts.⁶⁷ This increases the reaction activity, as compared with pristine Cu nanowires, the catalytic current density of Cu/Ru nanowires is significantly higher. The linear response of Cu/Ru nanowires electrode with respect to glucose concentration is observed at up to 5 mM.

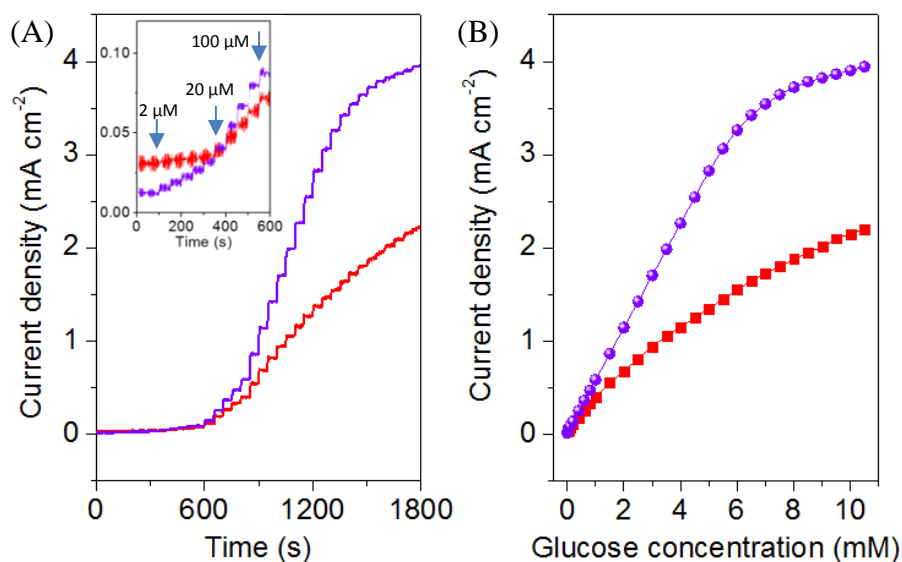


Figure 3.19 Electrochemical activities of Cu nanowires and Cu/Ru nanowires on FTO substrates as electrodes up to 1800 s. (A) Chronoamperometric curves of Cu nanowires (220 °C) and Cu/Ru nanostructures prepared at 220/270 °C at a constant potential of 0.6 V upon a successive addition of a glucose solution to obtain a cumulative concentration from 0 to 10.5

mM. Inset shows the enlarged current density region from 0-600 s. (B) The respective calibration curves of Cu nanowires and Cu/Ru nanowires.

3.4 Summary

Bimetallic Cu/Au nanostructures were successfully prepared by the controlled disproportionation of Cu^+ -oleylamine complex to form copper nanowires and the subsequent reaction with Au^{3+} at 140, 220 and 300 °C. A very low level incorporation of Au into Cu nanostructures can form bimetallic Cu/Au nanostructures at 140 °C by introducing 3, 1 and 0.1 mol % Au relative to Cu precursor used. This is to achieve their synergistic effect through the combined use of the merits of low-cost transition and high-stability noble metals. Among various Cu/Au and Cu/Ru nanostructures, the highly stable Cu/Au nanotubes exhibit the best performance towards glucose oxidation, originating from the high conductivity of Au and the high aspect ratio Cu nanotubes with high surface area so as to optimise the electroactive sites and facilitate mass transport. The present Cu/Au nanotubes demonstrated fast response, low detection limit and high sensitivity/selectivity. Promisingly, the long-term stability and recyclable features render them a promising strategy to extend non-enzymatic glucose sensors beyond disposable strips in future application.

Chapter 4
Rare Earth Metal Oxides for Sensing
Application

4.1 Introduction

Rare earth (RE) incorporated inorganic nanoparticles possess superior physicochemical features such as large Stokes and/or anti-Stokes shifts, narrow emission bands, long luminescence lifetimes (from several to tens of milliseconds), inherent photostability and low toxicity. These unique properties make them potential candidate for application in biolabelling, bioimaging, drug delivery, biological and analytical sensing for biological materials and metal ions, as well as light-emitting and photovoltaic devices for energy conversion.^{148, 164, 203} The intrinsic high color emissions are due to their f-f or f-d internal orbital transitions. Trivalent terbium ions (Tb^{3+}) have been expected as one of the promising activators that produce characteristic green emission transitions arising from the excited state $^5\text{D}_4$ to the lower energy state $^7\text{F}_J$ ($J=6, 5, 4, 3$). A considerable amount of work on the optical properties of Tb^{3+} doped in different inorganic host has been reported.^{148, 163, 167, 168} Typically, a low-incorporation level of <5-10 mol% rare earth luminescent centers is achieved and beyond this point, saturation of the luminescent intensity takes place due to the concentration quenching effect. This long-standing issue has been an on-going challenge in the potential application of RE.

To obtain desired RE ions incorporated inorganic nanoparticles, wet chemistry routes were modified in many ways to make the synthesis more efficient and to prepare particles with nanodimensions. In most cases, synthetic routes such as coprecipitation,¹⁴⁴ hydrothermal synthesis,^{271, 272} sol-gel method,^{143, 156} and colloidal chemistry are extensively used because starting materials in these methods can be mixed at molecular level and the reaction temperature for the formation of desired products is relatively low. Subsequently, post heat treatment is usually required to remove OH^- groups and/or crystal water molecules attached on the particle surface or in host lattice that may quench the luminescence.²⁷³ Moreover, the elevated temperature on Tb^{3+} may favor the formation of Tb^{4+} . Therefore further refinement in the synthetic process is highly desirable to alleviate the drawbacks of high temperature treatment process to improve energy efficiency.

In this work, amorphous Tb-incorporated ZrO_2 nanoparticles were synthesized with a tunable molar percentage of Tb^{3+} from 0 to 100 mol%, and a high incorporation-level of 50 mol% was achieved before the saturation of the luminescence occurred. The

critical role of ZrO_2 in $\text{ZrO}_2:\text{Tb}^{3+}$ nanoparticles helps to effectively disperse the luminescence centers (Tb^{3+}) in amorphous metal oxide matrices and minimizes nonradiative energy transfer, resulting in superior photoluminescence and photostability.¹⁴⁸ The well-known heavy trivalent Tb^{3+} ions can exhibit an intense $4f^8-4f^75d^1$ transition besides the intra-configuration f-f transition. The emission of this f-d transition exhibits unique interparticle distance dependent properties in solution, while their luminescence can be enhanced by several folds in a certain distance, but quenched in close proximity to another luminescent center. Moreover, the 2 nm size nanoparticles possess the surface atomic percentage of >80 % and thus making them extremely sensitive towards foreign influences.

Using these optimized parameters, a sensitive sensing approach was proposed for the detection of chemical contaminants (i.e., pesticides/herbicides) through the quenching of PL arising from the $4f^8-4f^75d^1$ transition. Chemical contaminants such as pesticides and herbicides are employed in agriculture worldwide, leading to the widespread contamination to environment, agricultural products and potentially hazardous to human body which causes serious health implication.²⁷⁴⁻²⁷⁶ The current detection methods of these chemical contaminants are usually involve with the use of time-consuming, cumbersome and expensive gas chromatography coupled to mass spectrometer, high-performance liquid chromatography or biological immunoassay.²⁷⁷⁻²⁸³ To date, it still remains great challenge to develop a fast detection of pesticides and herbicides. Towards achieving this aim, the highly luminescent $\text{ZrO}_2:\text{Tb}^{3+}$ nanoparticles in organic colloidal solution provide a simple, inexpensive and rapid implementation for the luminescent-based sensing of chemical contaminants. The high quenching efficiency of the $\text{ZrO}_2:\text{Tb}^{3+}$ PL in ppm and ppb level is particularly sensitive towards the electron withdrawing/electron deficient analytes which commonly found in pesticides, herbicides, drugs, and industrial waste.

4.2 Experimental section

4.2.1 Materials

Terbium (III) acetate hydrate (99.9%) was purchased from Alfa Aesar. Zirconium propoxide (70 wt% in 1-propanol), oleic acid (90%), oleylamine (70%), 1-octadecene (90%), nitrobenzene (99.5%), fenitrothion (analytical standard), paraoxon-ethyl (analytical standard), paraoxon-methyl (analytical

standard) and carbaryl (analytical standard) were purchased from Sigma-Aldrich.

4.2.2 Colloidal synthesis of $\text{ZrO}_2\text{:Tb}^{3+}$ nanoparticles

All experiments were carried out by standard oxygen-free techniques under nitrogen flow. In a typical preparation of $\text{ZrO}_2\text{:Tb}^{3+}$ (50 mol% Tb) nanoparticles, a mixed solution of terbium acetate (0.5 mmol), oleic acid (5 mmol), and 1-octadecene (6 mL) was dried and degassed at 90 °C in a 25-mL three-neck flask for 1 hour. Then zirconium propoxide (0.5 mmol) was injected into the mixed solution and heated for 10 minutes. The solution gradually turned from colorless to pale yellow, indicating the formation of zirconium-terbium carboxylate complexes. Gaseous isopropyl alcohol was rapidly released while the mixture was heated to 300 °C for 10 minutes. The aminolysis reaction was then initiated by rapid injection of oleylamine (4 mmol) with vigorous stirring. The resulting solution was kept at 300 °C for 1 hour. Then the final mixture was allowed to cool to room temperature. The resulting crude solution of $\text{ZrO}_2\text{:Tb}^{3+}$ nanoparticles was diluted with hexane (10 mL) followed by precipitation with acetone (20 mL). The crude product was recovered by centrifugation, dispersed in hexane (20 mL), and subjected to a second round of purification. The product obtained can be re-dispersed easily in hexane (30 mL) for further characterization. It can also be redispersed in other nonpolar solvents such as chloroform and toluene. The above procedures were repeated for 5, 10, 25, 40, 60, 75, 90 mol% Tb^{3+} in ZrO_2 , 100 mol% of Tb_2O_3 and 100 mol% ZrO_2 .

4.2.3 Measurement of luminescent response with respect to dilution in hexane

Typically, 1 mmol $\text{ZrO}_2\text{:Tb}^{3+}$ nanoparticles were dispersed in 5 mL hexane followed by dilution by 2, 3, 4, 6, 12, 18, 24, 30, 36, 42, 48, 54, 60, 90, 120 times which corresponds to a concentration range of 1.1×10^{18} (pristine), 5.6×10^{17} , 3.8×10^{17} , 2.8×10^{17} , 1.9×10^{17} , 9.4×10^{16} , 6.3×10^{16} , 4.7×10^{16} , 3.8×10^{16} , 3.1×10^{16} , 2.7×10^{16} , 2.4×10^{16} , 2.1×10^{16} , 1.9×10^{16} , 1.3×10^{16} and 9.4×10^{15} particles/mL.

4.2.4 Measurement of luminescent response to pesticides

In a typical procedure, 2 mL of $\text{ZrO}_2\text{:Tb}^{3+}$ dispersion in hexane (6.3×10^{16} particles/mL) was added to a quartz cuvette. Then, known concentration of pesticides in hexane

was injected into the above solution to obtain the desired final pesticide concentration and luminescent responses were recorded immediately. For the study of PL stability of $\text{ZrO}_2:\text{Tb}^{3+}$ under time effect, the evolution of luminescent responses was recorded for a specific time interval after mixing the pesticide and $\text{ZrO}_2:\text{Tb}^{3+}$ solution in the cuvette. The same procedure was performed using pristine $\text{ZrO}_2:\text{Tb}^{3+}$ solution as a control.

4.2.5 Sample preparation for characterisation

TEM images and EDX were recorded on a Philips CM 300 FEG transmission electron microscope (300 kV). TEM samples were prepared by depositing a drop of diluted colloidal nanoparticles in hexane on copper grids and dried under ambient conditions. XRD of samples on Si substrates was performed with a Bruker General Area Detector Diffraction System using Cu $K\alpha$ radiation ($\lambda = 1.54 \text{ \AA}$). Luminescent spectra were measured with a Shimadzu RF-5301 PC fluorometer. Optical spectra in hexane medium were measured with a Shimadzu UV-3150 spectrophotometer.

4.3 Results and Discussion

4.3.1 Colloidal synthesis of $\text{ZrO}_2:\text{Tb}^{3+}$ nanoparticles

In this study, monodisperse $\text{ZrO}_2:\text{Tb}^{3+}$ nanoparticles were synthesized via a nonhydrolytic synthetic approach. It was developed by firstly the formation of M-oleates (M: Zr, Tb) by ligand exchange in solution, followed by decomposition of the M-

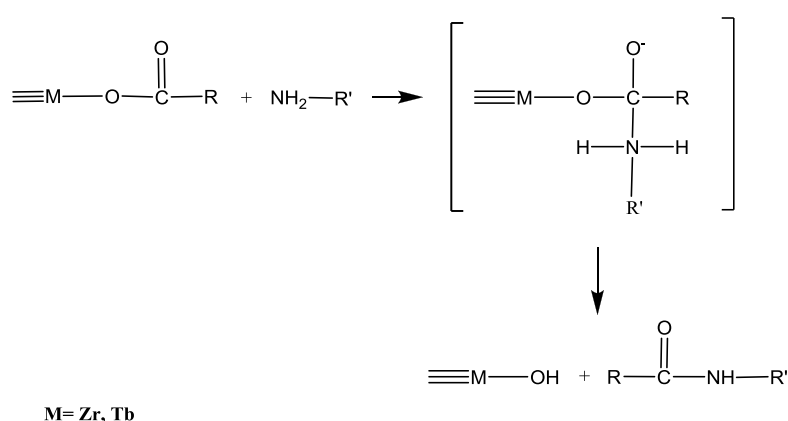


Figure 4.1 Aminolysis reaction between terbium-zirconia carboxylate complexes and primary amine.

oleates into M-oxides catalyzed by the base of oleylamine that involves the nucleophilic attack of an amine group on the carbonyl carbon atom of M-oleates derivatives (Figure 4.1).¹⁰⁹ With the developed synthetic method, high quality luminescent nanoparticles with different Tb³⁺ content in ZrO₂ was developed from 0, 5, 10, 25, 40, 50, 60, 75, 90 to 100 mol%.

4.3.2 Optical properties of ZrO₂:Tb³⁺ nanoparticles

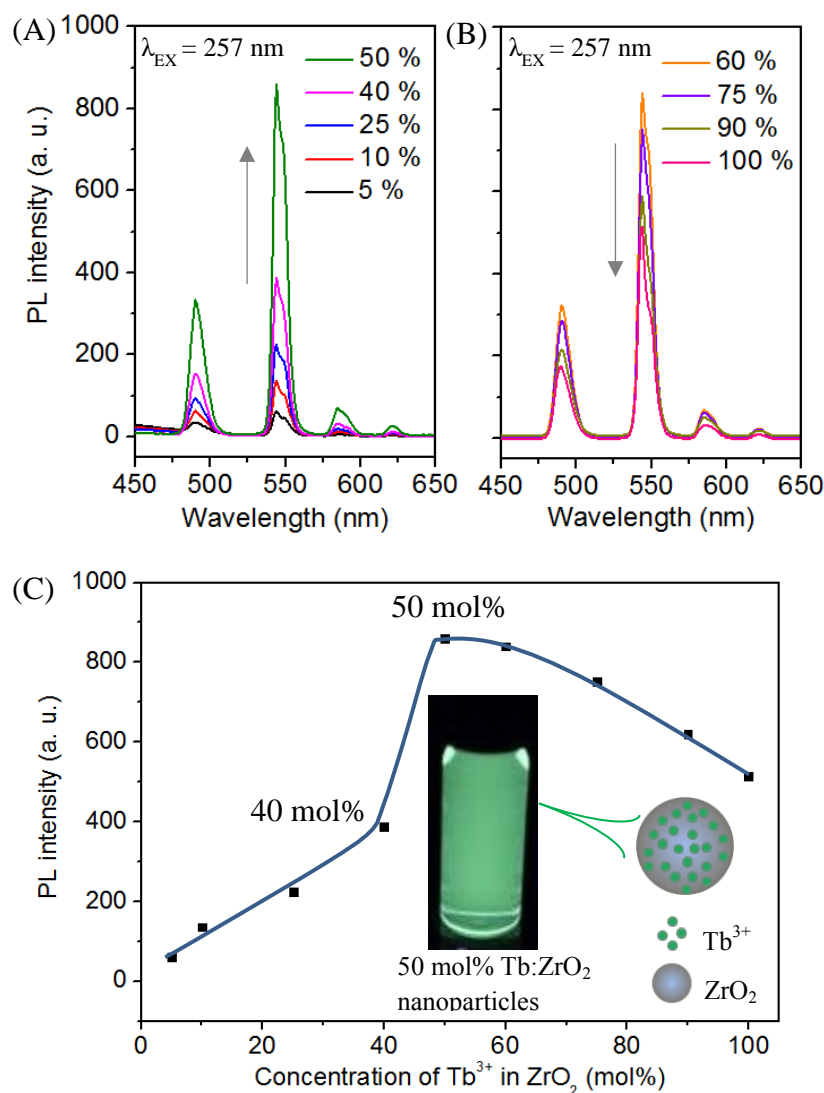


Figure 4.2 Emission spectra of Tb-incorporated ZrO₂ nanoparticles excited at 257 nm: (A) 5-50 mol% and (B) 60-100 mol% of Tb³⁺ in ZrO₂. (C) Maximum emission intensity at ⁵D₄→⁷F₅ transition (545 nm, excited as 257 nm) as a function of Tb³⁺ composition ranging from 5-100 mol% of Tb³⁺ in ZrO₂. Insets show the photograph of 50 mol% (1.9×10¹⁷ particles/ mL) ZrO₂:Tb³⁺ colloidal dispersion in hexane excited on a 302 nm UV illuminator.

Upon UV excitation at 257 nm, green emission of Tb³⁺ was observed and the corresponding PL emission spectra were measured at room temperature (Figure 4.2A-

B). The characteristic green emission peaks resulting from 4f→4f transitions within Tb³⁺ ions which consist of the intense peak at 545 nm corresponding to the ⁵D₄→⁷F₅ transition. Three other peaks are observed at 488 nm (⁵D₄→⁷F₆), 586 nm (⁵D₄→⁷F₄), and 621 nm (⁵D₄→⁷F₃) (Figure 4.3A). The relative intensities of the emission bands vary for the different degree of Tb³⁺ content. Figure 4.2C shows the maximum emission intensity of ⁵D₄→⁷F₅ transition as a function of Tb³⁺ content. The plot reveals that the increasing Tb³⁺ content from 5 to 50 mol% results in an increase of emission intensity (Figure 4.2A) whereas further increase the Tb³⁺ content to 60, 75, 90 and 100 mol% causes the PL to quench gradually (Figure 4.2B). The greatest concentration enhanced emission was observed in the 50 mol% ZrO₂:Tb³⁺ nanoparticles, showing 14 times stronger than the 5 mol% counterpart.

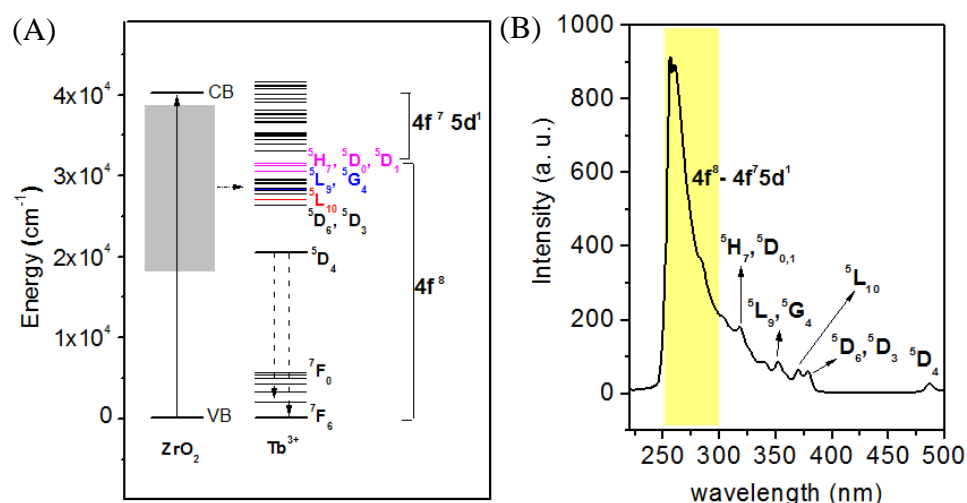


Figure 4.3 (A) Schematic diagram of energy transfer from Zr⁴⁺ to Tb³⁺. The up solid arrow represents photoexcitation and the down dash arrows denote emission. (B) Room temperature excitation spectrum of 50 mol% ZrO₂:Tb³⁺ nanoparticles monitored at 545 nm with concentration fixed at 1.9×10¹⁷ particles/ mL in hexane. The yellow highlighted region represents the f-d transition.

The excitation spectra of the corresponding ZrO₂:Tb³⁺ nanoparticles were monitored at 545 nm (4.4A-B), typically it consists of intense peak at ~260 nm and some other weaker peaks from 280 to 400 nm. With the changing Tb³⁺ content, the former intense peak shows significant variations in peak intensity while the latter weaker peaks show minor changes in the peak intensity. In accordance with the literature, the excitation spectrum of Tb³⁺ comprises of two types of transitions: f→d transition (220-290 nm) and f→f transition (290-500 nm). The f→d transition of Tb³⁺ in ZrO₂ nanoparticles is observed at an intense band at ~260 nm, which corresponds to the 4f⁸-4f⁷5d¹ transition

or simply the f-d band.^{272, 284} The f→f transition peaks centered at 488, 378, 369, 352, 317 nm have been assigned to the transition from ground state 7F_6 to the higher excited levels of 5D_4 , (5D_3 , 5D_6), $^5L_{10}$, (5L_9 , 5G_4), (5H_7 , $^5D_{0,1}$) respectively (Figure 4.3B). The corresponding excitation maxima as a function of Tb^{3+} content was monitored at 257 nm under excitation of 545 nm (Figure 4.4C). The excitation peak intensities at ~257 nm get intensified with increasing Tb^{3+} content from 5-50 mol% which matches well with the emission spectra. The increasing intensity is attributed to the larger number of luminescent centers and more excited ions are transitioned to the respective emitting level such as the 5D_4 . However, the increasing concentration of Tb^{3+} will only increase the intensity of PL up to a critical concentration, of which the luminescence is the saturation point. In this case, 50 mol% of Tb^{3+} is the saturation point and beyond this critical concentration, PL intensity gradually decreases. At higher Tb^{3+} concentrations of >50 mol%, interaction among Tb^{3+} ions causes an output-limiting effect. Concentra-

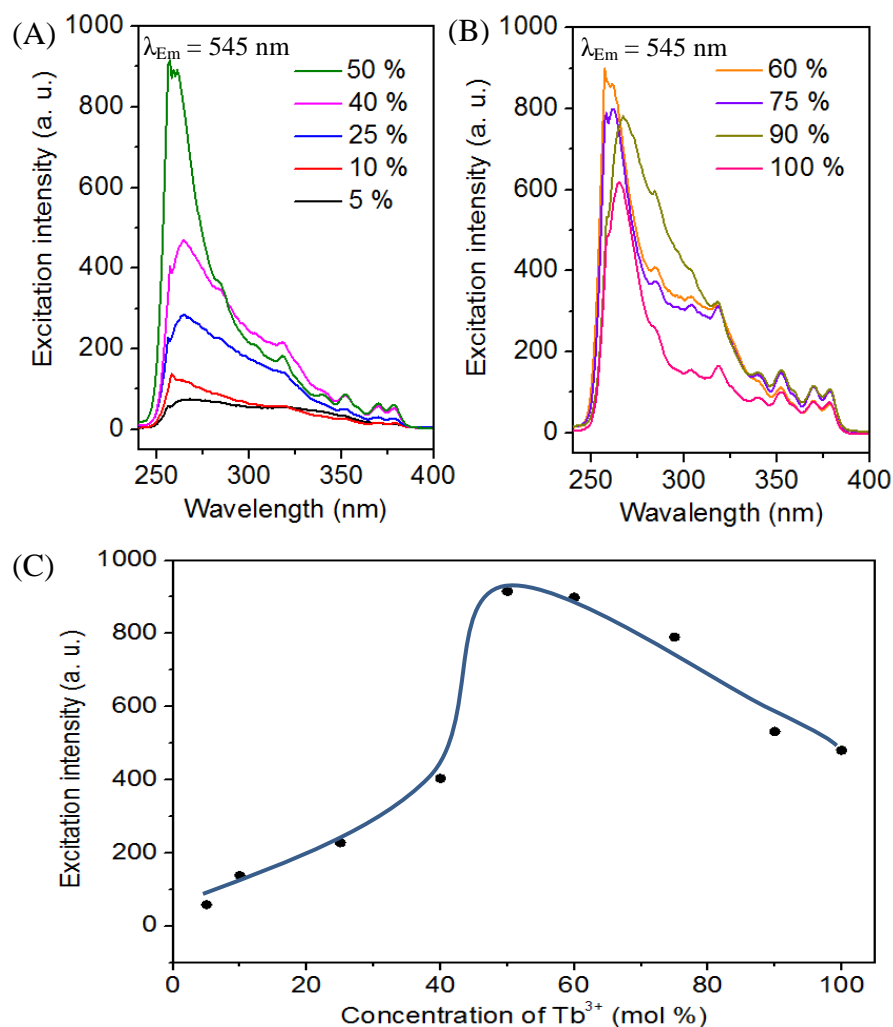


Figure 4.4 Excitation spectra of Tb-incorporated ZrO₂ nanoparticles excited at 545 nm: (A) 5 - 50 mol% and (B) 60-100 mol% of Tb³⁺ in ZrO₂. (C) Maximum excitation intensity at 4f⁸-4f⁷5d¹ transition (257 nm, excited as 545 nm) as a function of Tb³⁺ composition ranging from 5-100 mol% of Tb³⁺ in ZrO₂.

tion quenching beyond an optimal dopant concentration is due to energy transfer between adjacent luminescence centers via cross-relaxation. At high Tb³⁺ concentration, when two Tb³⁺ come into very close proximity, an excited Tb³⁺ deexcites the neighboring excited Tb³⁺ ion by energy transfer, and itself returns to the ground state by nonradiative relaxation. Therefore, this is observed in Tb³⁺ content of 60, 75, 90 and 100 mol%.

4.3.3 Interparticle-distance dependent PL of ZrO₂:Tb³⁺ nanoparticles

From the findings, the most intense luminescence was observed for the 50 mol% Tb-incorporated ZrO₂. The quantitative determination of the Tb-Zr atoms is determined by EDX which indicates the estimation of the each atom to be approximately 1:1 mol

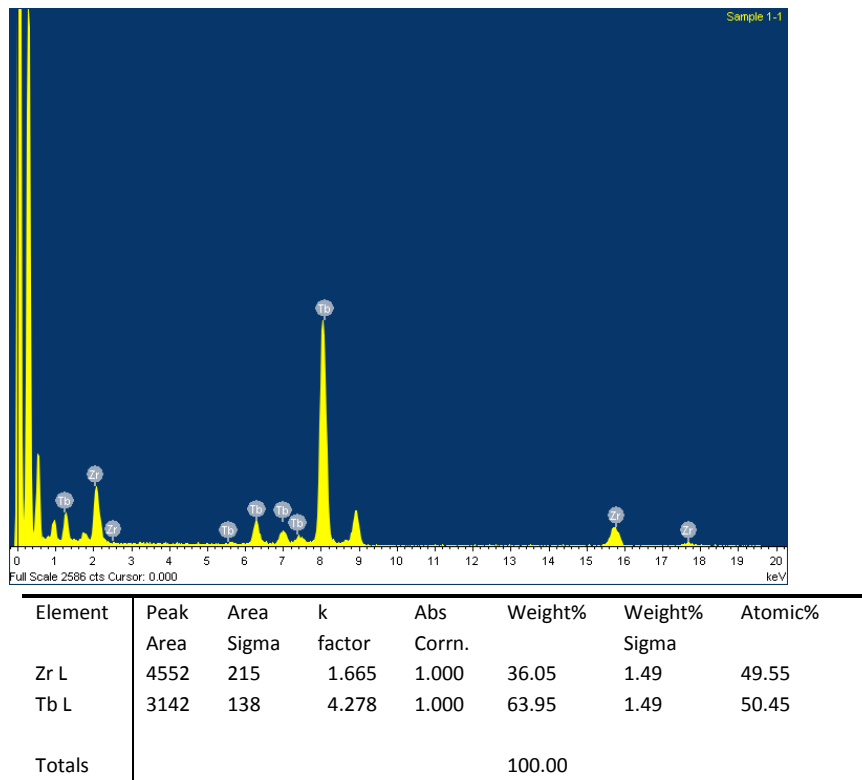


Figure 4.5 TEM EDX of 50 mol% ZrO₂:Tb³⁺ nanoparticles.

ratio (Figure 4.5). This system was chosen for a more accurate analysis, to further investigate the luminescence enhancement. The excitation spectra of ZrO₂:Tb³⁺ dispersion was measured by diluting the dispersion from 2 to 120 times ($\sim 1.1 \times 10^{18}$ to

$\sim 9.4 \times 10^{15}$ particles/ mL) in hexane (Figure 4.6A). It is observed that the f-d band which centered around 260 nm starts to develop at concentration of $\leq 3.8 \times 10^{17}$ particles/ mL. Upon diluting the $\text{ZrO}_2:\text{Tb}^{3+}$ dispersion, the significant increase in the luminescent intensity can be clearly shown from the intensified f-d transition peak at 257 nm. The most prominent luminescence enhancement can be observed at concentration of 6.3×10^{16} particles/ mL. Further diluting the dispersion causes the luminescence to become weaker. The result clearly shows the PL properties of $\text{ZrO}_2:\text{Tb}^{3+}$ nanoparticles is highly dependent on concentration. To achieve the optimum luminescence, a suitable distance between the nanoparticles is crucial. Therefore, an attempt was made to study the effect of interparticle distance of $\text{ZrO}_2:\text{Tb}^{3+}$ nanoparticles on the luminescence properties. Here, the interparticle distance is defined as the distance between the center of two particles and this separation distance can be determined by varying the concentration of $\text{ZrO}_2:\text{Tb}^{3+}$ nanoparticles in hexane. The variation of the luminescence properties of $\text{ZrO}_2:\text{Tb}^{3+}$ nanoparticles was carefully investigated as a function of interparticle distance by employing a simple model to define that the total solution volume is consisted of the sum of the volume of each individual nanoparticle, $V_{\text{solution}} = 4/3 \pi r^3 * N$, where V is the total solution volume, r is the radius of sphere volume and N is the number of $\text{ZrO}_2:\text{Tb}^{3+}$ nanoparticles in solution. The mathematical expression can then be expressed as interparticle distance, $d = 2(3V/4\pi N)^{1/3}$ which is equivalent to $2r$. In deriving our expression for the interparticle distance, d , we take advantage of the fact each $\text{ZrO}_2:\text{Tb}^{3+}$ nanoparticles developed are uniformly 2 nm spheres and monodispersed in dispersion (Figure 4.6A inset).

Figure 4.6B displays the interparticle dependent luminescence of $\text{ZrO}_2:\text{Tb}^{3+}$ nanoparticles with concentration ranging from $\sim 1.1 \times 10^{18}$ to $\sim 9.4 \times 10^{15}$ particles/ mL. When the interparticle distance of $\text{ZrO}_2:\text{Tb}^{3+}$ nanoparticles are increased from 10 to 31 nm, the luminescence intensity is found to be enhanced by 96 times. The luminescence intensity increases in a less concentrated Tb^{3+} environment by dispersing the Tb^{3+} distance apart and consequently minimizes the non-radiative energy transfer process. The optimal luminescence enhancement is observed at an interparticle distance of 31 nm (concentration of 6.3×10^{16} particles/ mL) and further increase of separation distance from 32 to 60 nm caused a decrease in luminescence properties. Overall, the effect of interparticle distance which is a function of concentration has great influence

on the f-d band (220-290 nm) band while less significant to f-f band (290-500 nm). The sensitivity of the f-d band at 257 nm can be attributed to the 4f-5d transition of Tb^{3+} which is greatly influenced by their surroundings. As well known, the 4f-5d transitions are different from the intra-4f transitions since the 4f-electrons are shielded by the 5s and 5p electrons. The 4f-5d transitions are more sensitive to the local environment surrounding the Tb^{3+} than the f-f transitions.

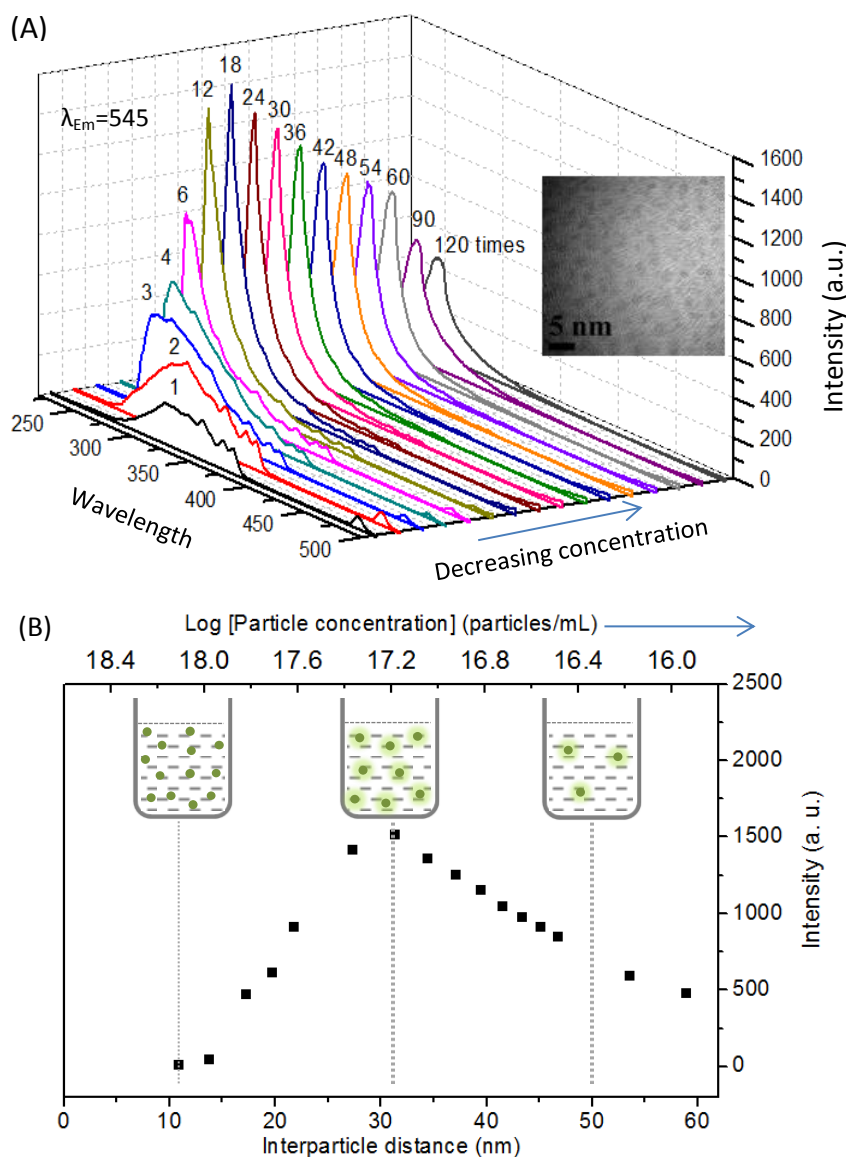


Figure 4.6 (A) Room temperature excitation spectra of as-synthesized 50 mol% $ZrO_2:Tb^{3+}$ nanoparticles (λ_{em} at 545 nm) with different concentrations in hexane (no. of particles/ mL) as labeled with 1 to 20 times, corresponding to dilution factor with respect to concentration ranging from $\sim 1.5 \times 10^{18}$ to $\sim 9.4 \times 10^{15}$ particles/ mL. Inset shows the TEM image of $ZrO_2:Tb^{3+}$ nanoparticles with average diameter of 2 nm. (B) Effect of the interparticle distance of 50 mol% $ZrO_2:Tb^{3+}$ nanoparticles on luminescent intensity. Luminescent intensity is obtained from the excitation maxima of different concentration monitored at 545 nm. The inset shows the schematic illustrations of the $ZrO_2:Tb^{3+}$ nanoparticles dispersed in hexane at different concentrations.

4.3.4 Detection of pesticides through PL quenching of $\text{ZrO}_2:\text{Tb}^{3+}$ nanoparticles

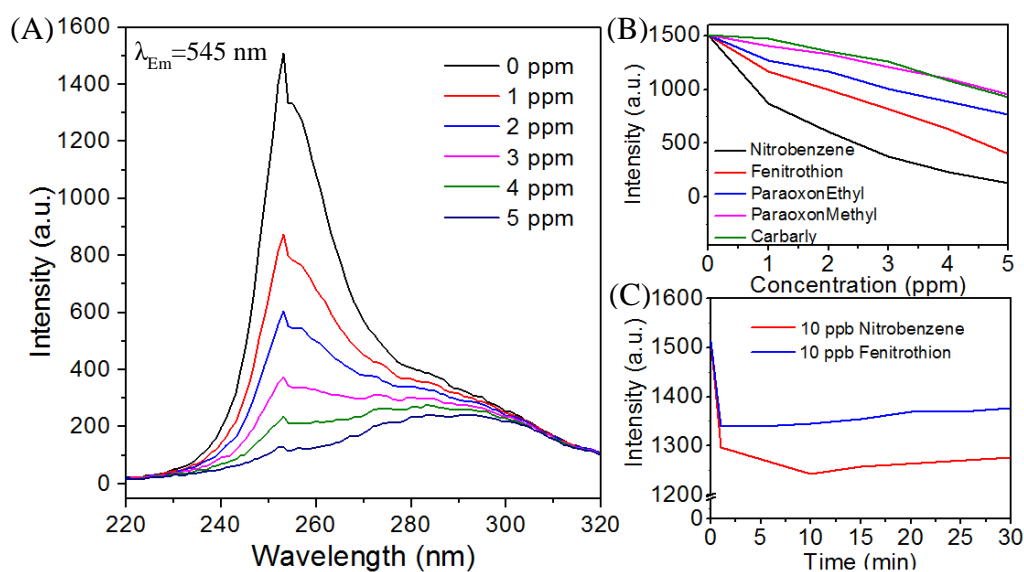


Figure 4.7 Sensitivity of 50 mol% $\text{ZrO}_2:\text{Tb}^{3+}$ nanoparticles responding to pesticides in the range of 1 to 5 ppm. Concentration of $\text{ZrO}_2:\text{Tb}^{3+}$ nanoparticles is fixed at 6.3×10^{16} particles/mL. (A) Excitation spectra of $\text{ZrO}_2:\text{Tb}^{3+}$ nanoparticles responding to nitrobenzene. (B) Luminescent quenching upon doping with different pesticides. (C) Luminescence stability of 50 mol% $\text{ZrO}_2:\text{Tb}^{3+}$ nanoparticles was tested with 10 ppb of nitrobenzene and fenitrothion for a period of 30 minutes.

The optimized concentration of 50 mol% $\text{ZrO}_2:\text{Tb}^{3+}$ nanoparticles (6.3×10^{16} particles/mL) are used as sensing material for nitroaromatic compounds due to the strong luminescent properties and the high sensitivity of the f-d band. The sensitivity of f-d band (λ_{em} at 545 nm) of $\text{ZrO}_2:\text{Tb}^{3+}$ nanoparticles responding to 1 to 5 ppm of nitrobenzene (Figure 4.7A) has demonstrated the quenching of luminescence occurred at a concentration of as low as 1 ppm. When reaching to 5 ppm, the luminescence is completely quenched by nitrobenzene. From this finding, the sensing of chemicals using is extended to pesticide materials such as fenitrothion, paraoxon ethyl, paraoxon methyl and carbaryl (Figure 4.7B). The range of pesticides concentration tested is from 1 to 5 ppm and the luminescent intensity is measured instantly upon pesticides addition. The order of sensitivity to pesticides is arranged in the order of nitrobenzene > fenitrothion > paraoxon-ethyl > paraoxon-methyl > carbaryl. The $\text{ZrO}_2:\text{Tb}^{3+}$ nanoparticles system is especially sensitive towards nitrobenzene and fenitrothion. Results reveal the excellent quenching efficiency of nitrobenzene at the f-d transition band even at 1 ppm level. This demonstrated that the strong $\text{ZrO}_2:\text{Tb}^{3+}$ luminescence

can sensitively respond to the presence of the aromatic compounds in solution through luminescent quenching. In particular, the electron deficient nitroaromatics are strong quenchers of the luminescent of the $\text{ZrO}_2\text{:Tb}^{3+}$ nanoparticles. Therefore, the extremely high quenching efficiency to the $\text{ZrO}_2\text{:Tb}^{3+}$ PL is thus achieved for electron withdrawing / electron deficient analytes which commonly found in pesticides, herbicides, drugs, industrial waste, etc. The limit of detection is further investigated down to ppb level. The $\text{ZrO}_2\text{:Tb}^{3+}$ nanoparticles (6.3×10^{16} particles/ mL) in hexane is tested with the two most sensitive pesticides such as nitrobenzene and fenitrothion. The response of optimized $\text{ZrO}_2\text{:Tb}^{3+}$ nanoparticles is measured with time when 10 ppb of pesticide is added. Luminescent result in Figure 4.7C indicates the instantaneous quenching of luminescent within 1 minute and this signal is stable over time up to 30 minutes. The above findings are definitely promising in terms of sensitivity, stability and response time.

4.3.5 Structure and composition study of $\text{ZrO}_2\text{:Tb}^{3+}$ nanoparticles

In order to investigate the PL properties of $\text{ZrO}_2\text{:Tb}^{3+}$ nanoparticles with respect to the structure and composition, as-synthesized $\text{ZrO}_2\text{:Tb}^{3+}$ nanoparticles with Tb^{3+} content ranges from 0 to 100 mol% are characterized by XRD. The 0 mol% in Tb content denotes 100 mol% Zr content. The obvious broadening of XRD lines (Fig. 4.8A) suggests a low crystalline structure. This is attributed to the fast formation of nanosized particles that are formed at high temperature by quick injection of oleylamine into the system which refrain the particle growth. As a result, a high proportion of atoms are located at or near the surface of nanoparticles, leading to disordered atoms arrangement at the core. Therefore, the synthesized nanoparticles are of low crystalline structure. It is also observed that the crystallinity decreases as the Zr^{4+} was gradually replaced by Tb^{3+} , particularly 100 mol% Tb_2O_3 is almost fully amorphous structure. This can be explained by the oxidation state of the metals, Zr carries a +4 charge which the ionic radius is smaller compared to Tb of +3 charges, smaller atoms are more feasible to form crystalline structure than the larger atoms. Hence, even under the same preparation condition, ZrO_2 is more crystalline than Tb_2O_3 . The positions of the 2θ (111) with changing Tb^{3+} content were investigated (Figure 4.8B). It is note that the positions of the 2θ show insignificant changes upon

replacing Zr^{4+} with Tb^{3+} , this observation is again support the as-synthesized $ZrO_2:Tb^{3+}$ nanoparticles are in random order of the amorphous structure.

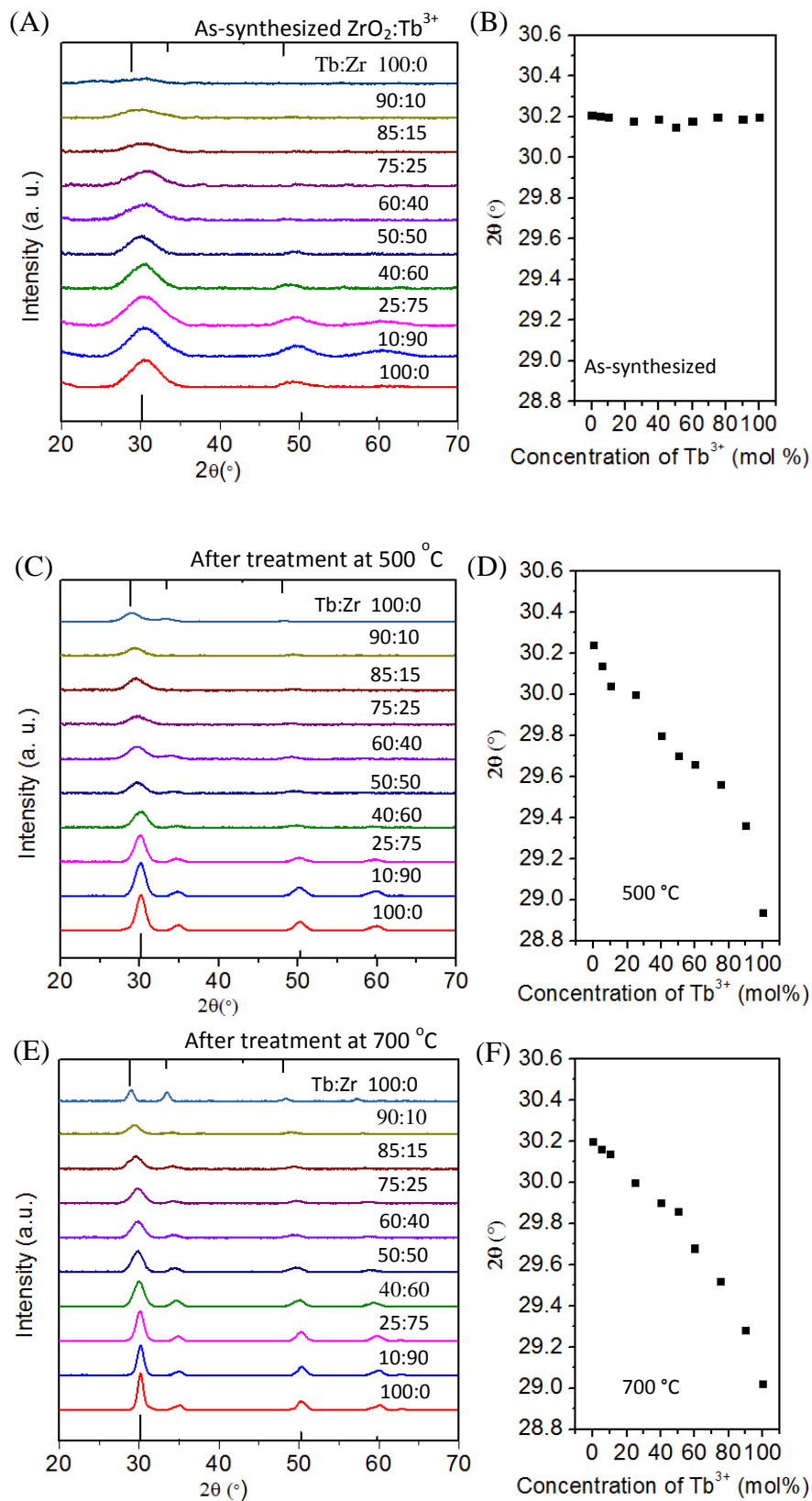


Figure 4.8 XRD diffraction pattern and their respective 2θ (111) as a function Tb^{3+} content of ZrO_2 , Tb -incorporated ZrO_2 nanoparticles with Tb^{3+} content ranges from 5-90 mol% of Tb^{3+} in ZrO_2 and Tb_2O_3 . (A-B) as-synthesized, (C-D) annealed at 500 °C, (E-F) 700 °C. The standard JCPDS file of Tb_2O_3 (23-1418) and ZrO_2 (49-1642) are shown on top and bottom respectively of the XRD diffraction plot.

To further evaluate the effect of crystal structure on the luminescence of nanoparticles, an annealing study of the nanoparticles was performed. Upon annealing the nanoparticles to higher temperatures of 500 °C (Figure 4.8C) and 700 °C (Figure 4.8E), the diffraction peaks become more intense and sharper due to an increase in crystallinity. At high annealing temperature, the diffraction peaks of 100% Tb^{3+} content and 100 % ZrO_2 can be well assigned to cubic phase JCPDS file #23-1418 and #49-

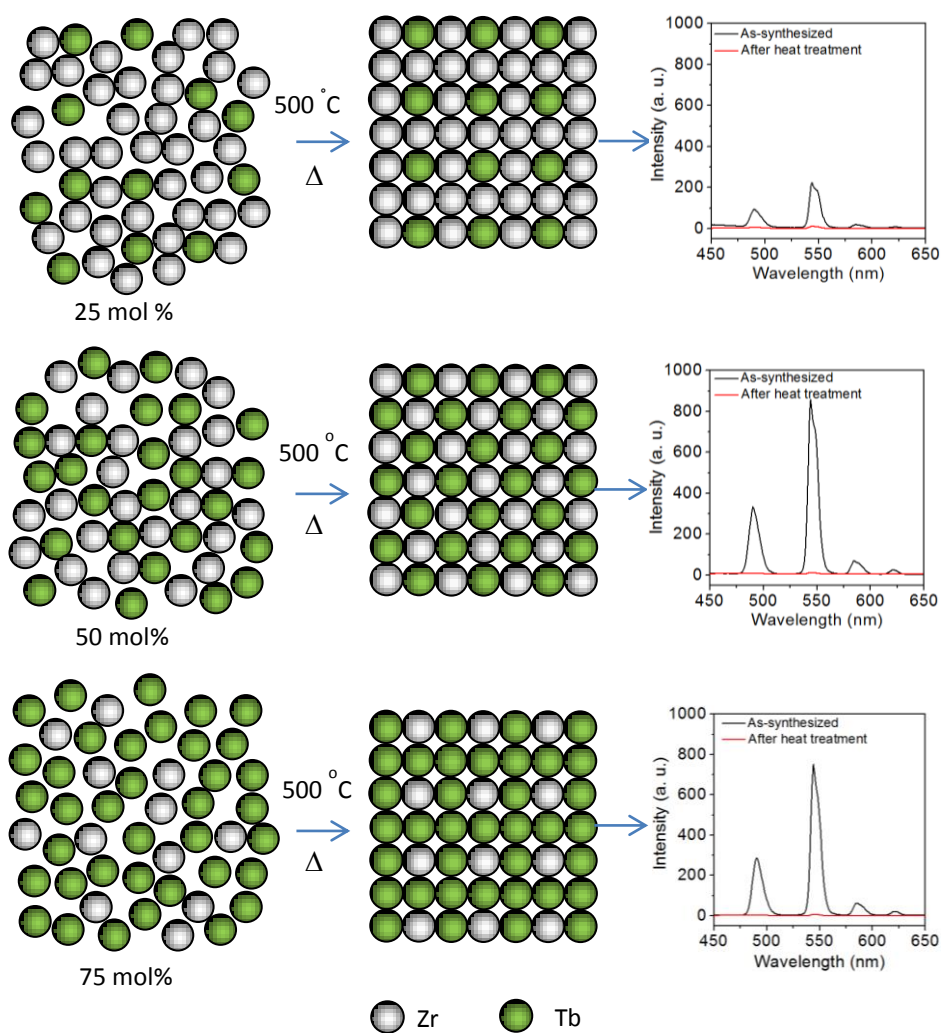


Figure 4.9 Schematic illustration of amorphous (as-synthesized) and crystalline (500 °C) $ZrO_2:Tb^{3+}$ matrix in 25, 50 and 75 mol% of Tb^{3+} in ZrO_2 .

1642 respectively. Similarly, diffraction peaks of 50 mol% $ZrO_2:Tb^{3+}$ can be well assigned to cubic phase which match well with the standard JCPDS file #01-9202. The

plot of 2θ (111) of $\text{ZrO}_2:\text{Tb}^{3+}$ nanoparticles (500 °C) with respect to increasing Tb^{3+} content reveals the diffraction peak position of samples gradually shift to smaller 2θ direction (Figure 4.8D). This is because of the replacement of the larger ionic radius of Tb^{3+} with respect to Zr^{4+} according to Bragg's law. Similarly, the same trend of 2θ reduction with respect to increasing Tb^{3+} content is also observed at 700 °C (Figure 4.8F). The illustration of three different composition (25, 50, 75 mol%) of Zr^{4+} and Tb^{3+} in the $\text{ZrO}_2:\text{Tb}^{3+}$ matrices (Figure 4.9) explains the random order of atoms in amorphous structure in the as-synthesized nanoparticles and the formation of long range order in crystalline structure after annealing at 500 °C. It is believed that the low crystallinity contribute to the superior luminescent properties as evidenced from the PL spectra. It is known that low crystalline structure is a structure that lacks the long range order characteristic of a crystal. Therefore, the lack of the long range order limits the energy transfer between adjacent luminescent and thus minimizing the non radiative energy transfer. On the contrary, the luminescent properties are completely loss in the annealed $\text{ZrO}_2:\text{Tb}^{3+}$ which due to the increase of long range order in crystalline structure that facilitates non radiative energy transfer between adjacent luminescence centers.

4.4 Summary

Highly sensitive pesticides detection was demonstrated for the first time with $\text{ZrO}_2:\text{Tb}^{3+}$ nanoparticles through the quenching of photoluminescence from the f-d transition. This is the first observation that interparticle distance of $\text{ZrO}_2:\text{Tb}^{3+}$ nanoparticles significantly alter their photoluminescence and it is successfully optimized for highly sensitive detection of pesticide down to ppb level. It was found that the electron deficient nitroaromatics are strong quenchers of the luminescent of the $\text{ZrO}_2:\text{Tb}^{3+}$ nanoparticles. The order of sensitivity to pesticides is arranged in the order of nitrobenzene > fenitrothion > paraoxon- ethyl > paraoxon-methyl > carbaryl. Therefore, the extremely high quenching efficiency to the $\text{ZrO}_2:\text{Tb}^{3+}$ luminescence is thus achieved for electron withdrawing analytes which commonly found in pesticides, herbicides, drugs, and industrial waste.

Chapter 5
Rare Earth Metal Oxides for
Bioimaging

5.1 Introduction

RE-incorporated metal oxide nanoparticles is an emerging new class of bioprobes and have attracted tremendous attention for their potential applications in biosensing, bioimaging, and theranostics, owing to their superior physicochemical features such as large Stokes and/or anti-Stokes shifts, narrow emission bands, long luminescence lifetimes, inherent photostability and low toxicity.^{140, 148, 203, 285} The conventional preparation of RE-incorporated metal oxide nanoparticles is through co-precipitation or sol-gel method which require subsequent post annealing to remove OH⁻ groups and/or crystal water molecules attached on the particle surface or in host lattice that may quench the luminescence.^{142, 273, 286} However, the oxide nanoparticles prepared by these methods often result in aggregation which is not desirable for biological applications.¹⁴⁵ Moreover, using the conventional methods, the incorporation level of RE in inorganic matrices remains low of < 5-10 mol%.^{142-145, 152} Beyond this point, the saturation of luminescence occurs which is well attributed to concentration quenching.^{146, 163, 174} Therefore further refinement in the synthetic process is highly important to develop biocompatible RE nanoparticles bioprobes with improved energy efficiency. The long-standing issue is expected to be addressed by effective passivation of more RE emission centers in amorphous metal oxide matrices via a uniform incorporation of RE elements. Full-shelled metal oxides are potentially good matrices because of good insulating properties to effectively localize photo-excited carriers of RE, no efficient self-emission pathways and no internal electron transitions of for causing emission quenching of RE.

In this research, highly luminescent and multicolor RE-incorporated metal oxide nanophosphors were prepared by non-hydrolytic aminolysis process of two metal precursors at high temperature concurrently. A great advantage of this high-temperature wet-chemistry approach over conventional processes is to avoid post-annealing of products at elevated temperatures, which is resulting in bulky size and low suspension ability in aqueous solution. Here, non-crystalline europium-incorporated titanium oxide (TiO₂:Eu³⁺) nanoparticles were prepared with a tunable molar percentage of europium from 0 to 90 mol%, and a drastic incorporation-level increase up to ≥ 50 mol% before self-quenching occurred. More than 65 times of emission enhancement was demonstrated while increasing europium molar percentage from 5 to 50 mol%, and obvious concentration quenching effect only occurred beyond

the value. With the exciting findings, all the chemically/environmentally stable metal oxides with high availability from the periods of 3 to 5 were thus systematically screened as potential matrix candidates to host an increased amount of emission centers for greatly improving emission properties of RE-incorporated metal oxides. As a consequence, a list of different 50 mol% europium-incorporated metal oxides was investigated and their emission intensity under direct ${}^7F_0 \rightarrow {}^5L_6$ excitation of Eu^{3+} was observed with a sequence of $\text{ZrO}_2 > \text{TiO}_2 > \text{SiO}_2$. It was found that $\text{ZrO}_2:\text{Eu}^{3+}$ nanoparticles exhibited high luminescence of 7 and 18 times as strong as the $\text{TiO}_2:\text{Eu}^{3+}$ and the $\text{Y}_2\text{O}_3:\text{Eu}^{3+}$ nanoparticles, respectively.

The effective passivation of various RE elements into non-toxic host matrices including TiO_2 , SiO_2 and ZrO_2 have been thus successfully employed for the first multicolor cellular imaging. In addition to greatly reduced cytotoxicity, these new multicolor bioprobes also presents ultranarrow fixed lines determined by the electronic structure of RE and is almost independent of the host matrix for high reliability biological detection, as compared to quantum dots by varying particle sizes and/or compositions.^{206, 207} For the first time, one of the multi-lines is selectively chosen to emit specific colors upon the direct excitation at well-defined longer wavelength for bio-imaging applications, and the short wavelength excitation only produces multi-lines for causing complexity of bioapplications. Meanwhile, the long-lived fluorescence lifetime also renders them as new generation nanoprobe in time-resolved luminescent biosensing with improved signal-to-noise ratio.²⁸⁵ Overall, the resulting colloidal rare-earth-incorporated metal oxide nanoparticles are also identified here as a promising alternative of prevailing luminescent probes like organic dyes and semiconductor quantum dots as bioprobes/nanotags/nanotags for imaging, sensing, and diagnostics besides lighting applications.

5.2 Experimental section

5.2.1 Materials for nanoparticles synthesis

Titanium(IV) isopropoxide (99%), zirconium(IV) propoxide (70 wt% in 1-propanol), yttrium acetate (99.9%), trimethoxypropyl-silane (98%), europium(III) acetate (99.9%), terbium(III) acetate (99.9%), oleic acid (90%), oleylamine (70%), 1-

octadecene (90%) were purchased from Sigma Aldrich. All reactants and solvents were used as received.

5.2.2 Colloidal synthesis of $\text{TiO}_2:\text{Eu}^{3+}$

All experiments were carried out by standard oxygen-free techniques under argon flow. The synthesis of $\text{TiO}_2:\text{Eu}^{3+}$ nanoparticles were described as an example of various Eu-incorporated metal oxide nanoparticles. In a typical preparation of 50 mol% $\text{TiO}_2:\text{Eu}^{3+}$ nanoparticles, a mixed solution of europium acetate (0.5 mmol), oleic acid (5 mmol), and 1-octadecene (6 mL) was dried and degassed at 90 °C in a 50-mL three-neck flask for 1 h. Then titanium isopropoxide (0.5 mmol) was injected into the mixed solution and heated for 20 min. The solution gradually turned from colorless to a pale yellow, indicating the formation of europium oleate and titanium oleate complexes. Gaseous isopropyl alcohol was rapidly released while the mixture was heated to 290 °C. The aminolysis reaction was then initiated by rapid injection of oleylamine (5 mmol) with vigorous stirring. The resulting solution was kept at 290 °C for 60 minutes. Then the final mixture was allowed to cool to room temperature. The resulting crude solution of $\text{TiO}_2:\text{Eu}^{3+}$ nanoparticles was diluted with hexane (10 mL) followed by precipitation with acetone (20 mL). The crude product was recovered by centrifugation, dispersed in hexane (20 mL), and subjected to a second round of purification. The white powders obtained can be re-dispersed easily in 30 mL hexane for further characterization. A series of $\text{TiO}_2:\text{Eu}^{3+}$ nanoparticles with Eu concentration of 5, 10, 25, 40, 50, 60, 75, and 90 mol% were obtained according to the above synthetic procedure by changing atomic ratio of Eu/Ti while the total amount of Eu^{3+} and Ti^{4+} was kept equal to 1 mmol for their preparation. Other europium-incorporate metal oxide nanoparticles were prepared by the above synthetic procedure by replacing metal precursors with yttrium acetate or trimethoxypropylsilane. Terbium-incorporated metal oxide nanoparticles were also prepared in the same way.

5.2.3 Colloidal synthesis of TiO_2

A mixed solution of oleic acid (5 mmol) in 1-octadecene was dried and degassed at 90 °C in a 50-mL three-neck flask for 1 h. Then titanium (IV) isopropoxide (1.0 mmol) was injected into the mixed solution and heated for 20 min. The aminolysis reaction was then initiated by rapid injection of 5 mmol oleylamine with vigorous stirring. The

resulting solution was kept at 290 °C for 60 minutes. The reaction system were then allowed to cool to room temperature and purified by the same way as above.

5.2.4 Nanoparticles sample preparation for characterisation

TEM images were recorded on a Philips CM 300 FEG transmission electron microscope (300 kV). TEM samples were prepared by depositing a drop of diluted colloidal nanoparticles in hexane on Formvar carbon-coated copper grids and drying in the desiccator. XRD was performed a Siemens D5005 X-ray powder diffractometer. The XRD samples were prepared by dropping the nanoparticle solution onto a silicon (100) wafer and drying at room temperature. Luminescent spectra were measured with a Shimadzu RF-5301 PC fluorometer. Optical spectra in hexane medium were measured with a Shimadzu UV-3150 spectrophotometer. The actual doping concentrations of europium were determined by induced coupled plasma atomic emission spectrometry (ICP-AES) which performed and examined by TÜV SÜD PSB Pte. Ltd.

5.2.5 Materials for PLGA encapsulation and biological experiment

Poly (D,L-lactic-co-glycolic acid) (PLGA) (with L:G molar ratio of 50:50, and Mw of 40-75 k), polyvinyl alcohol (PVA) (Mw 30-70 k), phosphate buffered saline (pH 7.4), DMEM culture medium, penicillin-streptomycin solution, and Trypsin-EDTA solution were purchased from Sigma. Dichloromethane (analytical grade), and fetal bovine serum was received from Merck, Fisher Scientific, and Gibco, respectively. DAPI was from Molecular Probes. All chemicals were used without further process. Double-distilled water was used throughout.

5.2.6 Encapsulation of luminescent nanoparticles with PLGA

After purification, luminescent nanoparticles (~20 mg) were dispersed in dichloromethane and mixed with PLGA (~50 mg) in dichloromethane solution. Encapsulation of nanoparticles in PLGA was further prepared by a modified emulsion-solvent evaporation method by polyvinyl alcohol as an emulsifier. Briefly, the obtained solution (4 mL) of nanoparticles and PLGA was added dropwise into 24 mL aqueous solution of 2 wt% PVA, under magnetic stirring followed by emulsifier for 90 seconds with a homogenizer. Solid PLGA encapsulated particles were successfully obtained by

solvent evaporation of dichloromethane from oil-in-water droplets. The resulting water-dispersible PLGA particles were collected by centrifugation and further washed with water for 3 times to remove excessive emulsifier.

5.2.7 Characterisation for PLGA microparticles

Characterization for PLGA encapsulated microparticles samples: Morphology of PLGA encapsulated microparticles was observed by scanning electron microscope, Jeol JSM 5600LV. The sample was prepared on the metallic stud with double-sided conductive tape and gold-coated by a sputter coater (JFC-1300, Jeol) for 20 s in a vacuum at a current intensity of 40mA. The SEM images were analyzed with SmileView software to determine the average size and size distribution of nanoparticles.

5.2.8 Cell culture

Human breast cancer cells (MCF-7) were obtained from American Type Culture Collection (ATCC) and maintained in DMEM medium supplemented with 10% FBS, 1.0mM sodium pyruvate, 0.1mM non-essential amino acids and 1% penicillin-streptomycin solution.

5.2.9 Cell uptake of PLGA particles in confocal microscopy

To study cell uptake of particles using confocal laser scanning microscopy, cells were seeded at 2.0×10^4 cells cm^{-2} in Lab-Tek chambered cover glasses and cultured as a monolayer at 37 °C in a humidified atmosphere containing 5% CO₂. The cell uptake was started when the culture medium was replaced by particles suspension/dispersion (500 $\mu\text{g mL}^{-1}$ in culture medium) and the monolayer was further incubated for 4 hours at 37 °C. At the end of experiment, the cell monolayer was washed 3 times with fresh pre-warmed phosphate-buffered saline (PBS) buffer to eliminate excess nanoparticles which were not associated to the cells. Cells were then fixed with 70% ethanol. Nucleus staining was carried out using DAPI to facilitate determine the location of the particles inside the cells. The samples were then mounted in the fluorescent mounting medium (Dako). Confocal fluorescent microscopy was performed using an Olympus FV500 system supported with a 60x water-immersion objective and images were processed by FV10-ASW 1.3 Viewer.

5.2.10 Cell cytotoxicity assay

Alamar blue assay was added to MCF-7 cells to test the cytotoxicity of as-prepared products. MCF7 cells were seeded at a density of 2.0×10^4 cells cm^{-2} in 96-well plates (Corning), and incubated with the above solutions for 24 hours at 37 °C in a humidified atmosphere containing 5% CO_2 . After incubation, the viability of the cells was evaluated by alamar blue assay. The reducing environment of viable cells converts the blue resazurin contents of alamar blue assay to highly fluorescent red resorufin that can be measured using 570 nm excitation by Tecan microplate reader. An average of 5 readings was taken for each concentration. The viability is calculated by the fluorescence emission values at 610 nm of treated samples divided by that of control cells without treatment and presented as percentage viability of the control cells.

5.3 Results and discussion

5.3.1 Colloidal synthesis of $\text{TiO}_2:\text{Eu}^{3+}$ nanoparticles

$\text{TiO}_2:\text{Eu}^{3+}$ nanoparticles were prepared with different concentration of Eu^{3+} ranging from ~5 to 90 mol%. The composition of $\text{TiO}_2:\text{Eu}^{3+}$ nanoparticles were analyzed by ICP, revealing the actual Eu^{3+} content ranging from 4.23 (5), 8.24 (10), 26.82 (25), 38.44 (40), 53.27 (50), 56.02 (60), 74.45 (75) and 87.23 (90) mol % in TiO_2 matrices (Table 5.1). These values are very close to the intended doping concentration which described in bracket and hence for the sake of easy recognition, the intended Eu^{3+} concentration will be used for discussion. To have a better understanding of the preparation of $\text{TiO}_2:\text{Eu}^{3+}$ nanoparticles, the scheme of non-hydrolytic approach of 50 mol% of $\text{TiO}_2:\text{Eu}^{3+}$ was illustrated in Figure 5.1A-B. Briefly, equimolar of titanium isopropoxide and europium acetate first reacted with oleic acid to form titanium and europium oleates in a mixed solution, which subsequently aminolyzed at 290 °C with the addition of oleylamine, yielding $\text{TiO}_2:\text{Eu}^{3+}$ nanoparticles of ~2 nm in size (Figure 5.1C).

Table 5.1 Various concentration of Eu^{3+} in TiO_2 with ICP analysis (atomic or molar %).

Number	Starting ratio (Ti/Eu)	Initial Eu concentration	ICP tested ratio (Ti/Eu)	ICP tested Eu concentration
1	0.95/0.05	5%	205/9.06	4.23%
2	0.90/0.10	10%	304/27.3	8.24%
3	0.75/0.25	25%	486/178	26.82%

4	0.60/0.40	40%	90.8/56.7	38.44%
5	0.50/0.50	50%	485/553	53.27%
6	0.40/0.60	60%	292/372	56.02%
7	0.25/0.75	75%	199/580	74.45%
8	0.10/0.90	90%	181/1236	87.23%

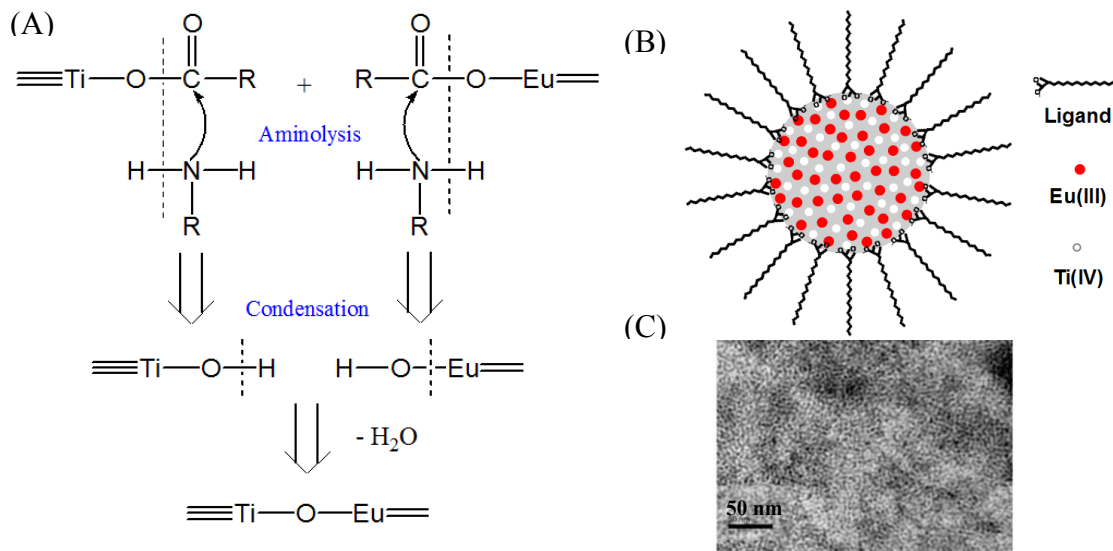


Figure 5.1 (A) Schematic aminolytic synthesis of oleate-coated $\text{TiO}_2:\text{Eu}^{3+}$ nanoparticles at 290 °C through the nucleophilic attack of $-\text{NH}_2$ (oleylamine) to $-\text{C}=\text{O}$ (metal oleates) to form amide. (B) Schematic illustration and (C) TEM image of 50% $\text{TiO}_2:\text{Eu}^{3+}$ nanoparticles.

5.3.2 Optical properties of $\text{TiO}_2:\text{Eu}^{3+}$ nanoparticles

Figure 5.2A shows the comparison of room temperature PL and PL excitation spectra of $\text{TiO}_2:\text{Eu}^{3+}$ nanoparticles. Due to a $^5\text{D}_0-^7\text{F}_2$ transition with europium, it was dominated by the red emission peak at 615 nm. From the shielding effect of 4f electrons by 5s and 5p electrons in outer shells in the europium ion, narrow row emission peaks are expected, consistent with the sharp peaks observed. Under the direct f-f excitation of Eu^{3+} ($^7\text{F}_0-^5\text{L}_6$) at 396 nm, the europium concentration-dependent excitation intensity changed drastically as a function of europium molar content, and the strongest excitation was observed in the 50 mol% $\text{TiO}_2:\text{Eu}^{3+}$ nanoparticles. The corresponding europium concentration-dependent emission of the composition-tunable $\text{TiO}_2:\text{Eu}^{3+}$ nanoparticles was further demonstrated in Figure 5.2B and its inset. The emission intensity increased drastically when europium concentration increased from 5, 10, 25, 40, to 50 mol%. The greatest concentration-enhanced emission by the direct excitation of Eu^{3+} was observed in the 50 mol% $\text{TiO}_2:\text{Eu}^{3+}$ nanoparticles, and it was >65 times as strong as the 5 mol% $\text{TiO}_2:\text{Eu}^{3+}$ nanoparticles while europium content was increased by 10 times. Beyond 50 mol%, the emission intensity started to decrease

until 75 mol%. The obvious concentration-enhanced quenching was much higher than the literature-reported low concentration level of <5-10 mol%. With the further increase of the concentration, it was levelled off. In addition to the direct excitation, europium concentration-dependent excitation at shorter wavelength through Eu^{3+} -to- TiO_2 energy transfer also showed a great intensity change with blue shifted excitation wavelengths from 341 to 320 nm as europium molar content increased from 5 to 90 mol% (Figure 5.1A). The corresponding europium concentration-enhanced emission of the composition-tunable $\text{TiO}_2:\text{Eu}^{3+}$ nanoparticles was demonstrated in Figure 5.1C and inset). The emission intensity increased drastically when europium concentration increased from 5, 10, 25, 40, 50, 60, and 75 mol%; and it started to decrease after further increase of the concentration. The greatest concentration-enhanced emission was observed in the 75 mol% $\text{TiO}_2:\text{Eu}^{3+}$ nanoparticles, and it was >50 times stronger than 5 mol% $\text{TiO}_2:\text{Eu}^{3+}$ nanoparticles while europium content was increased by merely 15 times.

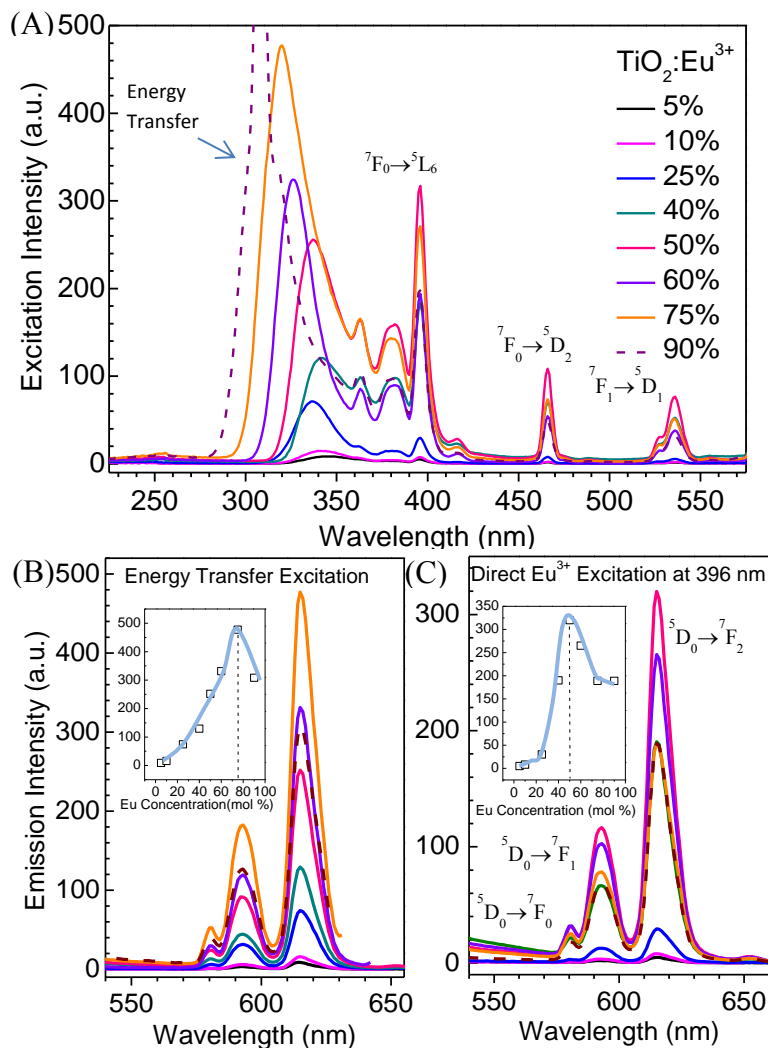


Figure 5.2 Luminescence spectra of $\text{TiO}_2:\text{Eu}^{3+}$ nanoparticles. (A) excitation and (B, C) emission spectra of $\text{TiO}_2:\text{Eu}^{3+}$ nanoparticles with tunable molar percentage ranging from 5, 10, 25, 40, 50, 60, 75, to 90 mol %.(B) Direct excitation at 396 nm from Eu^{3+} emission centers, and inset is the corresponding emission intensity as a function of molar concentration. (C) Energy-transfer excitation at the maximum peaks (341, 341, 341, 341, 337, 333, 326, and 320 nm) for the different concentration-tunable $\text{TiO}_2:\text{Eu}^{3+}$ nanoparticles respectively, and inset is the corresponding emission intensity as a function of molar concentration. The sharp second harmonic emission peak of 95% $\text{TiO}_2:\text{Eu}^{3+}$ nanoparticles cannot be removed by the filters because it has a large overlap with the energy transfer excitation wavelength.

When europium concentration is $\leq 50\%$, Eu^{3+} can just be separated from each other much evenly by Ti^{4+} neighbors in $\text{TiO}_2:\text{Eu}^{3+}$ nanoparticles. The isolated Eu^{3+} is excited individually from ground to excited 4f states directly, and the photo-excited electrons can be localized in insulating matrix at nanoscale followed by relaxing to emissive $^5\text{F}_0$ states and giving off intense light. When europium concentration is increased up to $>50\%$, direct contact between neighboring europium ions causes emission quenching as observed in Figure 5.2B. In addition to relaxation to the emissive $^5\text{F}_0$ states, the photo-excited electrons of Eu^{3+} can migrate to the neighboring europium ions with identical energy levels to quench the emission. It is very understandable that 50% incorporation of europium into TiO_2 matrix can achieve the strongest passivation of Eu_{3+} in matrices to yield the brightest emission of Eu^{3+} under direct excitation in the absence of direct contact of europium atoms.

5.3.3 Structural study of $\text{TiO}_2:\text{Eu}^{3+}$ nanoparticles

The XRD pattern of 50 mol% $\text{TiO}_2:\text{Eu}^{3+}$ and TiO_2 nanoparticles were investigated at different annealing temperatures. The high-temperature nonhydrolytic process led to the very fast formation of amorphous 50 mol% $\text{TiO}_2:\text{Eu}^{3+}$ and TiO_2 nanoparticles with no phase separation as revealed in Figure 5.3A. After 3 hours of annealing at 500 °C, amorphous TiO_2 nanoparticles were transformed into crystalline structure easily; however, the non-crystalline 50% $\text{TiO}_2:\text{Eu}^{3+}$ nanoparticles remained in amorphous structure so as to retain their highly emissive properties (Figure 5.3B). At a higher annealing temperature of 1000 °C, non-crystalline $\text{TiO}_2:\text{Eu}^{3+}$ transformed to crystalline $\text{Eu}_2\text{Ti}_2\text{O}_{11}$ as evidenced by XRD. The high crystallinity structure results in totally non-emissive properties (Figure 5.3B).

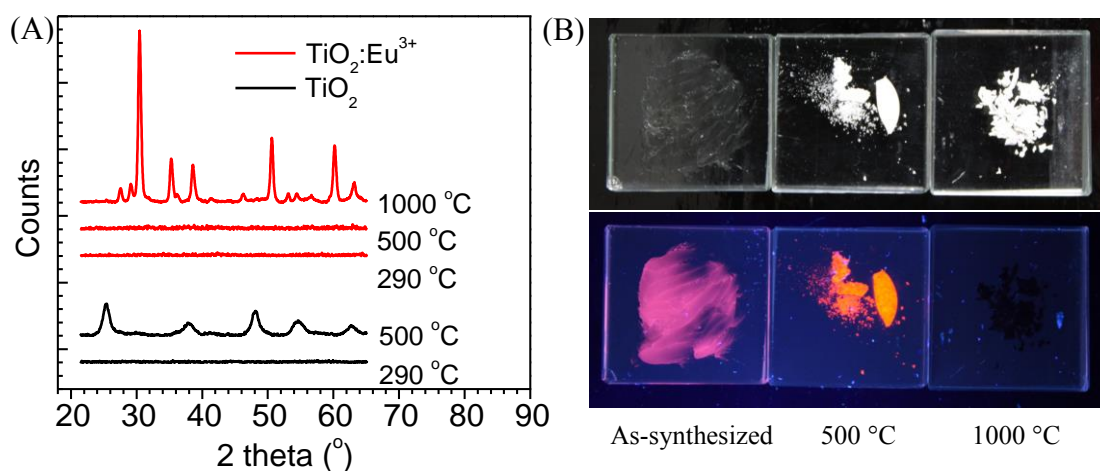


Figure 5.3 (A) XRD analysis of as-synthesized TiO₂ and 50% TiO₂:Eu³⁺ nanoparticles and after annealing at 500 and 1000 °C. (B) Room-light optical (top row) and UV-excited PL (bottom row) images of 50 mol% TiO₂:Eu³⁺ nanoparticles: as synthesized at 290 °C, after annealing at 500 °C and 1000 °C for 3 hours.

5.3.4 Comparative optical properties of TiO₂:Eu³⁺ with ZrO₂:Eu³⁺ and Y₂O₃:Eu³⁺ nanoparticles

The non-hydrolytic preparation of 50 mol% of TiO₂:Eu³⁺ nanoparticles was repeated for ZrO₂:Eu³⁺ and Y₂O₃:Eu³⁺ nanoparticles. Their emission properties were compared with TiO₂:Eu³⁺ nanoparticles as shown in Figure 5.4. The emission of 50 mol% Y₂O₃:Eu³⁺ are only 1/3 as strong as the 50 mol% TiO₂:Eu³⁺ nanoparticles. On the other hand, emission intensity of 50 mol% ZrO₂:Eu³⁺ nanoparticles is 18 times as strong as 50 mol% Y₂O₃:Eu³⁺ nanoparticles. It can be thus revealed that the emission properties of RE emission centers are highly dependent on the surrounding metal oxide matrices. When light is directly absorbed by the trivalent RE metal ions, Eu³⁺ (from ground to excited 4f levels such as ⁷F₀ → ⁵L₆ at 396 nm), the resulting photo-excited electrons of Eu³⁺ are passivated in host metal oxide matrices to enhance the emission properties. When light is indirectly absorbed by the immediate environment of the Eu³⁺ through the hosting matrix, energy is then transferred onto one or several excited states of the Eu³⁺, and finally the Eu³⁺ emits light. The major criteria must be satisfied for the indirect excitation is to have large spectral overlap of the luminescence spectrum of the donor (metal oxide matrices) with the absorption spectrum of the acceptor (Eu³⁺) and strong nonradiative dipole-dipole coupling of the acceptor states of the Eu³⁺ ions to the emissive ⁵D₀ states (⁵D₄ for Tb³⁺).²⁸⁷ For 50 mol% TiO₂:Eu³⁺ nanoparticles, direct excitation of Eu³⁺ take place at longer wavelength (e.g., 396, 535 or 590 nm), and indirect transfer excitation with energy transfer from matrix to Eu³⁺ take places at

shorter wavelength in the narrow range of ~310-360 nm for generating strong emission from $^5D_0 \rightarrow ^7F_1$ at 615 nm. The corresponding excitation energy is much larger than the red emission energy, indicating the energy transfer occurs from the lower energy surface states of nanoparticles to excited 4f states of Eu^{3+} . The strong emission arises from the effective energy transfer from the large number of surface states of ~2 nm $\text{TiO}_2:\text{Eu}^{3+}$ nanoparticles with a large surface-volume ratio of almost 80 % of the metal ions are located at the surface to form the high-density surface states.

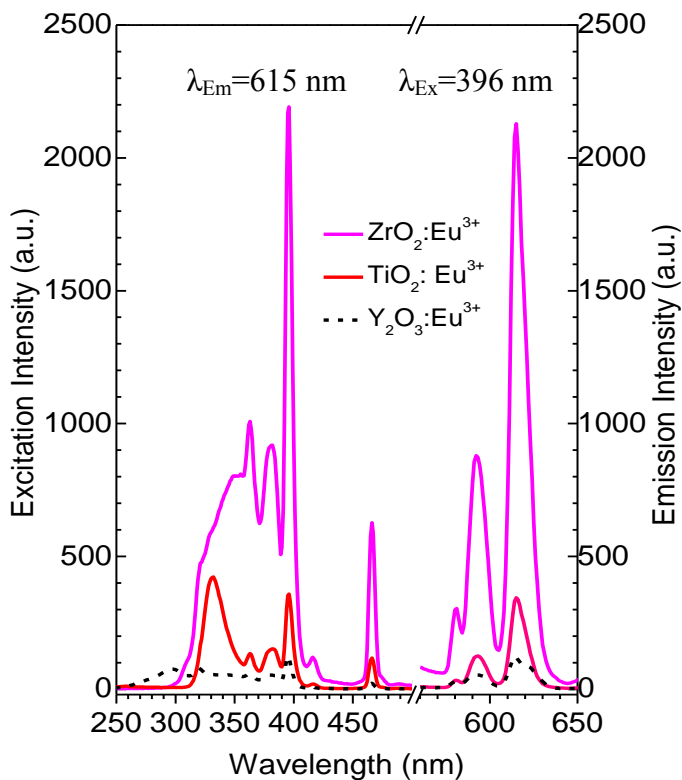


Figure 5.4 Comparative excitation and emission spectra of 50 mol% $\text{TiO}_2:\text{Eu}^{3+}$, $\text{ZrO}_2:\text{Eu}^{3+}$, and $\text{Y}_2\text{O}_3:\text{Eu}^{3+}$ nanoparticles.

When SiO_2 is used to replace TiO_2 as host matrix, energy transfer did not occur to give red color emission. In comparison, ZrO_2 are the best matrix for generating the most intense red emission among the three different matrices. The corresponding excitation wavelengths for the Eu-incorporated TiO_2 , ZrO_2 , and SiO_2 are ~320-360, ~300-360 and ~270-360 nm, respectively with increased excitation energy in the order of $\text{SiO}_2:\text{Eu}^{3+} > \text{TiO}_2:\text{Eu}^{3+} > \text{ZrO}_2:\text{Eu}^{3+}$. The energy transfer of diagram of Eu^{3+} in different host matrices is illustrated in Figure 5.5. First, the europium-incorporated matrix nanoparticles are excited with UV light and after relaxation to their certain sur-

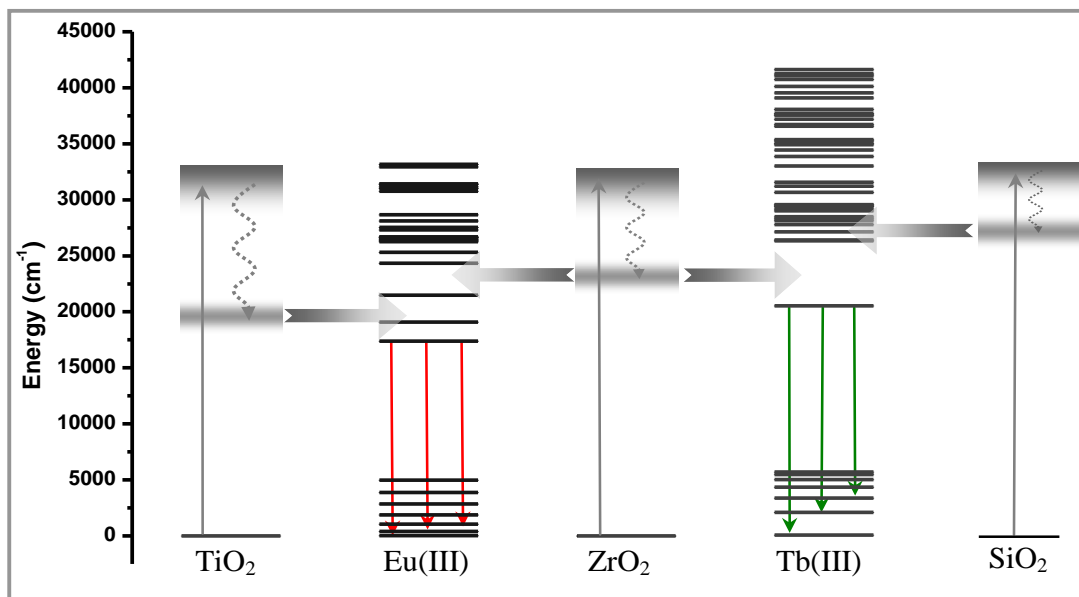


Figure 5.5 Schematic diagram showing the proposed energy transferring mechanism in $\text{TiO}_2:\text{Eu}^{3+}$ nanoparticles: \rightarrow UV photons are absorbed by the TiO_2 band gap; \dashrightarrow non-radiated relaxation to the TiO_2 surface states; \Rightarrow energy transferring to the crystal-field states of Eu^{3+} ions, — which causes the fluorescence. — Emission spectra of 50% $\text{SiO}_2:\text{Tb}^{3+}$ and 50% $\text{ZrO}_2:\text{Tb}^{3+}$ nanoparticles under respective maximum energy transfer excitation at 321 nm and direct excitation of Tb^{3+} ions at 488 nm.

face states, energy transfer occurred from the lower energy surface states of $\text{TiO}_2:\text{Eu}^{3+}$ and $\text{ZrO}_2:\text{Eu}^{3+}$ to the excited 4f states due to the good energy matching of surface states and excited 4f states, resulting in strong luminescence. But energy transfer did not occur effectively from the higher energy surface states of $\text{SiO}_2:\text{Eu}^{3+}$ to the excited 4f states of Eu^{3+} because the large offset between the surface states and the excited emissive states (mismatched energy levels) greatly reduce the energy transfer possibility, resulting in weak luminescence. In comparison with $\text{TiO}_2:\text{Eu}^{3+}$ nanoparticles, the more intense emission of $\text{ZrO}_2:\text{Eu}^{3+}$ nanoparticles arises from a higher surface states than the emissive level in $\text{ZrO}_2:\text{Eu}^{3+}$ so that the energy transfer occurs much efficiently to more excited 4f states due to their larger overlap; when too close, energy transfer is difficult to occur efficiently to less excited 4f states so as to reduce the emission in $\text{TiO}_2:\text{Eu}^{3+}$. This principal has also been further tested using another emission center, Tb^{3+} with higher excited 4f states than Eu^{3+} . As expected, the lower surface states of $\text{TiO}_2:\text{Tb}^{3+}$ cannot cause energy transfer, resulting in no luminescence at all. While, $\text{SiO}_2:\text{Tb}^{3+}$ nanoparticles become luminescent under indirect excitation due to the smaller offset of surface states and excited 4f states. In

comparison, $\text{ZrO}_2:\text{Tb}^{3+}$ nanoparticles are still the most luminescence due to better matched states

5.3.5 Bioimaging of PLGA encapsulated $\text{TiO}_2:\text{Eu}^{3+}$ and $\text{ZrO}_2:\text{Tb}^{3+}$ nanoparticles

The green luminescent $\text{ZrO}_2:\text{Tb}^{3+}$ and red luminescent $\text{TiO}_2:\text{Eu}^{3+}$ nanoparticles (Figure 5.6A) are encapsulated in PLGA via a microemulsion process to render their dispersibility in aqueous solution for bioapplications. SEM image of the as-prepared PLGA encapsulated $\text{ZrO}_2:\text{Tb}^{3+}$ microparticles show uniform capsules of $\sim 1 \mu\text{m}$. (Figure 5.6B). Confocal images of PLGA encapsulated $\text{ZrO}_2:\text{Tb}^{3+}$ (Figure 5.6C) and $\text{TiO}_2:\text{Eu}^{3+}$ (Figure 5.6D) microparticles show luminescent uniform capsules of ~ 1 to 2

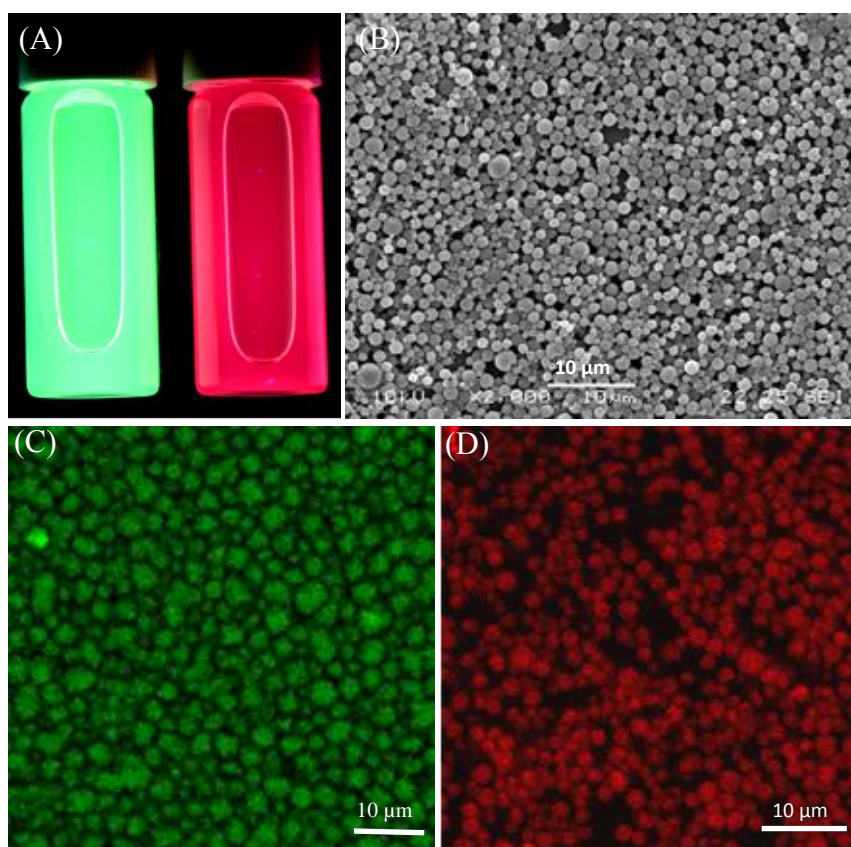


Figure 5.6 (A) Optical photos of $\text{ZrO}_2:\text{Tb}^{3+}$ /green and $\text{TiO}_2:\text{Eu}^{3+}$ /red, nanoparticles in glass vials. (B) SEM image of PLGA encapsulated $\text{ZrO}_2:\text{Tb}^{3+}$ microparticles. (C) Confocal images of PLGA encapsulated $\text{ZrO}_2:\text{Tb}^{3+}$ microparticles and (D) confocal images of PLGA encapsulated $\text{TiO}_2:\text{Eu}^{3+}$ microparticles.

μm . Generally, the cellular permeability and cytotoxicity characteristics of fluorescent nanoparticles are critical to their application as luminescent biological labels. Hence, the potential applicability of the red luminescent $\text{TiO}_2:\text{Eu}^{3+}$ and green luminescent $\text{ZrO}_2:\text{Tb}^{3+}$ nanoparticles in a biological system is confirmed by conducting analogous

experiments using MCF-7 cells. As a control experiment, MCF-7 cells alone showed negligible background fluorescence under laser 488 nm excitation. Nonetheless, upon incubation, incorporation of PLGA encapsulated $\text{TiO}_2:\text{Eu}^{3+}$ and $\text{ZrO}_2:\text{Tb}^{3+}$ microparticles into MCF-7 cells were confirmed by confocal fluorescence microscopy. Specifically, after incubation with $150 \mu\text{g mL}^{-1}$ of $\text{ZrO}_2:\text{Tb}^{3+}$ nanoparticles for 2 hours at 37°C , an intense intracellular luminescence was observed, as shown in Figure 5.7. These RE nanoparticles clearly retained their intrinsic fluorescent properties upon cellular internalization.

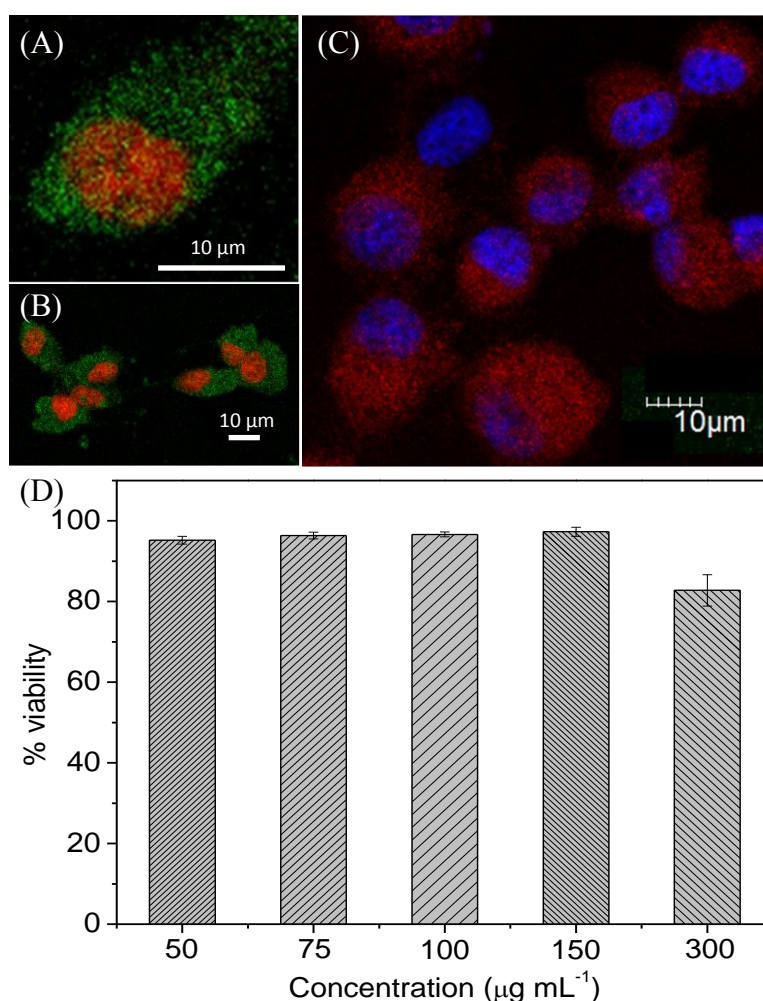


Figure 5.7 (A-C) Cellular imaging, (A-B) $\text{ZrO}_2:\text{Tb}^{3+}$, (C) $\text{TiO}_2:\text{Eu}^{3+}$ counterstained with dye molecules. (D) In vitro cell viability of MCF-7 cells incubated with PLGA encapsulated $\text{ZrO}_2:\text{Tb}^{3+}$ microparticles at different concentrations for periods of 24 hours.

To verify whether these PLGA encapsulated $\text{ZrO}_2:\text{Tb}^{3+}$ microparticles are nontoxic and biocompatible, cytotoxicity studies of MCF-7 were performed using alamar blue assay as shown in Figure 5.7. The viability of untreated cells was assumed to be 100%. Upon

incubation of MCF-7 cells with a $50 \mu\text{g mL}^{-1}$ solution of PLGA encapsulated $\text{ZrO}_2:\text{Tb}^{3+}$ microparticles, there are fewer than 10% of the cells died after 24. When the concentration of PLGA encapsulated $\text{ZrO}_2:\text{Tb}^{3+}$ microparticles was increased to $300 \mu\text{g mL}^{-1}$, the observed cell viability still remained above 80% after 24 h incubation. Therefore, these data strongly suggested that PLGA encapsulated $\text{ZrO}_2:\text{Tb}^{3+}$ microparticles to possess reasonably low cytotoxicity which are essential for bioimaging applications.

5.4 Summary

The passivation of trivalent europium in various metal oxides including TiO_2 , ZrO_2 , SiO_2 , Y_2O_3 have been synthesized with high incorporation concentration of up to 50 mol% before concentration quenching. In particular, the strong luminescence in $\text{TiO}_2:\text{Eu}^{3+}$ is facilitated by the energy matching of the surface states of the metal oxide hosts and the excited 4f state of europium, resulting in energy transfer induced luminescence enhancement. The $\text{TiO}_2:\text{Eu}^{3+}$ nanoparticles with high photostability and low cytotoxicity were readily encapsulated by PLGA to exhibit strong luminescent for cellular imaging, and it is believed that they are promising to be the next generation bioprobes in bioapplications.

Chapter 6

Conclusions and Outlook

6.1 Conclusions

In this dissertation, we have successfully fabricated various metals, bimetallic and RE-incorporated metal oxides in well-defined nanostructures for bioapplications. First, the anisotropic growth of Cu nanowires and Cu/Au nanotubes was employed in non-enzymatic glucose sensing. The incorporation of Au in Cu nanowires template at appropriate reaction temperature yielded the hollow Cu/Au nanotubes which improve the sensitivity of glucose sensing. The amount of Au doping into Cu nanostructures controlled the final nanostructures from solid nanowires, porous nanowires to hollow nanotubes. The Cu/Au nanotubes improved the overall catalytic performance in glucose sensing due to the increase in surface area compare to their solid counterparts. In addition, elevated reaction temperature destroyed the anisotropic growth of nanowires leading to irregular shaped nanoparticles resulting in poor sensing performance.

We have also prepared RE-incorporated metal oxides with various composition and combination of RE in metal oxides matrices. This includes $\text{ZrO}_2:\text{Tb}^{3+}$, $\text{SiO}_2:\text{Tb}^{3+}$, $\text{ZrO}_2:\text{Eu}^{3+}$, $\text{TiO}_2:\text{Eu}^{3+}$, and $\text{SiO}_2:\text{Eu}^{3+}$. Among all, 50 mol% $\text{ZrO}_2:\text{Tb}^{3+}$, $\text{ZrO}_2:\text{Eu}^{3+}$ and $\text{TiO}_2:\text{Eu}^{3+}$ exhibited the highest luminescence partially attributed to the effective energy transfer from the metal oxides host to RE emission centers. More importantly, the amorphous nanostructures prevent the non-radiative energy transfer among the emission centers and thus improved the overall emission. The small nanoparticles of 2 nm with large surface-to-volume ratio comprised of 80 % of atoms on the surface which is highly desirable in most applications. The highly luminescent $\text{ZrO}_2:\text{Tb}^{3+}$ nanoparticles are employed in pesticides sensing through the luminescent quenching of the f-d band of terbium. Particularly, the electron deficient nitroaromatics are strong quenchers of the luminescence of the $\text{ZrO}_2:\text{Tb}^{3+}$ nanoparticles achieving the detection limit of ppm and ppb level. While the highly luminescent $\text{ZrO}_2:\text{Tb}^{3+}$ and $\text{TiO}_2:\text{Eu}^{3+}$ nanoparticles were customized for bioapplication upon encapsulation with PLGA to render their dispersibility in aqueous solution. The potential applicability of the red luminescent $\text{TiO}_2:\text{Eu}^{3+}$ and green luminescent $\text{ZrO}_2:\text{Tb}^{3+}$ nanoparticles in bioimaging were confirmed by incubation with MCF-7 cells under confocal fluorescence microscopy. The intense intracellular luminescence was observed which clearly proved that the intrinsic fluorescent properties of RE were retained upon cellular

internalization. Overall, the exciting findings together with the low cytotoxicity, the RE-incorporated metal oxides are particularly beneficial as an alternative of prevailing luminescent probes like organic dyes and semiconductors as bioprobes for imaging, sensing and diagnostics applications.

6.2 Outlook

The use of colloidal synthesis techniques to develop functional nanostructures for tuning their properties will continue to play a vital role in improving the current technologies and discovering new applications. The research and finding of this dissertation elaborated on the general colloidal synthesis to fabricate various new and functional nanostructures for bioapplications. Future progress in this area hinges on improving the current fabrication techniques to generate more functional nanostructures to improve their usefulness for a given application. These nanostructures are not limited to transition metals, noble metals, bimetallic, transition metal oxides and RE metal oxides. For instance, the current fabrication techniques of bimetallic Cu/Au from Cu nanowire template can be applied for other hybrid transition and noble metals such as Cu/Pt and Cu/Pd nanostructures. The precise control of the morphology and composition of these nanostructures will undoubtedly offer the opportunity to reduce the cost of noble metals and improve the performance of noble metal-based nanostructures in applications such as non-enzymatic glucose sensor and automotive catalytic converters.

On the other hand, the fabrication of RE incorporated metal oxides can be further investigated by systematically screen the potential metal oxide host matrices in the elements of periods from 3 to 5 including s-(I, II), p-(III, VI), and d-block (transition metals) to improve the emission properties. Therefore, there will be more opportunities to exploit new individual properties as well as improving the existing technologies in commercial optical-based applications (i.e., lighting, display, lasing) and even biomedical application (i.e., bioimaging, magnetic resonance imaging, targeted drug delivery). Certainly, the development of novel nanostructures with tailored properties will produce more innovation that benefits industries and society.

References

1. P. K. Jain, X. Huang, I. H. El-Sayed and M. A. El-Sayed, *Acc. Chem. Res.*, 2008, **41**, 1578.
2. H. M. Chen and R.-S. Liu, *J. Phys. Chem. C*, 2011, **115**, 3513.
3. E. C. Dreaden, A. M. Alkilany, X. Huang, C. J. Murphy and M. A. El-Sayed, *Chem. Soc. Rev.*, 2012, **41**, 2740.
4. S. E. Lohse and C. J. Murphy, *J. Am. Chem. Soc.*, 2012, **134**, 15607.
5. C. N. Rao, H. S. Ramakrishna Matte, R. Voggu and A. Govindaraj, *Dalton Trans.*, 2012, **41**, 5089.
6. Q. Kuang, X. Wang, Z. Jiang, Z. Xie and L. Zheng, *Acc. Chem. Res.*, 2014, **47**, 308.
7. Y. Xia, Y. Xiong, B. Lim and S. E. Skrabalak, *Angew. Chem. Int. Ed.*, 2009, **48**, 60.
8. C. Y. Chiu, Y. Li, L. Ruan, X. Ye, C. B. Murray and Y. Huang, *Nat. Chem.*, 2011, **3**, 393.
9. H. Zhang, M. Jin and Y. Xia, *Angew. Chem. Int. Ed.*, 2012, **51**, 7656.
10. Z. Qian and S.-J. Park, *Chem. Mater.*, 2014, **26**, 6172.
11. K. Zhou and Y. Li, *Angew. Chem. Int. Ed.*, 2012, **51**, 602.
12. Z. Y. Zhou, N. Tian, J. T. Li, I. Broadwell and S. G. Sun, *Chem. Soc. Rev.*, 2011, **40**, 4167.
13. M. Faraday, *Philos. Trans. R. Soc. Lond.*, 1857, **147**, 145.
14. W. Stober and A. Fink, *J. Colloid Interface Sci.*, 1968, **26**, 62.
15. B. V. Enüstün and J. Turkevich, *J. Am. Chem. Soc.*, 1963, **85**, 3317.
16. P. Berger, *J. Chem. Educ.*, 1999, **76**, 943.
17. R. D. Glover, J. M. Miller and J. E. Hutchison, *ACS Nano*, 2011, **5**, 8950.
18. Z. M. Xiu, Q. B. Zhang, H. L. Puppala, V. L. Colvin and P. J. Alvarez, *Nano Lett.*, 2012, **12**, 4271.
19. J. A. Dahl, B. L. Maddux and J. E. Hutchison, *Chem Rev*, 2007, **107**, 2228.
20. S.-Y. Zhang, M. D. Regulacio, K. W. Shah, T. Sreethawong, Y. Zheng and M.-Y. Han, *J. Mol. Eng. Mater.*, 2014, **02**, 1430001.
21. Y. Xia, Y. Xiong, B. Lim and S. E. Skrabalak, *Angew. Chem. Int. Ed.*, 2009, **48**, 60.
22. K. Zhou and Y. Li, *Angew. Chem. Int. Ed.*, 2012, **51**, 602.
23. P. D. Cozzoli, T. Pellegrino and L. Manna, *Chem. Soc. Rev.*, 2006, **35**, 1195.
24. R. Costi, A. E. Saunders and U. Banin, *Angew. Chem. Int. Ed.*, 2010, **49**, 4878.
25. I. Lisiecki, F. Billoudet and M. P. Pileni, *J. Phys. Chem.*, 1996, **100**, 4160.
26. B. K. Park, S. Jeong, D. Kim, J. Moon, S. Lim and J. S. Kim, *J. Colloid Interface Sci.*, 2007, **311**, 417.
27. C. M. Welch and R. G. Compton, *Anal. Bioanal. Chem.*, 2006, **384**, 601.
28. P. Si, Y. Huang, T. Wang and J. Ma, *RSC Adv.*, 2013, **3**, 3487.
29. E. Ye, S. Y. Zhang, S. Liu and M. Y. Han, *Chem. Eur. J.*, 2011, **17**, 3074.
30. H. Guo, Y. Chen, M. B. Cortie, X. Liu, Q. Xie, X. Wang and D.-L. Peng, *J. Phys. Chem. C*, 2014, **118**, 9801.
31. X. Huang, Y. Chen, C. Y. Chiu, H. Zhang, Y. Xu, X. Duan and Y. Huang, *Nanoscale*, 2013, **5**, 6284.
32. N. George, J. Faoagali and M. Muller, *Burns*, 1997, **23**, 493.
33. B. S. Atiyeh, M. Costagliola, S. N. Hayek and S. A. Dibo, *Burns*, 2007, **33**, 139.
34. C. Chen, L. Wang, H. Yu, J. Wang, J. Zhou, Q. Tan and L. Deng, *Nanotechnology*, 2007, **18**, 115612.
35. J. Zhang, M. R. Langille and C. A. Mirkin, *J. Am. Chem. Soc.*, 2010, **132**, 12502.
36. K. M. M. Abou El-Nour, A. a. Eftaiha, A. Al-Warthan and R. A. A. Ammar, *Arabian J. Chem.*, 2010, **3**, 135.
37. Z. Huang, X. Jiang, D. Guo and N. Gu, *J. Nanosci. Nanotechnol.*, 2011, **11**, 9395.
38. Y.-H. Chen and C.-S. Yeh, *Colloid Surf. A*, 2002, **197**, 133.
39. B. Wiley, Y. Sun, B. Mayers and Y. Xia, *Chemistry*, 2005, **11**, 454.
40. R. Jin, *Nanoscale*, 2010, **2**, 343.

41. J. Xiao and L. Qi, *Nanoscale*, 2011, **3**, 1383.
42. A. Henglein and M. Giersig, *J. Phys. Chem. B*, 1999, **103**, 9533.
43. L. Qu, G. Shi, X. Wu and B. Fan, *Adv. Mater.*, 2004, **16**, 1200.
44. J. Q. Hu, Q. Chen, Z. X. Xie, G. B. Han, R. H. Wang, B. Ren, Y. Zhang, Z. L. Yang and Z. Q. Tian, *Adv. Funct. Mater.*, 2004, **14**, 183.
45. S. H. Zhang, Z. X. Xie, Z. Y. Jiang, X. Xu, J. Xiang, R. B. Huang and L. S. Zheng, *Chem. Commun.*, 2004, DOI: 10.1039/b315931k, 1106.
46. D. Yu and V. W. Yam, *J. Am. Chem. Soc.*, 2004, **126**, 13200.
47. B. Pietrobon and V. Kitaev, *Chem. Mater.*, 2008, **20**, 5186.
48. B.-H. Lee, M.-S. Hsu, Y.-C. Hsu, C.-W. Lo and C.-L. Huang, *J. Phys. Chem. C*, 2010, **114**, 6222.
49. X. He, X. Zhao, Y. Li and X. Sui, *J. Mater. Res.*, 2011, **24**, 2200.
50. I. Pastoriza-Santos and L. M. Liz-Marzán, *Nano Lett.*, 2002, **2**, 903.
51. M. Haruta, *Nature*, 2005, **437**, 1098.
52. H. Tsunoyama, H. Sakurai, Y. Negishi and T. Tsukuda, *J. Am. Chem. Soc.*, 2005, **127**, 9374.
53. L. Y. Chen, C. W. Wang, Z. Yuan and H. T. Chang, *Anal. Chem.*, 2015, **87**, 216.
54. Y. Liu, K. Ai, X. Cheng, L. Huo and L. Lu, *Adv. Funct. Mater.*, 2010, **20**, 951.
55. R. Zsigmondy, *The Chemistry of colloids*, John Wiley, New York, 1917.
56. N. R. Jana, L. Gearheart and C. J. Murphy, *J. Phys. Chem. B*, 2001, **105**, 4065.
57. C. J. Murphy, T. K. Sau, A. M. Gole, C. J. Orendorff, J. Gao, L. Gou, S. E. Hunyadi and T. Li, *J. Phys. Chem. B*, 2005, **109**, 13857.
58. T. H. Ha, H.-J. Koo and B. H. Chung, *J. Phys. Chem. C*, 2007, **111**, 1123.
59. J. E. Millstone, S. Park, K. L. Shuford, L. Qin, G. C. Schatz and C. A. Mirkin, *J. Am. Chem. Soc.*, 2005, **127**, 5312.
60. P. K. Jain, K. S. Lee, I. H. El-Sayed and M. A. El-Sayed, *J. Phys. Chem. B*, 2006, **110**, 7238.
61. A. C. Templeton, J. J. Pietron, R. W. Murray and P. Mulvaney, *J. Phys. Chem. B*, 2000, **104**, 564.
62. K. H. Su, Q. H. Wei, X. Zhang, J. J. Mock, D. R. Smith and S. Schultz, *Nano Lett.*, 2003, **3**, 1087.
63. T. Naota, H. Takaya and S.-I. Murahashi, *Chem. Rev.*, 1998, **98**, 2599.
64. T. Mallat and A. Baiker, *Chem Rev*, 2004, **104**, 3037.
65. K. Honkala, A. Hellman, I. N. Remediakis, A. Logadottir, A. Carlsson, S. Dahl, C. H. Christensen and J. K. Nørskov, *Science*, 2005, **307**, 555.
66. H. Over, *Science*, 2000, **287**, 1474.
67. E. Tsuji, A. Imanishi, K.-i. Fukui and Y. Nakato, *Electrochim. Acta*, 2011, **56**, 2009.
68. A. X. Yin, W. C. Liu, J. Ke, W. Zhu, J. Gu, Y. W. Zhang and C. H. Yan, *J. Am. Chem. Soc.*, 2012, **134**, 20479.
69. H. Over, *Chem Rev*, 2012, **112**, 3356.
70. G. Viau, R. Brayner, L. Poul, N. Chakroune, E. Lacaze, F. Fiévet-Vincent and F. Fiévet, *Chem. Mater.*, 2003, **15**, 486.
71. Y. Lee, J. Suntivich, K. J. May, E. E. Perry and Y. Shao-Horn, *J. Phys. Chem. Lett.*, 2012, **3**, 399.
72. L. Au, Y. Chen, F. Zhou, P. H. Camargo, B. Lim, Z. Y. Li, D. S. Ginger and Y. Xia, *Nano Res.*, 2008, **1**, 441.
73. C. L. Braceley, P. R. Ellis and G. J. Hutchings, *Chem. Soc. Rev.*, 2009, **38**, 2231.
74. J. Yang, X. Chen, X. Yang and J. Y. Ying, *Energy Environ. Sci.*, 2012, **5**, 8976.
75. G. Guisbiers, S. Mejia-Rosales, S. Khanal, F. Ruiz-Zepeda, R. L. Whetten and M. Jose-Yacaman, *Nano Lett.*, 2014, **14**, 6718.
76. J. Zhang, Y. Tang, L. Weng and M. Ouyang, *Nano Lett.*, 2009, **9**, 4061.

77. Z. W. Seh, S. Liu, S. Y. Zhang, K. W. Shah and M. Y. Han, *Chem. Commun.*, 2011, **47**, 6689.
78. Z. Peng and H. Yang, *J. Am. Chem. Soc.*, 2009, **131**, 7542.
79. D. Wang and Y. Li, *J. Am. Chem. Soc.*, 2010, **132**, 6280.
80. M. Chen, D. Kumar, C. W. Yi and D. W. Goodman, *Science*, 2005, **310**, 291.
81. D. Y. Wang, H. L. Chou, Y. C. Lin, F. J. Lai, C. H. Chen, J. F. Lee, B. J. Hwang and C. C. Chen, *J. Am. Chem. Soc.*, 2012, **134**, 10011.
82. Y. Jiang, Y. Lu, D. Han, Q. Zhang and L. Niu, *Nanotechnology*, 2012, **23**, 105609.
83. H. M. Chen, C. F. Hsin, P. Y. Chen, R. S. Liu, S. F. Hu, C. Y. Huang, J. F. Lee and L. Y. Jang, *J. Am. Chem. Soc.*, 2009, **131**, 15794.
84. C. Zhu, S. Guo and S. Dong, *Adv. Mater.*, 2012, **24**, 2326.
85. S. J. Hurst, E. K. Payne, L. Qin and C. A. Mirkin, *Angew. Chem. Int. Ed.*, 2006, **45**, 2672.
86. W. Wei, S. Li, J. E. Millstone, M. J. Banholzer, X. Chen, X. Xu, G. C. Schatz and C. A. Mirkin, *Angew. Chem. Int. Ed.*, 2009, **48**, 4210.
87. S. Duan and R. Wang, *Prog. Nat. Sci.*, 2013, **23**, 113.
88. C. C. Koch, *Nanostruct. Mater.*, 1997, **9**, 13.
89. C. Suryanarayana, E. Ivanov and V. V. Boldyrev, *Mater. Sci. Eng., A*, 2001, **304-306**, 151.
90. D. V. Goia and E. Matijević, *New J. Chem.*, 1998, **22**, 1203.
91. H. Bönemann and Ryan M. Richards, *Eur. J. Inorg. Chem.*, 2001, **2001**, 2455.
92. C. Burda, X. Chen, R. Narayanan and M. A. El-Sayed, *Chem Rev*, 2005, **105**, 1025.
93. R. Ferrando, J. Jellinek and R. L. Johnston, *Chem Rev*, 2008, **108**, 845.
94. S. E. Skrabalak, J. Chen, Y. Sun, X. Lu, L. Au, C. M. Copley and Y. Xia, *Acc. Chem. Res.*, 2008, **41**, 1587.
95. B. Goris, L. Polavarapu, S. Bals, G. Van Tendeloo and L. M. Liz-Marzan, *Nano Lett.*, 2014, **14**, 3220.
96. Y. Sun and Y. Xia, *J. Am. Chem. Soc.*, 2004, **126**, 3892.
97. X. Lu, L. Au, J. McLellan, Z. Y. Li, M. Marquez and Y. Xia, *Nano Lett.*, 2007, **7**, 1764.
98. S. E. Habas, H. Lee, V. Radmilovic, G. A. Somorjai and P. Yang, *Nat. Mater.*, 2007, **6**, 692.
99. W. Chen, R. Yu, L. Li, A. Wang, Q. Peng and Y. Li, *Angew. Chem. Int. Ed.*, 2010, **49**, 2917.
100. M. Mohl, D. Dobo, A. Kukovecz, Z. Konya, K. Kordas, J. Wei, R. Vajtai and P. M. Ajayan, *J. Phys. Chem. C*, 2011, **115**, 9403.
101. A. Fujishima and K. Honda, *Nature*, 1972, **238**, 37.
102. S. Wu, Z. Weng, X. Liu, K. W. K. Yeung and P. K. Chu, *Adv. Funct. Mater.*, 2014, **24**, 5464.
103. X. Wang, Z. Li, J. Shi and Y. Yu, *Chem Rev*, 2014, **114**, 9346.
104. E. Roduner, *Chem. Soc. Rev.*, 2006, **35**, 583.
105. M. Valden, *Science*, 1998, **281**, 1647.
106. X. Chen and S. S. Mao, *Chem Rev*, 2007, **107**, 2891.
107. J. Lin, Y. U. Heo, A. Nattestad, Z. Sun, L. Wang, J. H. Kim and S. X. Dou, *Sci. Rep.*, 2014, **4**, 5769.
108. G. Melcarne, L. De Marco, E. Carlino, F. Martina, M. Manca, R. Cingolani, G. Gigli and G. Ciccarella, *J. Mater. Chem.*, 2010, **20**, 7248.
109. Z. Zhang, X. Zhong, S. Liu, D. Li and M. Han, *Angew. Chem. Int. Ed.*, 2005, **44**, 3466.
110. R. M. Cornell and U. Schwertmann, *The Iron Oxides: Structure, Properties, Reactions, Occurrences and Uses*, Wiley-VCH, Weinheim, 2 edn., 2003.
111. W. Wu, Q. He and C. Jiang, *Nanoscale Res. Lett.*, 2008, **3**, 397.
112. S. Laurent, D. Forge, M. Port, A. Roch, C. Robic, L. Vander Elst and R. N. Muller, *Chem Rev*, 2008, **108**, 2064.

113. W. Wu, Z. Wu, T. Yu, C. Jiang and W.-S. Kim, *Sci. Technol. Adv. Mater.*, 2015, **16**, 023501.
114. R. Massart, *IEEE Trans. Magn.*, 1981, **17**, 1247.
115. T. Ahn, J. H. Kim, H.-M. Yang, J. W. Lee and J.-D. Kim, *J. Phys. Chem. C*, 2012, **116**, 6069.
116. S. Sun and H. Zeng, *J. Am. Chem. Soc.*, 2002, **124**, 8204.
117. Z. Li, B. Tan, M. Allix, A. I. Cooper and M. J. Rosseinsky, *Small*, 2008, **4**, 231.
118. J. Park, K. An, Y. Hwang, J. G. Park, H. J. Noh, J. Y. Kim, J. H. Park, N. M. Hwang and T. Hyeon, *Nat. Mater.*, 2004, **3**, 891.
119. S. Palchoudhury, W. An, Y. Xu, Y. Qin, Z. Zhang, N. Chopra, R. A. Holler, C. H. Turner and Y. Bao, *Nano Lett.*, 2011, **11**, 1141.
120. Z. Zhou, X. Zhu, D. Wu, Q. Chen, D. Huang, C. Sun, J. Xin, K. Ni and J. Gao, *Chem. Mater.*, 2015, **27**, 3505.
121. C. J. Jia, L. D. Sun, Z. G. Yan, Y. C. Pang, L. P. You and C. H. Yan, *J. Phys. Chem. C*, 2007, **111**, 13022.
122. T. Oku, R. Motoyoshi, K. Fujimoto, T. Akiyama, B. Jeyadevan and J. Cuya, *J. Phys. Chem. Solids*, 2011, **72**, 1206.
123. A. Bhaumik, A. Haque, P. Karnati, M. F. N. Taufique, R. Patel and K. Ghosh, *Thin Solid Films*, 2014, **572**, 126.
124. M. M. Rahman, A. J. Ahammad, J. H. Jin, S. J. Ahn and J. J. Lee, *Sensors*, 2010, **10**, 4855.
125. W. Chen, S. Cai, Q. Q. Ren, W. Wen and Y. D. Zhao, *The Analyst*, 2012, **137**, 49.
126. J. Y. Ji, P. H. Shih, C. C. Yang, T. S. Chan, Y. R. Ma and S. Y. Wu, *Nanotechnology*, 2010, **21**, 045603.
127. X. Jiang, T. Herricks and Y. Xia, *Nano Lett.*, 2002, **2**, 1333.
128. C. Lu, L. Qi, J. Yang, D. Zhang, N. Wu and J. Ma, *J. Phys. Chem. B*, 2004, **108**, 17825.
129. Y. Zhao, J.-J. Zhu, J.-M. Hong, N. Bian and H.-Y. Chen, *Eur. J. Inorg. Chem.*, 2004, **2004**, 4072.
130. H. Hou, Y. Xie and Q. Li, *Cryst. Growth Des.*, 2005, **5**, 201.
131. G. Filipic and U. Cvelbar, *Nanotechnology*, 2012, **23**, 194001.
132. W. Z. Wang, G. H. Wang, X. S. Wang, Y. J. Zhan, Y. K. Liu and C. L. Zheng, *Adv. Mater.*, 2002, **14**, 67.
133. Y. Li, X. Y. Yang, J. Rooke, G. Van Tendeloo and B. L. Su, *J. Colloid Interface Sci.*, 2010, **348**, 303.
134. K. Binnemans, *Chem Rev*, 2009, **109**, 4283.
135. R. Si, Y. W. Zhang, L. P. You and C. H. Yan, *Angew. Chem. Int. Ed.*, 2005, **44**, 3256.
136. R. Si, Y.-W. Zhang, H.-P. Zhou, L.-D. Sun and C.-H. Yan, *Chem. Mater.*, 2007, **19**, 18.
137. J. Paek, C. H. Lee, J. Choi, S.-Y. Choi, A. Kim, J. W. Lee and K. Lee, *Cryst. Growth Des.*, 2007, **7**, 1378.
138. M. Han, N. E. Shi, W. L. Zhang, B. J. Li, J. H. Sun, K. J. Chen, J. M. Zhu, X. Wang and Z. Xu, *Chemistry*, 2008, **14**, 1615.
139. E. G. Moore, A. P. Samuel and K. N. Raymond, *Acc. Chem. Res.*, 2009, **42**, 542.
140. S. Gai, C. Li, P. Yang and J. Lin, *Chem Rev*, 2014, **114**, 2343.
141. J. Wang, Y. Cheng, Y. Huang, P. Cai, S. I. Kim and H. J. Seo, *J. Mater. Chem. C*, 2014, **2**, 5559.
142. Y. Liu, W. Luo, R. Li and X. Chen, *Opt. Lett.*, 2007, **32**, 566.
143. Y. Liu, W. Luo, R. Li, G. Liu, M. R. Antonio and X. Chen, *J. Phys. Chem. C*, 2008, **112**, 686.
144. L. Luo, F. Y. Huang, G. S. Dong, H. H. Fan, K. F. Li, K. W. Cheah and J. Chen, *Opt. Mater.*, 2014, **37**, 470.
145. W. Luo, R. Li, G. Liu, M. R. Antonio and X. Chen, *J. Phys. Chem. C*, 2008, **112**, 10370.

146. H. Li, Y. Sheng, H. Zhang, J. Xue, K. Zheng, Q. Huo and H. Zou, *Powder Technol.*, 2011, **212**, 372.
147. H. Li, Y. Sheng, H. Zhao, Y. Song, F. Gao, Q. Huo and H. Zou, *Mater. Res. Bull.*, 2012, **47**, 4322.
148. Y. Liu, S. Zhou, D. Tu, Z. Chen, M. Huang, H. Zhu, E. Ma and X. Chen, *J. Am. Chem. Soc.*, 2012, **134**, 15083.
149. J. Shen, L.-D. Sun, J.-D. Zhu, L.-H. Wei, H.-F. Sun and C.-H. Yan, *Adv. Funct. Mater.*, 2010, **20**, 3708.
150. X. Wang, J. Zhuang, Q. Peng and Y. Li, *Inorg. Chem.*, 2006, **45**, 6661.
151. Z. Xu, C. Li, P. Yang, C. Zhang, S. Huang and J. Lin, *Cryst. Growth Des.*, 2009, **9**, 4752.
152. P. A. Tanner, L. Fu and B.-M. Cheng, *J. Phys. Chem. C*, 2009, **113**, 10773.
153. D. K. Williams, H. Yuan and f. B. M. f. B. M. Tissue, *J. Lumin.*, 1999, **83-84**, 297.
154. N. Dhananjaya, H. Nagabhushana, B. M. Nagabhushana, B. Rudraswamy, C. Shivakumara, K. Narahari and R. P. Chakradhar, *Spectrochim. Acta, Part A*, 2012, **86**, 8.
155. R. Bazzi, M. A. Flores, C. Louis, K. Lebbou, W. Zhang, C. Dujardin, S. Roux, B. Mercier, G. Ledoux, E. Bernstein, P. Perriat and O. Tillement, *J. Colloid Interface Sci.*, 2004, **273**, 191.
156. S. Ji, L. Yin, G. Liu, L. Zhang and C. Ye, *Chem. Commun.*, 2009, DOI: 10.1039/b902282a, 2344.
157. N. S. Singh, S. D. Singh and S. D. Meetei, *Chin. Phys. B*, 2014, **23**, 058104.
158. G. L. Kabongo, G. H. Mhlongo, T. Malwela, B. M. Mothudi, K. T. Hillie and M. S. Dhlamini, *J. Alloys Compd.*, 2014, **591**, 156.
159. E. Pereyra-Perea, M. R. Estrada-Yañez and M. García, *J. Phys. D: Appl. Phys.*, 1998, **31**, L7.
160. H. Choi, J. H. Kim, S.-s. Yi, B. K. Moon and J. H. Jeong, *J. Alloys Compd.*, 2006, **408-412**, 816.
161. L. Yu, H. Song, Z. Liu, L. Yang, S. Lu and Z. Zheng, *Solid State Commun.*, 2005, **134**, 753.
162. V. Pankratov, A. I. Popov, S. A. Chernov, A. Zharkouskaya and C. Feldmann, *Phys. Status Solidi B*, 2010, **247**, 2252.
163. Q. Li and V. W.-W. Yam, *Angew. Chem.*, 2007, **119**, 3556.
164. G. Wang, Q. Peng and Y. Li, *Acc. Chem. Res.*, 2011, **44**, 322.
165. L. Song and L. Xue, *Appl. Surf. Sci.*, 2012, **258**, 3497.
166. T. Grzyb, M. Runowski, A. Szczeszak and S. Lis, *J. Phys. Chem. C*, 2012, **116**, 17188.
167. B. Ritter, T. Krahl, K. Rurack and E. Kemnitz, *J. Mater. Chem. C*, 2014, **2**, 8607.
168. G. A. Sotiriou, M. Schneider and S. E. Pratsinis, *J. Phys. Chem. C*, 2012, **116**, 4493.
169. Q. Meng, B. Chen, W. Xu, Y. Yang, X. Zhao, W. Di, S. Lu, X. Wang, J. Sun, L. Cheng, T. Yu and Y. Peng, *J. Appl. Phys.*, 2007, **102**, 093505.
170. S. Ray, A. Patra and P. Pramanik, *Opt. Mater.*, 2007, **30**, 608.
171. F. Goubard, F. Vidal, R. Bazzi, O. Tillement, C. Chevrot and D. Teyssié, *J. Lumin.*, 2007, **126**, 289.
172. A. S. Pereira, M. Peres, M. J. Soares, E. Alves, A. Neves, T. Monteiro and T. Trindade, *Nanotechnology*, 2006, **17**, 834.
173. A. Urbietta, R. del Campo, R. Pérez, P. Fernández and J. Piqueras, *J. Alloys Compd.*, 2014, **610**, 416.
174. V. Kumar, S. Som, V. Kumar, V. Kumar, O. M. Ntwaeaborwa, E. Coetsee and H. C. Swart, *Chem. Eng. J.*, 2014, **255**, 541.
175. G. K. Das and T. T. Y. Tan, *J. Phys. Chem. C*, 2008, **112**, 11211.
176. J. A. Lichter, K. J. Van Vliet and M. F. Rubner, *Macromolecules*, 2009, **42**, 8573.
177. X. Zhang, L. Wang and E. Levänen, *RSC Adv.*, 2013, **3**, 12003.

178. A. Panacek, L. Kvitek, R. Prucek, M. Kolar, R. Vecerova, N. Pizurova, V. K. Sharma, T. Nevecna and R. Zboril, *J. Phys. Chem. B*, 2006, **110**, 16248.
179. N. M. Zain, A. G. Stapley and G. Shama, *Carbohydr. Polym.*, 2014, **112**, 195.
180. K. Vasilev, V. R. Sah, R. V. Goreham, C. Ndi, R. D. Short and H. J. Griesser, *Nanotechnology*, 2010, **21**, 215102.
181. S. Pal, Y. K. Tak and J. M. Song, *Appl. Environ. Microbiol.*, 2007, **73**, 1712.
182. S. Meghana, P. Kabra, S. Chakraborty and N. Padmavathy, *RSC Adv.*, 2015, **5**, 12293.
183. A. E. Nel, L. Madler, D. Velegol, T. Xia, E. M. Hoek, P. Somasundaran, F. Klaessig, V. Castranova and M. Thompson, *Nat. Mater.*, 2009, **8**, 543.
184. J. Diaz-Visurraga, A. Garcia and G. Cardenas, *Journal of applied microbiology*, 2010, **108**, 633.
185. P. Nalawade, P. Mukherjee and S. Kapoor, *Journal of Nanostructure in Chemistry*, 2014, **4**.
186. H. B. Li, P. Liu, Y. Liang, J. Xiao and G. W. Yang, *Nanoscale*, 2012, **4**, 5082.
187. S. Shankar and J.-W. Rhim, *Mater. Lett.*, 2014, **132**, 307.
188. K. Liu, M. Cao, A. Fujishima and L. Jiang, *Chem Rev*, 2014, **114**, 10044.
189. Y. Kikuchi, K. Sunada, T. Iyoda, K. Hashimoto and A. Fujishima, *J. Photochem. Photobiol. A: Chem*, 1997, **106**, 51.
190. X. Qiu, M. Miyauchi, K. Sunada, M. Minoshima, M. Liu, Y. Lu, D. Li, Y. Shimodaira, Y. Hosogi, Y. Kuroda and K. Hashimoto, *ACS Nano*, 2012, **6**, 1609.
191. R. H. Muller and C. M. Keck, *J. Biotechnol.*, 2004, **113**, 151.
192. J. Chomoucka, J. Drbohlavova, D. Huska, V. Adam, R. Kizek and J. Hubalek, *Pharmacol. Res.*, 2010, **62**, 144.
193. X. Peng, H. Chen, J. Huang, H. Mao and D. M. Shin, *Biomedical Engineering – From Theory To Applications*, InTech, 2011.
194. S.-W. Cao, Y.-J. Zhu, M.-Y. Ma, L. Li and L. Zhang, *J. Phys. Chem. C*, **112**, 1851.
195. N. T. K. Thanh and L. A. W. Green, *Nano Today*, 2010, **5**, 213.
196. X. Yang, J. J. Grailer, I. J. Rowland, A. Javadi, S. A. Hurley, V. Z. Matson, D. A. Steeber and S. Gong, *ACS Nano*, 2010, **4**, 6805.
197. Y. C. Chen, L. C. Liao, P. L. Lu, C. L. Lo, H. C. Tsai, C. Y. Huang, K. C. Wei, T. C. Yen and G. H. Hsiue, *Biomaterials*, 2012, **33**, 4576.
198. P. Zou, Y. Yu, Y. A. Wang, Y. Zhong, A. Welton, C. Galban, S. Wang and D. Sun, *Mol. Pharm.*, 2010, **7**, 1974.
199. K. Kaaki, K. Herve-Aubert, M. Chiper, A. Shkilnyy, M. Souce, R. Benoit, A. Paillard, P. Dubois, M. L. Saboungi and I. Chourpa, *Langmuir*, 2012, **28**, 1496.
200. S. Sun, *Adv. Mater.*, 2006, **18**, 393.
201. J. Gao, G. Liang, B. Zhang, Y. Kuang, X. Zhang and B. Xu, *J. Am. Chem. Soc.*, 2007, **129**, 1428.
202. J. Gao, B. Zhang, Y. Gao, Y. Pan, X. Zhang and B. Xu, *J. Am. Chem. Soc.*, 2007, **129**, 11928.
203. Y. Liu, D. Tu, H. Zhu, E. Ma and X. Chen, *Nanoscale*, 2013, **5**, 1369.
204. E. Hemmer, F. Vetrone and K. Soga, *MRS Bulletin*, 2014, **39**, 960.
205. S. Setua, D. Menon, A. Asok, S. Nair and M. Koyakutty, *Biomaterials*, 2010, **31**, 714.
206. F. Zhang and S. S. Wong, *ACS Nano*, 2010, **4**, 99.
207. G. A. Sotiriou, D. Franco, D. Poulidakos and A. Ferrari, *ACS Nano*, 2012, **6**, 3888.
208. N. Li, P. Zhao and D. Astruc, *Angew. Chem. Int. Ed.*, 2014, **53**, 1756.
209. H. Guo, F. Ruan, L. Lu, J. Hu, J. Pan, Z. Yang and B. Ren, *J. Phys. Chem. C*, 2009, **113**, 10459.
210. L. Rodríguez-Lorenzo, R. n. A. Álvarez-Puebla, F. J. G. a. de Abajo and L. M. Liz-Marzán, *J. Phys. Chem. C*, 2010, **114**, 7336.

211. Z. Jiang, Q. Zhang, C. Zong, B.-J. Liu, B. Ren, Z. Xie and L. Zheng, *J. Mater. Chem.*, 2012, **22**, 18192.
212. C. Zhu, G. Yang, H. Li, D. Du and Y. Lin, *Anal. Chem.*, 2015, **87**, 230.
213. C. Chen, Q. Xie, D. Yang, H. Xiao, Y. Fu, Y. Tan and S. Yao, *RSC Adv.*, 2013, **3**, 4473.
214. X. Gao, L. Jin, Q. Wu, Z. Chen and X. Lin, *Electroanalysis*, 2012, **24**, 1771.
215. E. Koposova, X. Liu, A. Kisner, Y. Ermolenko, G. Shumilova, A. Offenhausser and Y. Mourzina, *Biosens. Bioelectron.*, 2014, **57**, 54.
216. B. J. Plowman, M. Mahajan, A. P. O'Mullane and S. K. Bhargava, *Electrochim. Acta*, 2010, **55**, 8953.
217. J. Xie, Y. Zheng and J. Y. Ying, *Chem. Commun.*, 2010, **46**, 961.
218. X. Xia, Y. Long and J. Wang, *Anal. Chim. Acta*, 2013, **772**, 81.
219. L. V. Nair, D. S. Philips, R. S. Jayasree and A. Ajayaghosh, *Small*, 2013, **9**, 2673.
220. E. Zobeiri, A. Bayandori Moghaddam, F. Gudarzy, H. Mohammadi, S. Mozaffari and Y. Ganjkhanelou, *Luminescence*, 2015, **30**, 290.
221. W. Di, J. Li, N. Shirahata and Y. Sakka, *Nanotechnology*, 2010, **21**, 455703.
222. G. Wang, X. He, L. Wang, A. Gu, Y. Huang, B. Fang, B. Geng and X. Zhang, *Microchim. Acta*, 2012, **180**, 161.
223. L. C. Clark Jr and C. Lyons, *Ann. N. Y. Acad. Sci.*, 1962, **102**, 29.
224. S. J. Updike and G. P. Hicks, *Nature*, 1967, **214**, 986.
225. A. E. G. Cass, G. Davis, G. D. Francis, H. A. O. Hill, W. J. Aston, I. J. Higgins, E. V. Plotkin, L. D. L. Scott and A. P. F. Turner, *Anal. Chem.*, 1984, **56**, 667.
226. P. D. Hale, T. Inagaki, H. I. Karan, Y. Okamoto and T. A. Skotheim, *J. Am. Chem. Soc.*, 1989, **111**, 3482.
227. B. J. Plowman, S. K. Bhargava and A. P. O'Mullane, *The Analyst*, 2011, **136**, 5107.
228. M. Govindhan, B.-R. Adhikari and A. Chen, *RSC Adv.*, 2014, **4**, 63741.
229. K. E. T. a. R. G. Compton, *Int. J. Electrochem. Sci.*, 2010, **5**, 56.
230. E. M. Skou, E. Larsen, R. Winsnes, P. Pajunen, J. Koskikallio and C.-G. Swahn, *Acta Chem. Scand.*, 1973, **27**, 2239.
231. S. Park, H. Boo and T. D. Chung, *Anal. Chim. Acta*, 2006, **556**, 46.
232. Y. Bai, W. Yang, Y. Sun and C. Sun, *Sens. Actuators B: Chem.*, 2008, **134**, 471.
233. S. Cherevko and C.-H. Chung, *Sens. Actuators B: Chem.*, 2009, **142**, 216.
234. Y.-G. Zhou, S. Yang, Q.-Y. Qian and X.-H. Xia, *Electrochem. Commun.*, 2009, **11**, 216.
235. D. Feng, F. Wang and Z. Chen, *Sens. Actuators B: Chem.*, 2009, **138**, 539.
236. I. G. Casella, M. Contursi and R. Toniolo, *Electroanalysis*, 2014, **26**, 988.
237. L. Meng, J. Jin, G. Yang, T. Lu, H. Zhang and C. Cai, *Anal. Chem.*, 2009, **81**, 7271.
238. X. M. Chen, Z. J. Lin, D. J. Chen, T. T. Jia, Z. M. Cai, X. R. Wang, X. Chen, G. N. Chen and M. Oyama, *Biosens. Bioelectron.*, 2010, **25**, 1803.
239. Q. Zeng, J. S. Cheng, X. F. Liu, H. T. Bai and J. H. Jiang, *Biosens. Bioelectron.*, 2011, **26**, 3456.
240. L. M. Lu, H. B. Li, F. Qu, X. B. Zhang, G. L. Shen and R. Q. Yu, *Biosens. Bioelectron.*, 2011, **26**, 3500.
241. Q. Wang, X. Cui, J. Chen, X. Zheng, C. Liu, T. Xue, H. Wang, Z. Jin, L. Qiao and W. Zheng, *RSC Adv.*, 2012, **2**, 6245.
242. J. H. Yuan, K. Wang and X. H. Xia, *Adv. Funct. Mater.*, 2005, **15**, 803.
243. Z. Cao, Y. Zou, C. Xiang, L. X. Sun and F. Xu, *Anal. Lett.*, 2007, **40**, 2116.
244. J.-F. Huang, *Electroanalysis*, 2008, **20**, 2229.
245. Q. Shen, L. Jiang, H. Zhang, Q. Min, W. Hou and J.-J. Zhu, *J. Phys. Chem. C*, 2008, **112**, 16385.
246. S. Badhulika, R. K. Paul, Rajesh, T. Terse and A. Mulchandani, *Electroanalysis*, 2014, **26**, 103.

247. B. Singh, F. Laffir, T. McCormac and E. Dempsey, *Sens. Actuators B: Chem.*, 2010, **150**, 80.
248. J. Ryu, K. Kim, H. S. Kim, H. T. Hahn and D. Lashmore, *Biosens. Bioelectron.*, 2010, **26**, 602.
249. Y.-J. Lee and J.-Y. Park, *Sens. Actuators B: Chem.*, 2011, **155**, 134.
250. K.-J. Chen, W.-N. Su, C.-J. Pan, S.-Y. Cheng, J. Rick, S.-H. Wang, C.-C. Liu, C.-C. Chang, Y.-W. Yang, C.-H. Wang and B.-J. Hwang, *J. Mater. Chem. B*, 2013, **1**, 5925.
251. Y. Zhang, L. Su, D. Manuzzi, H. V. de los Monteros, W. Jia, D. Huo, C. Hou and Y. Lei, *Biosens. Bioelectron.*, 2012, **31**, 426.
252. L. Wang, Q. Zhang, S. Chen, F. Xu, S. Chen, J. Jia, H. Tan, H. Hou and Y. Song, *Anal. Chem.*, 2014, **86**, 1414.
253. L. M. Lu, L. Zhang, F. L. Qu, H. X. Lu, X. B. Zhang, Z. S. Wu, S. Y. Huan, Q. A. Wang, G. L. Shen and R. Q. Yu, *Biosens. Bioelectron.*, 2009, **25**, 218.
254. Z. Liu, Y. Guo and C. Dong, *Talanta*, 2015, **137**, 87.
255. A. Salimi and M. Roushani, *Electrochem. Commun.*, 2005, **7**, 879.
256. Q. Yi, W. Huang, W. Yu, L. Li and X. Liu, *Electroanalysis*, 2008, **20**, 2016.
257. A. Sun, J. Zheng and Q. Sheng, *Electrochim. Acta*, 2012, **65**, 64.
258. J. Zhao, F. Wang, J. Yu and S. Hu, *Talanta*, 2006, **70**, 449.
259. T.-K. Huang, K.-W. Lin, S.-P. Tung, T.-M. Cheng, I. C. Chang, Y.-Z. Hsieh, C.-Y. Lee and H.-T. Chiu, *J. Electroanal. Chem.*, 2009, **636**, 123.
260. J. Yang, W. D. Zhang and S. Gunasekaran, *Biosens. Bioelectron.*, 2010, **26**, 279.
261. L. Xu, J. Xia, H. Li, H. Li, K. Wang and S. Yin, *Eur. J. Inorg. Chem.*, 2011, **2011**, 1361.
262. K.-C. Lin, Y.-C. Lin and S.-M. Chen, *Electrochim. Acta*, 2013, **96**, 164.
263. X. Li, J. Yao, F. Liu, H. He, M. Zhou, N. Mao, P. Xiao and Y. Zhang, *Sens. Actuators B: Chem.*, 2013, **181**, 501.
264. T. Sreethawong, K. W. Shah, S.-Y. Zhang, E. Ye, S. H. Lim, U. Maheswaran, W. Y. Mao and M.-Y. Han, *J. Mater. Chem. A*, 2014, **2**, 3417.
265. J. Luo, S. Jiang, H. Zhang, J. Jiang and X. Liu, *Anal. Chim. Acta*, 2012, **709**, 47.
266. M. Tominaga, Y. Taema and I. Taniguchi, *J. Electroanal. Chem.*, 2008, **624**, 1.
267. D. Liu, Q. Luo and F. Zhou, *Synth. Met.*, 2010, **160**, 1745.
268. X. C. Dong, H. Xu, X. W. Wang, Y. X. Huang, M. B. Chan-Park, H. Zhang, L. H. Wang, W. Huang and P. Chen, *ACS Nano*, 2012, **6**, 3206.
269. G. Wang, X. Lu, T. Zhai, Y. Ling, H. Wang, Y. Tong and Y. Li, *Nanoscale*, 2012, **4**, 3123.
270. S. K. Meher and G. R. Rao, *Nanoscale*, 2013, **5**, 2089.
271. Z. Li, J. Zeng and Y. Li, *Small*, 2007, **3**, 438.
272. L. Zhang, L. Fu, X. Yang, Z. Fu, X. Qi and Z. Wu, *J. Mater. Chem. C*, 2014, **2**, 9149.
273. W. Di, X. Wang, B. Chen, S. Lu and X. Zhao, *J. Phys. Chem. B*, 2005, **109**, 13154.
274. K. M. Hayden, M. C. Norton, D. Darcey, T. Ostbye, P. P. Zandi, J. C. Breitner, K. A. Welsh-Bohmer and I. Cache County Study, *Neurology*, 2010, **74**, 1524.
275. M. F. Bouchard, D. C. Bellinger, R. O. Wright and M. G. Weisskopf, *Pediatrics*, 2010, **125**, e1270.
276. G. Velmurugan, D. D. Venkatesh Babu and S. Ramasamy, *Toxicology*, 2013, **307**, 103.
277. Y. A. Cho, Y. J. Kim, B. D. Hammock, Y. T. Lee and H. S. Lee, *J. Agric. Food Chem.*, 2003, **51**, 7854.
278. A. Garrido Frenich, J. L. Fernandez Moreno, J. L. Martinez Vidal and F. J. Arrebola Liebanas, *J. Agric. Food Chem.*, 2007, **55**, 8346.
279. H. Karasali, K. M. Kasiotis, K. Machera and A. Ambrus, *J. Agric. Food Chem.*, 2014, **62**, 11347.
280. Y. Fintschenko, A. J. Krynetsky and J. W. Wong, *J. Agric. Food Chem.*, 2010, **58**, 5859.
281. I. Ferrer, E. M. Thurman and A. R. Fernandez-Alba, *Anal. Chem.*, 2005, **77**, 2818.
282. D. Sharma, A. Nagpal, Y. B. Pakade and J. K. Katnoria, *Talanta*, 2010, **82**, 1077.

283. J. N. Seiber and L. A. Kleinschmidt, *J. Agric. Food Chem.*, 2011, **59**, 7536.
284. L. Chen, Y. Jiang, Y. Yang, J. Huang, J. Shi and S. Chen, *J. Phys. D: Appl. Phys.*, 2009, **42**, 215104.
285. W. Zheng, D. Tu, P. Huang, S. Zhou, Z. Chen and X. Chen, *Chem. Commun.*, 2015, **51**, 4129.
286. X. Liu, C. Li, Z. Quan and J. Lin, *J. Phys. Chem. C*, 2007, **111**, 16601.
287. C.-H. Hsu and C.-H. Lu, *J. Mater. Chem.*, 2011, **21**, 2932.

List of Abbreviations

Bcc	Body-centered cubic
CFU	Colony forming unit
CTAB	Cetyltrimethylammonium bromide
CV	Cyclic voltammetry
E. coli	Escherichia coli
Fcc	Face-centered cubic
FESEM	Field-emission scanning electron microscope
FRET	Fluorescence resonance energy transfer
FTO	Fluorine doped tin oxide
GO _x	Glucose oxidase
HRTEM	High-resolution transmission electron microscopy
LOD	Limit of detection
LUMO	Lowest unoccupied molecular orbital
LB	Lysogeny broth
PVP	Poly(N-vinylpyrrolidone)
FRET	Fluorescence resonance energy transfer
SHE	Standard hydrogen electrode
SPR	Surface plasmon resonance
PBS	Phosphate-buffered saline
PL	Photoluminescence

RE	Rare earth
SAED	Selected area (electron) diffraction
S. aureus	Staphylococcus aurea
SERS	Surface enhanced Raman Scattering
UV-vis	Ultraviolet-visible
TEM	Transmission electron microscopy
TOPO	Trioctylphosphine oxide
TOP	Trioctylphosphine
EDX	Energy dispersive X-ray analysis
XRD	X-ray diffraction
XPS	X-ray photoelectron spectroscopy